Gas phase bimetallic nanoclusters-modified TiO₂ supports as efficient photo(electro)catalysts for self-cleaning surfaces and water splitting

Vana Chinnappa Chinnabathini

Supervisors:
Prof. Dr. Ewald Janssens
Prof. Dr. Sammy W. Verbruggen (University of Antwerp)
Co-supervisor:
Dr. Didier Grandjean

Members of the Examination Committee:
Prof. Dr. Enrico Carlon (Chair)
Prof. Dr. Peter Lievens
Prof. Dr. Joris van de Vondel
Prof. Dr. Francesca Baletto (University of Milan)
Dr. Fons Dingenen (University of Antwerp)

Acknowledgment

"Commit your work to the Lord, and your plans will succeed" -- Proverbs 16:3. This biblical wisdom guided me during my PhD studies. And, indeed, all my endeavors have flourished.

PhD studies constitute a journey into the unknown and I did not travel alone on this journey. Many good and generous souls accompanied me all through and the outcome is this PhD thesis. To begin with, I am very grateful to **God in Jesus** for His powerful, unassuming and ever-assuring presence all through my PhD journey. My love and gratitude to **Mother Mary** for her powerful intercession at every stage of my PhD.

My profound gratitude goes to my promoters, Prof. Ewald Janssens, Prof. Sammy Verbruggen (University of Antwerp), and co-supervisor Dr. Didier Grandjean for their valuable guidance and support. The opportunities and skills they provided, were instrumental in conducting my PhD research smoothly and efficiently at both QSP, KU Leuven, and DuEL, University of Antwerp. Thank you very much for providing me with this excellent opportunity to work with you to build up scientific knowledge, experience and networking. My special thanks go to Prof. Ewald Janssens and Dr. Didier Grandjean for understanding my background and teaching me patiently the intricacies of research all through. I truly appreciate your patience, guidance and above all your good heart. Special thanks to Prof. Ewald Janssens for giving me scholarship during the last phase of PhD journey. I am profoundly inspired by your hard work, discipline, patience, and dedication to your profession, as well as your methodical approach to tasks. I consider myself extremely fortunate to have such an excellent mentor. I want to express very specially my heartfelt gratitude for all the support you have provided me throughout my PhD journey. There have been instances where I

Abstract

In the context of global challenges such as climate change and environmental pollution, photocatalysis evolved as one of the promising strategies for sustainable energy conversion and pollutant degradation. In this thesis, photocatalysis using gas phase deposited bimetallic nanoclusters (BNCs) on TiO_2 supports is studied in the context of self-cleaning surfaces and photoelectrochemical (PEC) water splitting applications. Thanks to their plasmonic properties, BNCs made of coinage metals can serve as efficient cocatalysts for the degradation of organic pollutants and surface contaminants under light irradiation. They also hold great promise for PEC water splitting, a promising pathway for renewable hydrogen production, which can be used in hydrogen fuel cells or for the environmentally friendly production of fuels in, for example, CO_2 hydrogenation processes.

The small size and high surface-to-volume ratio of plasmonic BNCs play pivotal roles in influencing the efficiency and selectivity of photocatalytic processes. BNCs have unique optical, physical, chemical, and structural properties distinctly different from their bulk and monometallic counterparts. These properties can be fine-tuned at the single particle level by their size, composition, and atomic arrangement, but also by interaction with other particles through the coverage and through interaction with the support. To design better photocatalysts it is crucial to carefully understand the BNCs' characteristic properties, especially at the atomic level where synergies between different elements are sought. To achieve this objective, BNCs with well-defined sizes and compositions are deposited on TiO_2 supports and we studied their structural properties and their influence on the photocatalytic activity.

The general procedure followed in this thesis is the production and deposition of BNCs on TiO_2 by the cluster beam deposition (CBD) technique, followed by structural and optical characterization to understand their tailored properties, and photocatalytic testing either for photodecomposition of organic molecules or PEC water splitting.

In a first study, Au_xAg_{1-x} (x = 1, 0.9, 0.7, 0.5, 0.3, and 0) alloy BNCs with different compositions are synthesized in the gas phase and deposited from a molecular beam on TiO_2 P25 supports. The photocatalytic self-cleaning activity of as-prepared samples is tested under UV and visible light towards stearic acid

(SA) degradation. SA is a widely accepted model contaminant, which represents the group of organic fouling compounds that typically contaminates glass surfaces. A composition-dependent activity is observed with the $Au_{0.3}Ag_{0.7}$ nanocluster modified TiO_2 exhibiting the highest photoactivity. Scanning transmission electron microscopy (STEM) measurements reveal that, for a mass loading corresponding to an equivalent of 4 atomic monolayers (MLs), the BNCs are uniformly distributed over the surface. The clusters have an average size of 3.5 ± 0.5 nm and are crystalline in nature. The atomic structure is characterized by X-ray absorption fine structure (XAFS) spectroscopy and their electronic structure by X-ray photoelectron spectroscopy (XPS). These measurements demonstrate a charge redistribution between the Ag and Au atoms when alloyed at the nanoscale. The effect of this charge redistribution is likely the stabilization of Ag against oxidation and directly affects the catalytic properties of the clusters. It is suggested that the highest photoactivity of 4 ML loaded $Au_{0.3}Ag_{0.7}$ under solar light results from a combination of four main possible contributing factors: (i) injection in TiO_2 of excited carriers that are generated by the localized surface plasmon resonance (LSPR) effect of the BNCs in the visible light wavelength range which overlaps with the sun's irradiance spectrum. (ii) a strong near-field enhancement that increases the photoabsorption by the TiO_2 for photons that have enough energy to overcome the high bandgap, (iii) the optimized total metal loading of 4 ML leaves enough of the TiO_2 surface accessible for light absorption, and finally (iv) an effective charge distribution between Au and Ag. This study demonstrates that CBD is an efficient approach for fabricating well-defined, tunable AuAg plasmon-based photocatalysts for self-cleaning applications, outperforming their monometallic counterparts as well as bimetallic alternatives obtained through colloidal methods.

In a second study, titania nanotubes (TNTs) are modified with a series of Au_xCu_{1-x} (x = 1, 0.75, 0.5, 0.25, and 0) BNCs using the CBD technique. Based on the results of the first study, we opted again for a loading of 4 ML. TNTs are known for their high surface area, fast charge transfer, and corrosion resistance, while keeping the inherent strengths of traditional TiO_2 materials. They prove to be promising photoanodes, enhancing photocurrent in PEC applications for water oxidation. In this work the TNTs are grown via anodic oxidation of a titanium metal foil. The crystalline anatase phase of the grown TNTs is confirmed by the X-ray diffraction technique (XRD), while transmission electron microscopy (TEM) provides information about the size and composition of the deposited BNCs. XAFS provides further structural information, while XPS measurements

reveal charge redistribution between Au and Cu, which can aid in the enhancement of the PEC activity. Oxidation of as-prepared electrodes over the time results in structural changes with Cu_xO at the outer shell functioning as a protective layer, while the majority of the core is an alloy. The optical properties, studied through UV-Vis spectroscopy confirm the extended absorption range of the cluster-modified TNTs towards the visible region. The charge carrier recombination rate is derived from photoluminescence (PL) measurements. The as-prepared electrodes are tested photoelectrochemically for the generation of an anodic photocurrent using simulated sunlight. It is found that the Au_xCu_{1-x} (x = 1, 0.75, 0.5, 0.25 and 0) BNC modified TNTs show a remarkable enhancement in the anodic photocurrent relative to pristine TNTs, with $Au_{0.25}Cu_{0.75}$ exhibiting the highest photocurrent. This is due to the combination of many possible factors. Firstly, the charge redistribution between Au and Cu and increase stability of the $Au_{0.25}Cu_{0.75}$ electrode as observed in XAFS, indicates that the electronic effect in the cluster is also one of the governing factors for PEC activity. Secondly, formation of a surface CuO_x layer, protects against further corrosion of the metallic AuCu BNCs cores. Third, reduced recombination of charge carriers is indicated by lower photoluminescent (PL) intensity compared to pristine TNTs and all other electrodes except pure gold, as observed in PL spectra. This implies that the generated charge carriers are efficiently separated by $Au_{0.25}Cu_{0.75}$ NCs acting as electron sinks and easily available for redox reactions. Fourth, the highest interfacial charge transfer efficiency is evidenced by the electrochemical impedance spectroscopy (EIS), leading to more efficacious charge migration and separation, facilitating the water oxidation surface reaction. A final beneficial factor is the uniform deposition of well-defined, size- and composition-controlled, ligand-free BNCs. Such BNCs provide more effective surface sites to the reaction medium, in contrast to electrodes synthesized by e.g. sol-gel methods, where (in)organic residues on metal surfaces may decrease the efficiency.

The structure of thesis is as follows: Chapter 1 introduces the research work and places it in a wider context, stressing the need to go beyond the state of the art. Chapter 2 gives an overview of the experimental techniques used in the thesis work, with examples from own experimental work. The main findings of the research are presented in chapters 3 and 4 where chapter 3 contains the results of SA degradation by Au_xAg_{1-x} BNCs on P25 TiO_2 nanoparticles, chapter 4 deals with PEC water splitting using Au_xCu_{1-x} BNCs on titania nanotubes. Finally, chapter 5 provides a comprehensive summary of thesis and proposes novel

experiments based on the insights gained throughout this study and their potential implications.

Samenvatting

In de context van wereldwijde uitdagingen zoals klimaatverandering en milieuvervuiling, heeft fotokatalyse zich ontwikkeld tot één van de meest veelbelovende strategieën voor duurzame energieomzetting en de afbraak van vervuilende stoffen. In dit proefschrift werd fotokatalyse bestudeerd met bimetallische nanoclusters (BNC's), in gasfase afgezet op TiO_2-dragers, met name in toepassingen van zelfreinigende oppervlakken en foto-elektrochemische (PEC) watersplitsing. Dankzij hun plasmonische eigenschappen kunnen BNC's gemaakt van edelmetalen dienen als efficiënte co-katalysatoren voor de afbraak van oppervlakteverontreinigingen onder belichting. Ze zijn ook veelbelovend voor de PEC-watersplitsing, een cruciaal proces voor de productie van hernieuwbare waterstof die kan gebruikt worden in waterstofbrandstofcellen of voor de milieuvriendelijk productie van brandstoffen via bijvoorbeeld CO_2 hydrogenatiereacties.

De kleine afmetingen en hoge oppervlakte-volumeverhouding van plasmonische BNC's spelen een centrale rol voor de efficiëntie en selectiviteit van fotokatalytische processen. BNC's hebben unieke optische, fysische, chemische en structurele eigenschappen die duidelijk verschillen van hun bulk- en monometallische tegenhangers. Deze eigenschappen kunnen worden verfijnd op het niveau van de afzonderlijke deeltjes door hun grootte, samenstelling, en atomaire rangschikking, alsook door de interactie met andere deeltjes door de bedekkingsgraad te variëren of door de interactie met de drager. Om betere fotokatalysatoren te ontwerpen is het cruciaal om de karakteristieke eigenschappen van de BNC's goed te begrijpen, vooral op atomair niveau waar synergieën tussen verschillende elementen worden gezocht. Om dit doel te bereiken zijn BNC's met goed gedefinieerde afmetingen en samenstellingen afgezet op TiO_2-dragers en hebben we hun structurele eigenschappen en hun invloed op de fotokatalytische activiteit bestudeerd.

De algemeen procedure die gevolgd werd in dit proefschrift is de productie en afzetting van BNC's op TiO_2 door de clusterbundeldepositietechniek (CBD), structurele en optische karakterisering om hun specifieke eigenschappen te begrijpen, gevolg door fotokatalytische

testen voor ofwel fotodecompositie van organische molecules of PEC-watersplitsing.

In de eerste studie worden Au_xAg_{1-x} (x = 1, 0,9, 0,7, 0,5, 0,3 en 0) BNC's met verschillende samenstellingen gesynthetiseerd in de gasfase en afgezet op TiO_2 P25-substraten. De fotokatalytische zelfreinigende activiteit van de bereide stalen wordt getest onder ultraviolet (UV) en zichtbaar (Vis) licht voor de afbraak van stearinezuur (SA). SA is algemeen aanvaard als modelmolecule voor organische vervuiling op oppervlakken. Er werd een samenstellingsafhankelijke activiteit waargenomen waarbij TiO_2 gemodificeerd met $Au_{0.3}Ag_{0.7}$-nanoclusters de hoogste fotoactiviteit vertoont. Metingen met behulp van scanning-transmissie-elektronenmicroscopie (STEM) tonen aan dat de BNC's, bij een maslading die overeenkomt met een equivalent van 4 atomaire monolagen (MLs) uniform over het oppervlak verdeeld zijn. De clusters hebben en gemiddelde grootte van 3,5 ± 0,5 nm en zijn kristallijn van aard. De atomaire structuur is gekarakteriseerd door *X-ray absorption fine structure* (XAFS) spectroscopie en de elektronische structuur door en *X-ray photoelectron spectroscopy* (XPS). Deze metingen tonen een herverdeling van de lading aan tussen de Ag- en Au-atomen in deze nanolegeringen. Het effect van deze ladingsherverdeling is waarschijnlijk de stabilisatie van Ag tegen oxidatie en beïnvloedt directe de katalytische eigenschappen van de clusters. Er wordt gesuggereerd dat de hoogste fotoactiviteit van 4 ML geladen $Au_{0,3}Ag_{0,7}$ onder zonlicht het resultaat is van een combinatie van vier mogelijke factoren: (i) de injectie in TiO_2 van geëxciteerde ladingsdragers die resulteren van de gelokaliseerde oppervlakteplasmonresonantie (LSPR) van de BNC's in het golflengtegebied dat samenvalt met het zonnespectrum, (ii) een felle versterking van het nabije elektrische veld die de foto-absorptie door TiO_2 verhoogt voor fotonen die voldoende energie hebben om de bandkloof te overwinnen, (iii) de geoptimaliseerde metaalhoeveelheid van 4 ML die voldoende van het TiO_2 rechtstreeks toegankelijk laat voor lichtabsorptie, en tenslotte (iv) een effectieve ladingsverdeling tussen Au en Ag. Deze studie demonstreerde dat CBD een efficiënte methode is voor het vervaardigen van goed gedefinieerde, afstembare AuAg plasmon-gebaseerde fotokatalysatoren voor zelfreinigende oppervlakken, die beter presteren dan hun monometallische tegenhangers en als bimetallische alternatieven verkregen via colloïdale methoden.

In een tweede studie worden titaniananotubes (TNT's) gemodificeerd met een reeks van Au_xCu_{1-x} (x = 1, 0,75, 0,5, 0,25 en 0) BNC's met behulp van de CBD-techniek. Op basis van de resultaten van de eerste studie wordt opnieuw gekozen voor een belasting van 4 ML. TNT's staan bekend om hun grote oppervlakte, en hoge corrosiebestendigheid, terwijl ze de inherente voordelen van traditionele TiO_2-materialen behouden. Ze blijken veelbelovende fotoanodes te zijn die de fotostroom in PEC-toepassingen voor wateroxidatie verbeteren. De kristallijne anataasfase van de gegroeide TNT's werd bevestigd door de röntgendiffractietechniek (XRD), terwijl transmissie-elektronenmicroscopie (TEM) informatie geeft over de grootte en samenstelling van de neergezette BNC's. XAFS geeft verdere structurele informatie, terwijl XPS-metingen de ladingsherverdeling tussen Au en Cu laat zien, welke kan helpen bij de verbetering van de PEC-activiteit. Oxidatie van de geprepareerde elektroden in de loop van de tijd resulteert in structurele veranderingen waarbij Cu_xO in de buitenste schil functioneert als een beschermende laag, terwijl het grootste deel van de kern een legering is. De optische eigenschappen, bestudeerd met UV-Vis-spectroscopie, bevestigen het uitgebreide absorptiebereik van TNT's in het zichtbare gebied. De recombinatiesnelheid van de ladingsdragers is afgeleid uit fotoluminescentie (PL)-metingen. De geprepareerde elektroden zijn foto-elektrochemisch getest op het genereren van een anodische fotostroom met behulp van gesimuleerd zonlicht. Het blijkt dat de Au_xCu_{1-x} (x= 1, 0,75, 0,5, 0,25 en 0) BNC-gemodificeerde TNT's een opmerkelijke verbetering vertonen in de anodische fotostroom ten opzichte van TNT's zonder clusters, waarbij $Au_{0,25}Cu_{0,75}$ de hoogste fotostroom laat zien. Dit is het gevolg van een combinatie van factoren. Ten eerste geeft de ladingherverdeling tussen Au en Cu en de toename van de stabiliteit van de $Au_{0,25}Cu_{0,75}$-elektrode, zoals waargenomen in XAFS, een indicatie voor het belang van het elektronische effect in de cluster voor PEC-activiteit. Ten tweede beschermt de vorming van een CuO_x laag aan het oppervlak tegen verdere corrosie van de metallische AuCu BNC-kernen. Ten derde is er een verminderde recombinatie van ladingsdragers, aangegeven door de lage fotoluminescerende (PL) intensiteit. Dit impliceert dat de gegenereerde ladingsdragers efficiënt werden gescheiden door $Au_{0,25}Cu_{0,75}$ NC's die fungeren als elektronenputten en gemakkelijk beschikbaar zijn voor redoxreacties. Ten vierde is er een hoge efficiëntie van ladingsoverdracht aan het grensvlak, bewezen door de elektrochemische impedantiespectroscopie (EIS), wat leidt tot effectieve ladingsmigratie en -scheiding, waardoor de wateroxidatie oppervlaktereactie

wordt bevorderd. Een laatste gunstige factor is de uniforme neerzetting van goed gedefinieerde, grootte- en samenstellingsgecontroleerde, ligandvrije BNC's. Dergelijke BNC's verschaffen een effectieve centra voor oppervlaktereacties, in tegenstelling tot elektroden die zijn gesynthetiseerd met bv. sol-gel-methoden, waarbij (an)organische residuen op het oppervlak achterblijven.

De structuur van het proefschrift is als volgt: Hoofdstuk 1 introduceert het onderzoekswerk en plaatst het in de bredere context, waarbij de noodzaak wordt benadrukt om verder te gaan dan de huidige *state of the art*. Hoofdstuk 2 geeft een overzicht van de experimentele technieken die in dit proefschrift zijn gebruikt, met voorbeelden uit eigen experimenteel werk. De belangrijkste bevindingen van het onderzoek worden gepresenteerd in de hoofdstukken 3 en 4. Waar hoofdstuk 3 de resultaten van SA-afbraak door Au_xAg_{1-x} BNC's op P25 TiO_2 nanodeeltjes bevat, behandelt hoofdstuk 4 de PEC-watersplitsing met Au_xAu_{1-x} BNC's op titaniananotubes. Tenslotte geeft hoofdstuk 5 een samenvatting van het proefschrift en worden nieuwe experimenten voorgesteld, gebaseerd op de inzichten die tijdens dit onderzoek zijn opgedaan, en hun potentiële implicaties.

Table of Contents

List of Abbreviations

Acronym	Long name
ABPE	Applied bias to photon conversion efficiency
AM	Air mass - The path length that sunlight travels through the Earth's atmosphere
BE	Binding energy
BNCs	Bimetallic nanoclusters
BNPs	Bimetallic nanoparticles
CA	Chronoamperometry
CBD	Cluster beam deposition
CB	Conduction band
CDA	Cluster deposition apparatus
CN	Coordination number
DC	Direct current
DFT	Density functional theory
DRS	Diffuse Reflectance Spectroscopy
EIS	Electrochemical impedance spectroscopy
EDX	Energy-dispersive X-ray spectroscopy
EPR	Electron paramagnetic resonance
ESRF	European synchrotron radiation facility
EXAFS	Extended X-ray absorption fine structure
FQE	Formal quantum efficiency
FEG	Field emission gun
FTIR	Fourier transform infrared
GeV	Giga electron volts
HAADF-STEM	High-angle annular dark-field scanning transmission electron microscopy
HAS	Hemispherical analyzer
IPCE	Incident photon-to-electron conversion efficiency
IR	Infrared
JSC	Short-circuit photocurrent density
ML	Atomic monolayer
NCs	Nanoclusters
NG	Noble gas
NPs	Nanoparticles
(L)SPR	(Localized) surface plasmon resonance
LUMO	Lowest unoccupied molecular orbital

MCP	Microchannel plate detector
ML	Monolayer
OCV	Open circuit potentials
OD	Optical density
PEC	Photoelectrochemical
PSV	Pulsed supersonic valve
QCM	Quartz crystal microbalance
RHE	Real hydrogen electrode
RToF-MS	Reflectron time of flight mass spectrometer
Refl- XAFS	Fluorescent reflection mode X-ray absorption fine structure
SA	Stearic acid
SCE	Saturated calomel electrode
SDG	Sustainable development goals
SEM	Scanning electron microscopy
SHE	Standard hydrogen electrode
STEM	Scanning transmission electron microscopy
TEY	Total electron yield
TNTs	Titania nanotubes
UHV	Ultra-high vacuum
UV- Vis	Ultraviolet- Visible
VB	Valence band
Wt%	Weight percentage
XAS	X-ray absorption spectroscopy
XANES	X-ray absorption near edge spectroscopy
XPS	X-ray photoelectron spectroscopy
XRD	X-ray diffraction

List of Symbols and Units

A	Debye-Waller term for each shell = $2\,\sigma^2$
a	Lattice constant
c	Velocity of light
d	Cluster diameter
D_v and D_h	Deflection voltages (vertical and horizontal)
D	Diffusion coefficient
e^-	Electron
E	Photon energy
E_{KE}	Kinetic energy
E_{BE}	Binding energy
E_{CB}	Conduction band energy
E_{VB}	Valence band energy
$E°$	(Standard) Redox potential
E_g	Band gap energy
E_p	Electrostatic potential energy
$\vec{E}_{sc}$	Scattered electrical field intensity vector
$\vec{E}_{inc}$	Incident electrical field intensity vector
$\vec{E}_{tot}$	Total electrical field intensity vector
f	Relaxation frequency
h	Planck's constant
$\hbar$	reduced Planck's constant = $h/2\pi$
h^+	Hole
I	Intensity of light transmitted through sample
I_0	Incident light intensity
j	Current density
k	Wave vector
L	Angular momentum
L_d	Hole diffusion length
m	Mass
N	Number of atoms in each cell
p	Momentum
P	Power
q	Cluster charge
R	Atomic distance / Radius
$R(\%)$	Percentage fit- Agreement fraction
R_{ct}	Charge transfer resistance
T	Transmittance
t_F	free flight of path length

$t_{1/2}$	Half-life
ν	frequency of the light
V	Potential
x	Distance
Z	Atomic number
v	Cluster velocity
$\mu(E)$	Oscillating portion of the X-ray absorption coefficient
$\mu_0(E)$	Isolated-atom X-ray absorption
μ_{exp}	Measured X-ray absorption signal
ρ	Sample density
$\chi(E)$	Modulated X-ray absorption
ϕ	Work function of the energy analyzer
ε	Dielectric constant
ε_r	Relative permittivity
λ	Wavelength
σ^2	Debye- Waller factor
τ	Hole relaxation time/ electron lifetime

Units

Å	Ångström
a.u.	Arbitrary units
u	Atomic mass units
atm	Standard atmosphere
GeV	Giga electron volt
hPa	Hectopascal
kV	Kilo volts
mA/cm^2	Milli ampere per square centimeter
mW	Milliwatt
ppm	Parts per million
rpm	Rotation per minute
W	Watt

Chapter 1

Introduction

Today, 'sustainability' or 'sustainable development' stands as a global rallying cry. In 2015, all United Nations member states collectively came up with "The 2030 Agenda for Sustainable Development," presenting a shared roadmap for long term human life on the planet, both presently and in the future. Central to this agenda are the 17 Sustainable Development Goals (SDGs),[1] representing a pressing call to action for all nations, regardless of their development status, to collaborate in addressing global challenges.

My PhD thesis is related to three of these SDGs: ensuring healthy lives (SDG 3), promoting renewable and clean energy (SDG 7), and climate action to preserve the earth's resources (SDG 13). These goals emphasize some of the contemporary challenges we face: the escalating threat of global warming, the depletion of fossil fuel resources, and the pervasive issue of urban pollution. Global and scientific communities are seeking solutions to address these pressing issues. Photocatalysis and photoelectrocatalysis can contribute to attainable and sustainable solutions for mitigating urban pollution and global warming, and can provide renewable energy as alternative to fossil fuels.

The interest in photocatalysis began with the energy crisis of the 1970s when people worldwide realized that the supply of fossil fuels (coal, oil and natural gas) cannot last forever, and that humanity will face serious consequences if continuing to use earth's resources uncontrollably. Furthermore, the consumption of fossil fuels leads to an increase in the CO_2 content in the atmosphere. CO_2 is the main by-product in the usage of fossil fuels that contribute up to 75% of the estimated greenhouse gases according to United Nations.[2] Excess of CO_2 causes global warming and other undesirable climate changes. Therefore, we are confronted with urgent need to identify and use renewable energy resources. These are expected to have no destructive impact on the environment and will enable energy security. Currently renewable energy sources like hydropower (electrical energy generated via abundant water resources),[3] wind energy, geothermal energy (heat extracted from rocks beneath water beds or undergrounds)[4] and solar energy are being used, but geographical, technological, cost-effectiveness challenges remain. In an attempt to explore new ways or to modify existing ways to maximally exploit renewable energy resources, hydrogen has been looked upon as a good energy carrier.[5] There are different paths for hydrogen production, namely steam methane reforming, coal gasification, electrolysis, biomass gasification, thermochemical

water splitting, biohydrogen production, and photoelectrochemical (PEC) decomposition of water.[5] This last path has caught the attention of the world after the study in 1972 by Fujishima and Honda[6] using titanium dioxide (TiO_2) and later in 1991 by O'Regan and Grätzel.[7] The study of Fujishima and Honda demonstrated the possibility of generating hydrogen through photocatalysis from water using solar energy, offering a beacon of hope in addressing the global energy crisis. From then on, TiO_2 has been investigated extensively by the scientific community. **Figure 1.1** gives an overview of various applications of TiO_2 in industry, for a variety of reasons. In particular, it is an excellent photocatalyst for a number of reactions, including solar fuel production, oxidation or degradation of pollutants, anti-fogging or self-cleaning coatings for windows, and hydrogen production.[8]
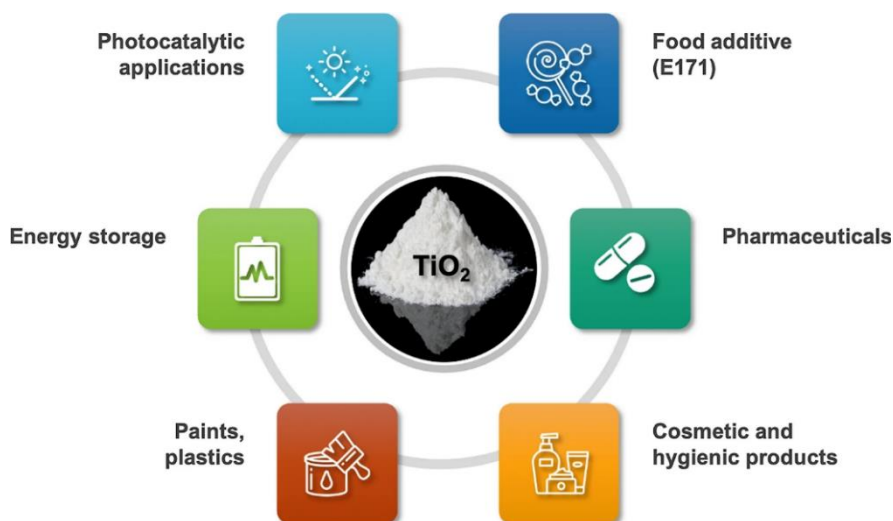
Figure 1.1. Various applications of titanium dioxide, adapted from ref. [9].

1.1. TiO_2 based photocatalysis

Despite the extensive research on various semiconductors over the years, TiO_2 continues to stand out as an unmatched n-type semiconductor, particularly in photocatalytic and PEC applications. This superiority is attributed to its exceptional photocatalytic activity, chemical and thermal stability, ability for large-scale production, cost-effectiveness, suitable positions of conduction band (CB) and valence band (VB) and low toxicity.[10,11,12,13,14] Before going into

the detailed characteristics of TiO_2, first a brief introduction to photocatalysis is given.

Photocatalysis is a technology in which a semiconductor is irradiated by (solar) light to drive a chemical reaction. When semiconductors, like TiO_2, absorb photons, electrons and holes are generated, which can then initiate the reduction and/or oxidation reactions.[10] To be more specific, when the semiconductor is exposed to photons with an energy equal to or larger than its bandgap, $hv \geq E_{CB} - E_{VB}$ with h the Planck's constant, v the frequency of light, and E_{CB} and E_{VB} the conduction and the valence-band energy, respectively, the photon energy can be transferred to an electron that is excited from the VB to the CB. This process leaves a hole in the VB and places an excited electron in the CB. The excited electrons and holes should be efficiently separated so that they can be utilized for different chemical reactions, as applied in photocatalytic wastewater treatment, air purification, water splitting, CO_2 reduction, disinfection, and self-cleaning surfaces.[15,16,17,18] Therefore efficient charge carrier separation and prevention of electron-hole recombination, which can occur on the surface of semiconductor, is important. A large charge carrier lifetime is essential for a good photocatalytic activity.

TiO_2 has dominated the field of photocatalysis in the last five decades, i.e. since Honda and Fujishima discovered the photoelectrocatalytic water splitting over TiO_2 electrodes under ultraviolet (UV) light illumination.[6] Titania naturally exhibits four different polymorphs, i.e., anatase, rutile, brookite and TiO_2(B) of which anatase is the most photoactive phase and rutile is thermodynamically the most stable one.[19] **Figure 1.2** shows the schematic crystal structure of the four common TiO_2 phases using Ti–O octahedrons as the fundamental building block. These four phases have different symmetry, and their corresponding nanostructures exhibit different growth behavior. Rutile TiO_2 has a tetragonal structure,[20] with {011} and {100} planes having the lowest surface energy. The equilibrium morphology of rutile nanoparticles is a trunked octahedron. The anatase phase also has a tetragonal structure and trunked octahedral morphologies in the corresponding.[20] Brookite is orthorhombic and has a large unit cell consisting of 8 TiO_2 units. TiO_2(B) also has a large unit cell with a more open crystal structure compared to other polymorphs.[21] Anatase TiO_2, being the most photoactive phase of TiO_2,[22,23] is the preferred polymorph in this research and can be obtained by annealing treatments at relatively mild temperatures and is very stable under irradiance conditions.
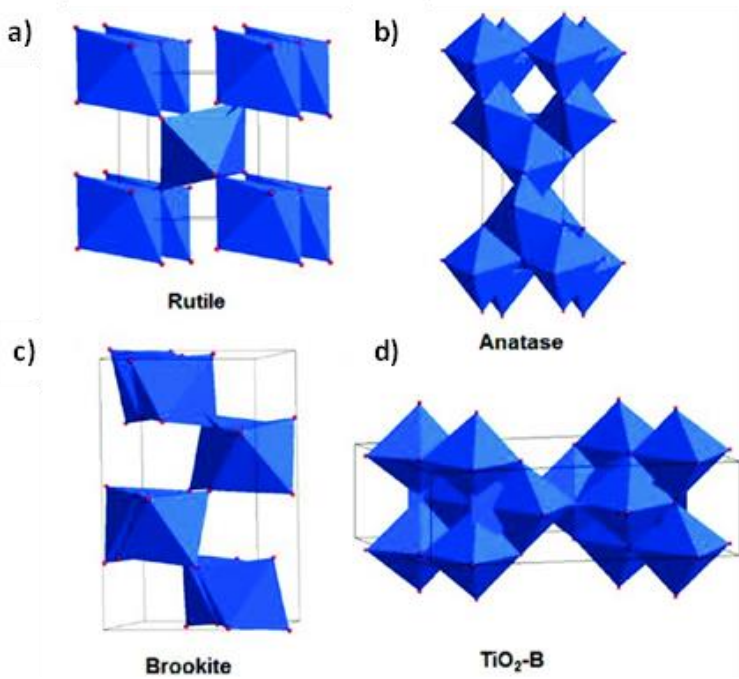
Figure 1.2. Schematic crystal structure of the four TiO_2 polymorphs (a) rutile, (b) anatase, (c) brookite, and (d) TiO_2(B), figure adapted from ref. [24].

$$TiO_2 + h\upsilon \rightarrow TiO_2 + e^-_{CB} + h^+_{VB} \quad (1.1)$$

$$H_2O + h^+_{VB} \rightarrow {}^\bullet OH + H^+ \quad (1.2)$$

$$O_2 + e^-_{CB} \rightarrow O_2^{-\bullet} \quad (1.3)$$

$$O_2^{-\bullet} + H^+ \rightarrow {}^\bullet OOH \quad (1.4)$$

$${}^\bullet OOH + {}^\bullet OOH \rightarrow H_2O_2 + O_2 \quad (1.5)$$

$$H_2O_2 + e^-_{CB} \rightarrow {}^\bullet OH + OH^-$$
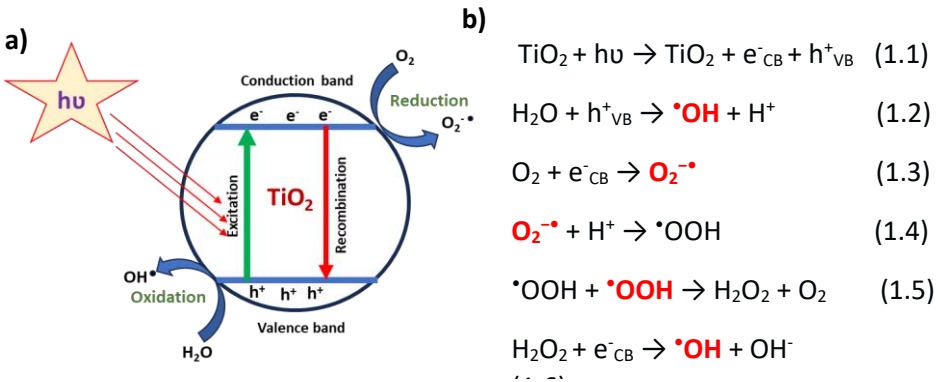
Figure 1.3. a) Schematic presentation of mechanism of TiO_2 based photocatalysis and b) a set of radical chain of reactions involved in this process (reactions 1.1 to 1.6).

When the photons are absorbed inside the semiconductor photocatalyst, the excited electrons and holes need to migrate to the surface before they can initiate redox reactions. In a homogeneous semiconductor, the migration is a random walk and thus the excited electrons and holes have plenty of chance to recombine due to lattice defects, crystal imperfections, and impurities,[25] causing low photocatalytic efficiency. Furthermore, for large-bandgap materials, such as TiO_2, the use of UV light requires artificial light sources and consumes more electricity, making it less attractive when energy supply and cost are concerns. The need to use sunlight more efficiently has sparked increasing research interest in photocatalysis.

Figure 1.3 gives the mechanism involved in photocatalysis as a set of radical chain reactions with a series of reactive species. The large band gap of anatase TiO_2 (3.2 eV) necessitates the use of UV light for electron-hole pair formation (equation 1.1). This band gap ensures sufficient longevity for the photogenerated electron pair to migrate to the photocatalyst surface, where they become trapped and initiate oxidation and reduction reactions with adsorbates.[19,26] The hole's redox potential is notably high (+2.53 V vs SHE at pH 7)[1] making it an effective oxidizing agent, while the photoexcited electron exhibits strong reducing capabilities due to its low redox potential (-0.52 V vs SHE at pH 7).[28] The positively charged holes can oxidize OH^- or H_2O, to produce hydroxyl radicals ($^•OH$) (equation 1.2), whereas conduction band electrons reduce molecular oxygen (O_2) to produce superoxide anion ($O_2^{-•}$) (equation 1.3). These anions may further react with H^+ to generate the hydroperoxyl radical ($^•OOH$) and hydrogen peroxide (H_2O_2) (equations 1.4 & 1.5). The photocatalytic mechanism, such as pollutant degradation, operates through a radical chain reaction, generating reactive oxygen species such as $^•OH$, $O_2^{-•}$, and $^•OOH$ which subsequently react with surface-adsorbed species, ultimately degrading them to CO_2 and H_2O.[29,30,19,28,31] Additionally, there's a possibility for electrons and holes to directly react with molecules adsorbed on the surface.

Despite its popularity, TiO_2 has two serious limitations as photocatalyst. It only is responsive to the UV part of solar light (wavelength < 400 nm) which comprises only 4% of entire solar spectrum and there is a fast recombination of photogenerated electrons and holes (h^+/e^-) which results in a low photocatalytic

---

[1] The standard hydrogen electrode or SHE, is a redox electrode that forms the basis of the thermodynamic scale of oxidation-reduction potentials. It is a reference electrode against which the electrode potentials of all electrodes are measured. When hydrogen gas at 1 atm-pressure is adsorbed over a platinum electrode dipped in 1M HCl at 25 °C, the SHE potential is, $E^0 = 0$ V).[27]

efficiency.[10,32] For comparison, band gap energies of different popular semiconductors are compared with anatase TiO_2 in **Figure 1.4.**
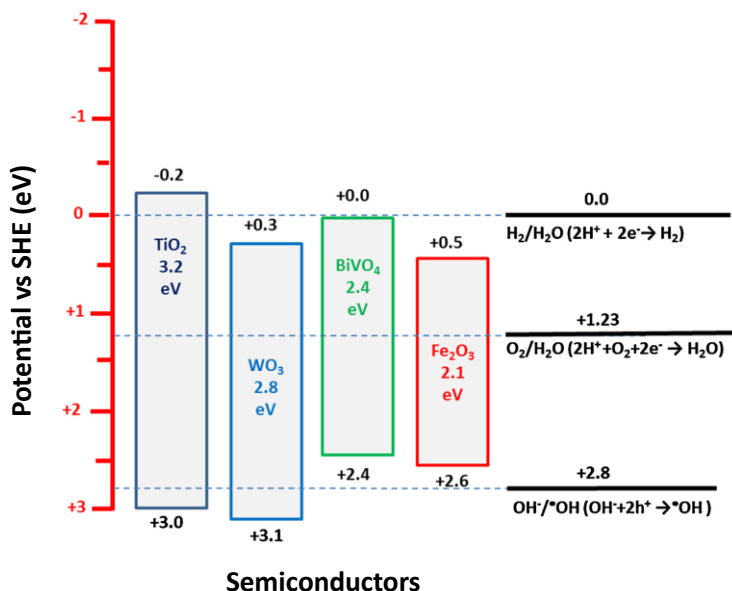
Figure 1.4. Energy states and band gap energies of a few popular oxide semiconductor photocatalysts. All values are expressed vs SHE (corresponding to pH 0). Figure is adapted from ref. [8].

To overcome these two limitations and to optimize the performance of TiO_2 under visible light, researchers have explored various modifications of titania such as, specific ordered nanostructures to transport the photo-generated charge carriers to the other side of the PEC cell,[33,34] band gap engineering, and surface modification with metal nanoparticles.

1.2. Nanoparticles and plasmonic photocatalysis

The deposition of metal nanoparticles has been extensively studied as a strategy to enhance the capabilities of TiO_2-based photocatalysts. Nanoparticles/nanoclusters (NPs/NCs) are small pieces of matter, typically composed of a few to 10^5 atoms and have sizes < 100 nm in all directions. They have received much attention in the scientific research for the last few decades due to their unique and enhanced properties, which can be very different from the corresponding bulk properties, and their numerous applications in many fields, especially in medicine,[35] healthcare, electronics,[36] and energy related fields,[37] as well as in environmental applications.[38,39] At the nanoscale, quantum

effects become dominant leading to altered physical, chemical, optical, mechanical, electrical and thermal properties, which serve as a suitable platform to create innovative materials that would open up infinite possibilities for technological advancement.

For example, gold NPs smaller than 10 nm exhibit a strong plasmon resonance, which is a collective oscillation of free conduction electrons in a noble metal when irradiated by light, that is highly interesting for catalysis or solar energy conversion.[40] The gold plasmon resonance enhances the absorption of light and increases the generation of electron-hole pairs in the photocatalyst. Au NPs are chemically inert and resistant to corrosion under various environmental conditions.[41] Silver NPs in the range of 1 to 100 nm are promising nanomaterials with antibacterial properties that exhibit increased chemical activity due to their large surface to volume ratios and crystallographic surface structure.[42] The antibacterial properties of Ag NPs can be beneficial for applications involving water purification and disinfection.[43] Similar to gold, silver NPs also exhibit strong surface plasmon resonance effects, enhancing light absorption and increasing the photocatalytic activity. Copper is more abundant and less expensive compared to gold and silver, making Cu NPs a cost-effective alternative for large-scale applications.[44] Cu NPs are effective in redox reactions and also can improve the overall catalytic performance of photocatalysts. Copper nanoparticles can facilitate electron transfer processes, which are crucial for photocatalytic applications such as pollutant degradation and hydrogen production.[45]

NPs can also play a vital role as cocatalysts in addressing environmental challenges. They can be employed for water purification, soil remediation, and air purification. Their unique properties enable efficient removal of pollutants and contaminants from various aqueous and solid environmental matrices such as surface water, ground water, drinking water, soil solutions, soils, sedimentary matter, etc. With the possibility of imaging and designing nanoparticles through the invention of electron microscopes,[46,47] researchers have started to produce various types of NPs and manipulate their properties at the atomic level, driving the rapid development of the nanotechnology field. These NPs are of particular interest in photocatalysis and photoelectrocatalysis because they can act as individual active sites, and minor changes in size and composition can have a substantial influence on the activity and selectivity of a chemical reaction.

Most of the metal NPs nowadays are synthesized in solution by wet chemistry methods that generally include inorganic acids, ligands, surfactants, and functional groups that protect and stabilize the NPs.[48] The choice of ligands is of utmost importance for the colloidal stability and function of the NPs. Moreover, the selection of ligands employed in NPs synthesis can determine

their final size and shape. Ligands added after NPs synthesis infer new properties and provide enhanced colloidal stability. Therefore the use of acids and ligands in wet chemistry synthesis methods can have significant influence on the properties of the metal NPs,[49] in the context of catalysis this implies their activity, selectivity and stability.[50] Wet chemical methods dominated the research due to their ability to provide suitable amounts of NPs for industrial applications. Physical methods, though further from large production to scale up to the industry, can produce NPs with unmatched control over size and composition, and these NPs are ligand-free. This opens up new opportunities to perform fundamental investigations on defined systems. These are important assets in the design of high performance catalysts with enhanced reactivity, selectivity and stability.
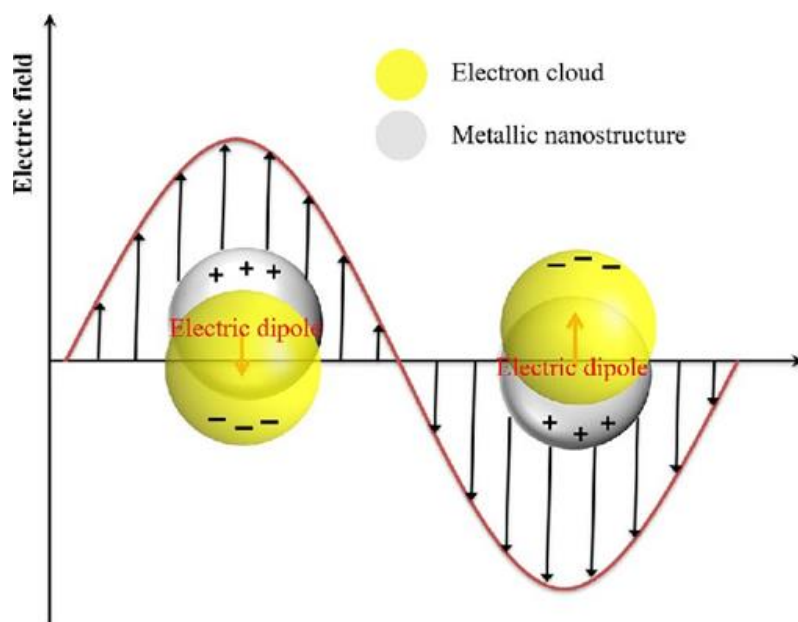
Figure 1.5. Schematic illustration of the LSPR phenomenon in a metallic nanoparticle. The itinerant electron cloud in the metal oscillates along with the electric field component of the incident light, against the restoring force of the positive nuclei, figure adapted from ref. [51].

Plasmonic photocatalysis, in which sunlight as an abundant and renewable energy source is utilized efficiently to drive diverse chemical reactions, has emerged as an expanding research field.[52,53,54] Plasmonic photocatalysis involves doping or deposition of plasmonic metal NPs, with sizes of tens to hundreds of nanometers, into semiconductor photocatalysts to obtain a drastic enhancement of their photoactivity under the visible light irradiation. Au, Ag and Cu are the most popular materials used for plasmonic photocatalysis because of their localized surface plasmon resonance (LSPR) phenomenon. Compared with conventional TiO_2 semiconductor photocatalysis, plasmonic photocatalysis possesses two distinctive features:[55] a Schottky junction and LSPR, each feature has its own advantages in the photocatalytic processes. The Schottky junction arises from the contact between the noble metal and the n-type semiconductor as the work function of the metal is greater than that of the semiconductor. This results in an upward band bending at the metal-semiconductor interface. This contact between metal and semiconductor results in redistribution of charge carriers as electrons are transferred from semiconductor to the metal nanoparticle until the entire system reaches equilibrium. The metal component facilitates a rapid channel for charge transfer,[56] with its surface serving as a center for trapping charges (electron sink), thus reduce the recombination with photogenerated holes that stay at the semiconductor.[57,58,59] Thus, the metal nanoparticle assists the photocatalytic process by promoting interfacial charge transfer with the Schottky barrier preventing the backflow of electrons from metal to semiconductor.[11,57,60]
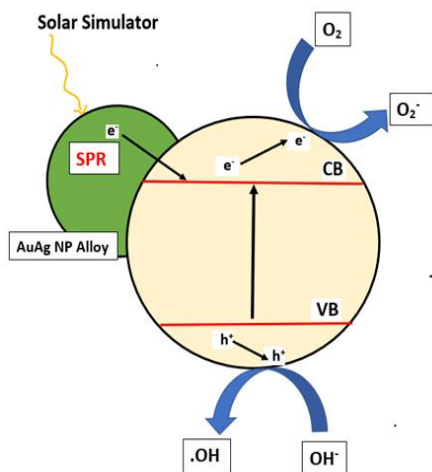
Figure 1.6. a) Schematic representation of plasmonic photocatalysis using alloy AuAg nanoparticles.

LSPR is the coherent oscillation of free conduction band electrons with concurrent light. [51,61,62,63] It occurs when electromagnetic radiation of the right wavelength irradiates a metal NP much smaller than the wavelength of incident light, the electric field component of the incident light interacts with the NP's electrons, causing the collective electron density to oscillate at a frequency of the incoming light as schematically shown in **Figure 1.5.**[64,65] The LSPR effect enhances the light absorption and leads to strong field enhancement effects around the NPs. The oscillatory electron movement induced by surface plasmon resonance implies energy transfer from the incoming light to the electrons, partially extinguishing it. When the wavelength of the incoming light approaches the plasmonic wavelength, more energy can be transferred resulting in an increased light absorption.

The plasmonic wavelength is defined by several key factors such as dielectric function of the metal, the size and shape of NPs, and the surrounding medium. The resonant wavelength is red-shifted if the surrounding medium has a higher dielectric constant (ε).[66,67] The resonant wavelength is also redshifted when the nanoparticle size increases.[68] Similarly, it depends on the particle's shape. For particles of a comparable size, but a shape variation from spherical to pentagonal and then to triangular, the resonant wavelength was found to be shifted from 445 to 520 nm and then to 670 nm.[69] In plasmonic photocatalysis, the noble metal NPs (e.g. Au nanospheres) could have different contact states with the photocatalyst (e.g. TiO_2). They could contact only through the surfaces, or the NPs could be fully (or partially) enclosed by the photocatalyst. For example, the resonant wavelength was found to red-shift from 350 to 430 nm with the increase of the contact area in the case of silver nanosphere (radius 10 nm) embedded into a mica shell (10 nm thick).[70]

The schematic representation of plasmonic photocatalysis is given in **Figure 1.6.** The physical processes taking place in it are: 1) Efficient separation of generated electrons and holes is achieved through Schottky barrier as explained above. 2) Extension of the operational window of TiO_2 (wide band gap semiconductor) from the UV to the visible range. 3) The resonance wavelength of Au or Ag or Cu NPs or their alloys can be tuned depending on their size, shape, composition, and surrounding environment.[70] 4) LSPR generates a concentrated local electric field, promoting photocatalytic reactions by facilitating the excitation of more electrons and holes in the enhanced electric field,[71] and heating the surrounding environment to enhance redox reaction rates (heating effect).[61] 5) Intense absorption ensures that most incident light is absorbed in a thin layer (~10 nm) beneath the surface, reducing the distance between photoexcited electrons and/or holes and the surface, making it comparable to

the minority carrier diffusion length ($\sim$ 10 nm).[52,72,73] This is advantageous for materials with poor electron transport. 6) Excitation of electrons in metal through LSPR (called hot electrons) and injection into semiconductor is done (**Figure 1.6**). Such electrons are called 'hot' because when an electron is excited due to LSPR, its energy becomes larger than in the classical Maxwell Boltzmann distribution at ambient temperature. As a result the electron is not in thermodynamic equilibrium anymore with the atoms in the material and so is called 'hot'.[74] The energy of hot electrons in Au and Ag nanoparticles typically ranges between 1 and 4 eV.[52,75,74,76] These highly energetic hot electrons can be subsequently transferred into a semiconductor if their energy exceeds the Schottky barrier height. The barrier height is relatively small (approximately 1 eV) for Au/TiO$_2$ and Ag/TiO$_2$, facilitating the transfer of hot electrons across the barrier.[77] Research conducted by the group of Moskovits indicated that even electrons with insufficient energy to overcome the Schottky junction can still tunnel across the metal-semiconductor interface, although the possibility is lower.[78,73] Following electron injection into the semiconductor, the plasmonic nanoparticle becomes positively charged, necessitating the presence of an electron donor or a hole transporting species to restore charge balance.[74]

1.3. Photoelectrochemical reactions

The term "photoelectrochemical" indicates the coupling of light with electrochemical reactions. This term encompasses the overall chemical processes that occur when reactants are exposed to light and an applied potential. It includes not only catalytic reactions but also the generation and transport of photoexcited charge carriers, which can contribute to various electrochemical processes such as water splitting or energy storage. Photoelectrocatalysis is typically carried out in a photoelectrochemical cell (PEC), which operates based on the interaction between a semiconductor and an electrolyte at their interface. PEC cells were reported already in 1839 by Edmond Becquerel.[79] A detailed description of a PEC cell and operation principles will be given in experimental section 2.9 of chapter 2.

In this thesis we will make use of PEC water splitting. This reaction was first discovered by Fujishima and Honda using TiO$_2$ as a photoanode and Pt as cathode.[6] It is electrolysis of water by the direct use of light in the presence of a photocatalyst. Semiconductor oxide photoelectrodes TiO$_2$, Fe$_2$O$_3$,[80,81] WO$_3$,[82,83] BiVO$_3$,[84] and CdS and CdSe[85,86] and other advanced nanomaterials such as yttrium vanadate (YVO$_4$)[87], CuInS$_2$[88] and g-C$_3$N$_4$[89] have been used for designing PEC devices to oxidize water and generate molecular oxygen and hydrogen.

TiO$_2$ has been recognized to be an excellent electrode material for PEC water splitting,[90] due to its favorable band structure (**Figure 1.4,** the conduction

band edge should be more negative than the reduction potential of the target reaction and the valence band edge should be more positive than the oxidation potential of the target reaction), good optical stability, chemical inertness, photostability and cost efficiency.[91] Various morphologies of TiO_2, including nanospheres, nanobelts, nanotubes, and nanoflowers, have been investigated for diverse catalytic purposes. Among these, TiO_2 nanotubes (TNTs) fabricated through anodization stand out due to their advantageous properties such as high electron mobility, chemical stability, large surface area, and photoconversion efficiency. However, their optical absorption primarily occurs in the near UV region, and the significant recombination of excitons (electron-hole pairs) hampers their practical use as mentioned earlier.[92,93] The modification of TNTs with other materials or dopants can address these limitations. One promising approach involves the incorporation of noble metal NPs such as silver, gold, or copper which can enhance optical absorption and improve the efficiency of TNTs in PEC applications.[94,52] TNTs are used as photoanodes in PEC cells in this PhD thesis.
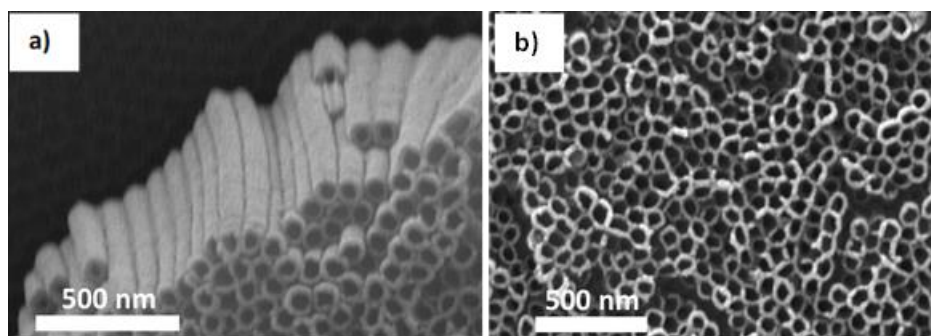
Figure 1.7. Scanning electron microscopy image of TNTs: a) cross-sectional view b) top view, measured with FEG-ESEM-Thermo Fisher Scientific Quanta 250 at an accelerating voltage of 20 kV, courtesy to Karthick Raj Ag (University of Antwerp) for providing the image.

Highly ordered and vertically oriented TNTs have been studied extensively in PEC devices for water splitting.[95,96] They still represent an important subject in the development of PEC devices nowadays, even though further engineering[97] is needed to optimize their performances. They are fabricated through the electrochemical anodization of Ti foil in a fluoride ion containing electrolyte.[98] A scanning electron microscopy (SEM) image of TNTs is given in **Figure 1.7**. The cross-sectional view of TNTs as shown in **Figure 1.7a**

reveals that the nanotubes have a length of approximately 800 nm and are quite regularly ordered. The top view, as depicted in **Figure 1.7b**, indicates that the diameter of the nanotubes is around 80 nm. The application of TNTs for water oxidation will be discussed in section 1.4.2.

Photoelectrocatalysis brings together the synergies between photocatalysis and electrocatalysis, using light to initiate chemical reactions, with potential applications in the development of sustainable energy technologies.

1.4. Application of TiO$_2$ supported BNPs

After introducing the mechanisms and principles involved in photocatalysis, plasmonic photocatalysis and photoelectrocatalysis, this section focusses on the applications of NP/NC-modified TiO$_2$ as photocatalyst and NP/NC-modified TNTs as photoanode.

1.4.1. NP/NC-modified TiO$_2$ as photocatalyst

TiO$_2$ is considered promising as a 'photoresponsive' wetting material after the discovery of its photoinduced superhydrophilic behaviour reported by Wang et al. in 1997.[99] Its ability to decompose and degrade organic pollutants on its surface, makes TiO$_2$ a good self-cleaning photocatalyst in the midst of contaminated, unhygienic, polluted, fouled, or infected surfaces. Due to the photoinduced hydrophilicity of TiO$_2$, organic dirt molecules are adsorbed onto the TiO$_2$ surface. When excited with UV light, those molecules are decomposed in a photocatalytic process. In self-cleaning applications outdoor, rain water subsequently washes away the decomposed or degraded fragments, leaving the surface clean and sterilized.[100,101,102] Since TiO$_2$ is only UV responsive, the possibility to extend the photodegradation towards visible light has been investigated by addition of metal NPs like Au or Ag. It was shown by Alvero et al.,[103] that mesoporous titania containing Au NPs is an efficient photocatalyst for visible light decontamination of Soman (IUPAC - 2,2-trimethylpropyl methylphosphonofluoridate is an extremely toxic chemical substance and it is a nerve agent, interfering with normal functioning of the mammalian nervous system[104]). For this, light intensity of 4300 Lx (measured with an 840006 Speer Scientific luxmeter) was used. When the degradation of Malathion (IUPAC - diethyl 2-dimethoxyphosphinothioylsulfanylbutanedioate is a pesticide) is monitored under visible and UV light for Au/TiO$_2$ nanocomposites, it was observed that the presence of gold accelerates the photocatalytic degradation and allows photodegradation under sun light for 67% which is higher than the 6% photodegradation under UV light compared to material without Au. This

could be attributed to the Au induced prevention of electron-hole recombination.[105] The optimal loading of Ag in crystalline TiO_2 was found to strongly enhance the photocatalytic activity of TiO_2 in the degradation of acetamiprid at 25^oC. In their study, the photocatalytic degradation velocity constant (k) was found to increase quickly with the increase of the Ag mole percent from n = 0.02 to 0.06, while the rate decreased slowly when mole percent was further increased from n = 0.08 to 0.12. The best degradation efficiency is thus found for a mole percentage of Ag in TiO_2 between 4% and 8%.[106]

Compared to monometallic NPs, bimetallic nanoparticles (BNPs) on TiO_2 potentially exhibit higher photocatalytic activity or a higher selectivity due to synergy between two metals or a metal and metal oxide.[107,108] For instance, in BNPs, one metal can act as an electron donor while the other acts as an acceptor, improving the overall catalytic efficiency.[109,110] It was recently shown that the combination of ultra-low amounts of Au (< 0.1% wt) with FeO_x NPs supported on CeO_2 can provide the selective oxidation of glycerol to glyceric acid with a high yield, while monometallic Au and Fe catalysts were almost not active in the reaction.[111] The electronic properties of BNPs can be fine-tuned by adjusting the ratio of the two metals.[112] BNPs often show improved thermal and chemical stability compared to their monometallic counterparts. The presence of a second metal can help stabilize the nanoparticle structure and prevent degradation during catalytic reactions. For example, mixing of gold and silver increase the stability and protects Ag from further oxidation.[113] The unique properties of BNPs make them suitable for a wide range of applications. They are, for example, used for chemical synthesis, environmental remediation, and energy conversion processes.[114]

The effect of depositing BNPs such as Au-Pt, Au-Cu and Au-Ag, on TiO_2 has demonstrated to be promising for the removal of organic pollutants. Such deposition increases the activity and selectivity in the oxidation–reduction processes of inorganic pollutants in water, such as NH_4 and NO_3. Formic acid as a hole scavenger for inhibiting the mechanism of electron-hole recombination, H_2 as a reducing agent, and CO_2 as buffer agent all influenced the photocatalytic reduction of nitrate catalyzed by Pd-Cu BNPs/TiO_2 with high selectivity and activity. The palladium noble metal by itself does not present activity for nitrate reduction, but is effective for nitrite reduction. Therefore, nitrite migrates to palladium sites, where it is further reduced to the end-products, N_2 and/or NH_4^+.

Both metals are reduced by the action of hydrogen, completing the catalytic cycle.
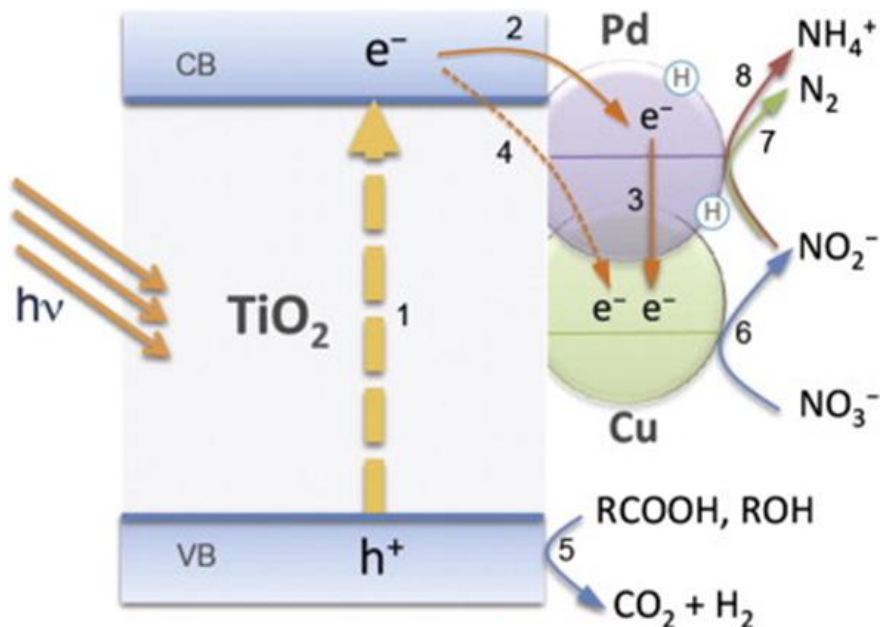
Figure 1.8. Schematic representation of nitrate photocatalytic reduction reaction mechanism over the Pd–Cu NPs/TiO$_2$ catalyst in the presence of H$_2$ and CO$_2$: (1) TiO$_2$ photo-excitation and charge separation; (2) electron transfer to Pd nanoparticles; (3) electron transfer to oxidized Cu; (4) electron transfer to Cu nanoparticles; (5) oxidation of organic compounds by photo-generated holes; (6) nitrate reduction towards nitrite over Cu nanoparticles; (7) nitrite reduction towards nitrogen over Pd nanoparticles; (8) nitrite reduction towards ammonia over Pd nanoparticles. Figure is adapted from ref. [115].

A schematic presentation of mechanism involved in this photocatalytic process is given in **Figure 1.8**.[115,116] The modification by Au-Cu BNPs increases the photocatalytic activity for phenol degradation under UV light (355 nm). A faster degradation was obtained with Au-Cu 1:3 / TiO$_2$ P25 with highest rate constant being $(0.0125 \pm 0.0015) \times 10^{-3}$ s^{-1} (TiO$_2$ P25 is a TiO$_2$ nanopowder which contains higher anatase and rutile phases). 80% of phenol was degraded after 3 minutes (the initial concentration of phenol is 2×10^{-4} M which is equal to 18.82 ppm). It was observed that under UV radiation, Au-Cu 1:3 acts as more efficient electron scavenger than the monometallic counterparts, hindering charge recombination in the modified TiO$_2$ P25. Here, metal nanoparticles act as a sink for electrons, decreasing the charge carrier recombination.[44] A

15

considerable increase in the photocatalytic activity in the reaction of phenol degradation under visible light was observed for 1 to 5 nm Pt-Pd BNPs deposited on TiO_2 with specific surface area 91 m^2/g. The average degradation rate of a particular Pt-Pd BNP modified TiO_2 sample with 0.5 mol% of platinum and 0.5 mol% of palladium was 6.84 µmol dm^{-3} min^{-1} for phenol, which is about 19 times greater than for pure TiO_2 (i.e., the degradation rate increased from 0.42 to 6.84 µmol dm^{-3} min^{-1}). This increase was attributed to the synergistic effect of the bimetallic noble metal photocatalysts.

The presence of noble metal particles on TiO_2 surface can lead to efficient charge separation by trapping or removing electrons from TiO_2. As a consequence of the improved separation of electrons and holes, they are readily available to participate in chemical reactions (transferring holes to create $^{•}$OH radicals, and electrons to dissolved oxygen), thus enhancing the photocatalytic activity.[117] Since every composition has a well-defined LSPR resonance frequency, 'rainbow' photocatalysts (for example, TiO_2 modified with Au_xAg_{1-x} of various sizes and compositions) have been developed. They are ensembles of particles that together cover a broad range of the entire light spectrum, i.e. the rainbow. Gold-silver nanoparticle rainbow catalysts were found to have an efficiency (formal quantum efficiency, FQE) that is approximately 50% better than TiO_2 for stearic acid degradation, a prototypical test for the self-cleaning nature. A catalyst containing specifically $Au_{0.3}Ag_{0.7}$ alloy NPs induced an efficiency increase of almost 70% under visible light illumination (λ_{max} = 490 nm). This is due to the excellent match between the catalyst's peak plasmon wavelength and λ_{max} of the light source used.[118] Plasmonic 'rainbow' NPs (2 wt %) supported on TiO_2 P25 and coated by a protecting layer exhibited a 56% increase in efficiency compared to pristine TiO_2, combined with a good stability under Air Mass 1.5G simulated sunlight due to the stabilizing effect of an insulating polymer shell which intensifies the near field.[119] Air Mass 1.5G is the standard spectrum at the earth's surface. It is the path length which light takes through the atmosphere normalized to the shortest possible path length, that is, when the sun is directly overhead.[120] An AM number represents the spectrum at mid-latitudes. 1.5 is atmosphere thickness, corresponds to a solar zenith angle of 48.2°. G stand for global which includes both direct and diffuse radiation.

1.4.2. NP/NC-modified TNTs as photoanode

TNTs, a self-organized oxide, formed from a titanium metal film, is one of the explored systems in photocatalysis[121] particularly in solar cells, environmental purification, water photolysis, gas sensing and bio-medical applications,[122,123] because it combines a unique morphology with the

semiconductive nature of TiO_2. It has a high porous structure which results in a large surface area that allows for more interaction between the nanotubes and incident light, leading to enhanced light absorption. TNTs are chemically stable and have a highly ordered architecture.[124] The tubular morphology of TiO_2 may act as a light trapping system allowing the incident light to undergo multiple reflections within the tubes, thus increasing the optical path length, which can ultimately contribute to an enhanced photocurrent. The elongated and interconnected TNTs also allow for facile diffusion and movement of charge carriers along the tube walls, minimizing the recombination of photogenerated charge carriers (electrons and holes). This efficient transport of charge carriers to the electrodes in a PEC cell contributes to generation of higher photocurrent.[125] The morphology of TNTs can be altered through multi-step anodization, significantly impacting the orderliness and uniformity of the tubes. This, in turn, has a consequential effect on the photocurrent. For example, the photocurrent density of TNTs synthesized through three-step anodization is about 24 mA cm^{-2} in 0.5 M KOH, which is 2.2 times higher than that of the TNTs (~11 mA cm^{-2}) obtained by a single-step anodization.[126]

As for TiO_2 in general, decoration of TNTs with plasmonic NPs can enhance light absorption at longer wavelengths, in particular in the visible range, and increase the efficiency in PEC reactions.[127,128] Depositing of plasmonic NPs on TNTs, decreases the charge transfer resistance, increases light absorption due to their LSPR behaviour and leads to enhanced PEC activity.[129] Loaded metal NPs can act as an electron trap, assisting in electron-hole separation, and thus enhancing the quantum yield.[130,131,132]
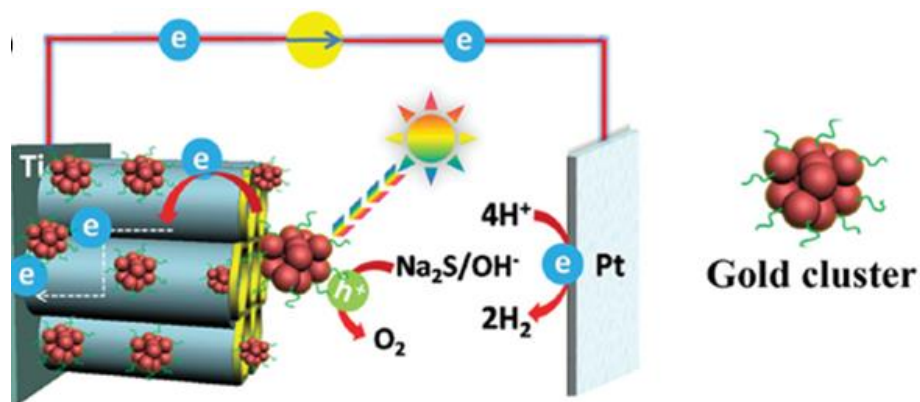
Figure 1.9. Schematic illustration of PEC mechanism with TNTs with gold clusters, adapted from ref. [133].

Several examples in literature demonstrated the positive effect of metal NPs on the photocatalytic activity of TNTs. For example, copper and copper oxide doped TNTs, obtained by adding $Cu(NO_3)_2$ to the electrolyte during the

electrochemical anodization process exhibited a five times higher photocatalytic H$_2$ evolution in comparison to pure TNTs.[134] Au NPs synthesized using an electrostatic self-assembly strategy and deposited on TNTs reinforced light absorption within the visible region, significantly enhancing the PEC water splitting performance.[133] A schematic representation of the corresponding PEC mechanism is given in **Figure 1.9.** TNTs decorated with platinum NPs proved to be highly active and non-poisoning catalysts for PEC oxidation of galactose.[135] Au modified TNTs exhibited a high stability and a high photocurrent of 5.23 mA cm^{-2} at an applied potential of 1 V, which is a 5.19 times higher compared to the corresponding electrode measured in dark. Titanium oxynitride nanotube arrays sensitized with Ag nanoparticles (Ag/TiON) when used to split water photoelectrochemically under AM 1.5 G illumination (100 mW cm^{-2}, 0.1 M KOH), showed a significant increase in the photocurrent (6 mA cm^{-2}) compared to pristine TNTs (0.15 mA cm^{-2}). Moreover, decorating the TiON nanotubes with Ag NPs (13 ± 2 nm) resulted in exceptionally high photocurrent reaching 14 mA cm^{-2} at 1.0 V Saturated Calomel Electrode.[2] This enhancement in the photocurrent is related to the synergistic effects of Ag decoration, nitrogen doping, and the unique structural properties of the fabricated nanotube arrays.[136] The Cu–WO$_3$–TNTs sample showed a photocurrent density at +0.6 V Ag/AgCl equal to 2.3 mA cm^{-2}, which was *ca.* five times higher than that of the Cu–TNTs.[137] In the same work, instead of Cu, Au NPs have been added as dopants for WO$_3$-TNTs. The H$_2$ evolution on the Au / WO$_3$TNTs was three times higher than that on the WO$_3$-TNTs and even nine times higher than that on pure TNTs. Similarly, an enhanced absorbance under visible light and a higher photocatalytic water splitting activity is observed for the Au-CrTNTs and the Ag-CrTNTs fabricated via photodeposition process of noble metals on TNTs.[138] Ag-Cu nanoparticles co-deposited with a molar ratio of 1 to 4 on TNTs via photodeposition exhibited the highest short-circuit photocurrent (JSC) under both solar and visible irradiation.[139]

The development and selection of effective materials for water splitting through PEC cells is still a major challenge today. Much of the literature on PEC water splitting used BNPs synthesized through wet chemistry colloidal techniques, not always with good control over the particle size, composition and coverage, and potential involvement of harsh reaction conditions and reducing agents. In this PhD thesis, we use a unique approach involving physical synthesis by laser ablation and deposition on TNTs in vacuum of small-sized (below 5 nm) AuCu alloy NCs with low loading and precise control over composition and

---

[2] The saturated calomel electrode, SCE, is a reference electrode based on the reaction between elemental mercury and mercury(I) chloride. The aqueous phase in contact with the mercury and the mercury(I) chloride (Hg$_2$Cl$_2$, "calomel") is a saturated solution of potassium chloride in water.

coverage for boosting PEC water splitting performance. This approach opens up new avenues for conducting more in-depth investigations on well-defined systems, aiming to gain a clearer understanding of the underlying mechanisms behind the photocatalytic properties of BNCs. Such investigations are essential for designing novel and highly performing photocatalysts with improved selectivity, reactivity, and stability.

1.5. Objective and outline of the thesis

In this first chapter we have introduced photocatalysis based on TiO_2 in general and TNTs in specific and framed its relevance in a broader perspective of searches for green energy and the mitigation of pollution. The modification of TiO_2 and TNTs by BNPs, using photocatalysis, plasmonic photocatalysis and photoelectrocatalysis, as ways to improve the performance was also discussed. The applications of BNPs modified TiO_2 and TNTs towards degradation of pollutants and water oxidation using light, show that BNPs are suitable photocatalysts for self-cleaning applications and for boosting photocurrents. TiO_2 thin films hold great potential in the development of self-cleaning glass surfaces but suffer from a poor visible light response that hinders the application under actual sunlight since they are only activated by the UV-component of solar light.

The work presented in this thesis goes beyond the state-of-the-art of self-cleaning surfaces that are currently commercially available. We have modified TiO_2 with Au, Ag and Cu alloy nanostructures through the CBD technique, which is presented as an highly controllable alternative to wet chemistry fabrication methods. Soft landing of BNCs produced in the gas phase, maintains their preformed structure with excellent control over size, coverage and composition. This allows for the fabrication of model catalysts for photocatalytic and PEC performances. In this thesis, we focus on the enhancement of self-cleaning surface efficiency (photocatalytic activity) with TiO_2 and higher photocurrent generation (PEC activity) with TNTs modified with nanoalloys made of Au, Ag and Cu. The overall research objective of the PhD thesis can be summarized as follows:

"To design and characterize a new and high-performance photocatalysts and photoanodes for self-cleaning surfaces and for photocurrent generation by getting insight into the influence of the size, elemental composition, shape, atomic structure and oxidation/charge state of AuM (M = Ag, Cu) BNCs."

Following on this introductory chapter, a brief overview of each of the techniques used in the thesis research, with examples from own experimental work is given in **chapter 2**. The article-based chapters 3 and 4, contain the main

results of the thesis. **Chapter 3** gives an elaborate and in-depth discussion on how LSPR, composition-dependent atomic arrangement and geometric structures of gas phase AuAg BNCs-modified TiO$_2$ P25, fabricated through CBD technique contribute to the photocatalytic self-cleaning activity, assessed by monitoring stearic acid degradation both under UV light and simulated sun light. **Chapter 4** will discuss the role of gas phase AuCu alloy BNCs synthesized through CBD technique, deposited on highly porous, ordered TNTs fabricated through one-step anodization, in boosting photocurrent in PEC water splitting reaction. The general conclusions and future perspectives are presented in the final **chapter 5**.

Chapter 2

Experimental setups and characterization techniques

This chapter describes the various experimental techniques and methods that are employed in this doctoral thesis namely, the cluster beam deposition technique, electron microscopy, spectroscopic characterization methods, and the techniques used for photoelectrochemical characterization.

2.1. Cluster deposition apparatus
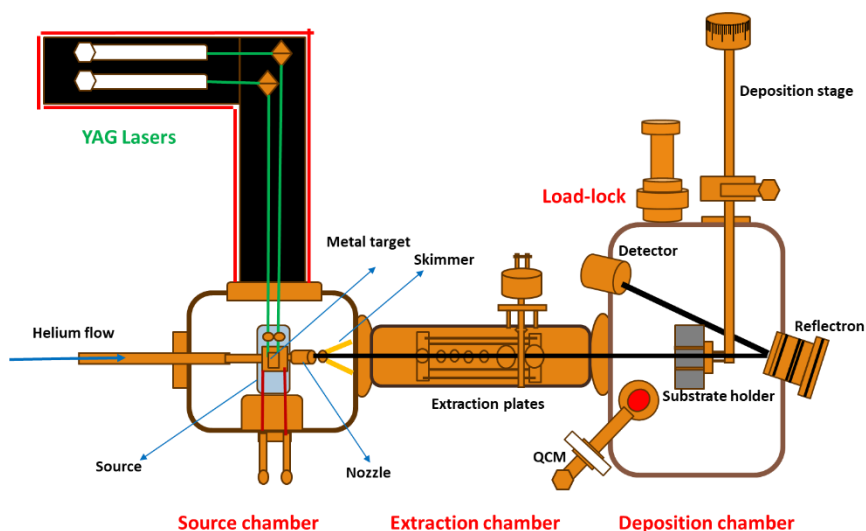
Figure 2.1. Schematic drawing of the cluster deposition apparatus (CDA).

Among a variety of methods for the fabrication of nanoparticles, gas-phase synthesis has drawn attention of the scientific community because of its potential extraordinary control over the particles' size, structure and composition.[140] In gas phase synthesis, nanoparticles are built up from individual atoms or molecules to the desired size. Cluster embryos are formed either by physical means such as condensation of a supersaturated vapor or by chemical

reaction of gaseous precursors. Examples include inert gas condensation,[141,142] plasma,[143] and flame processes.[144] Depending on the embryo concentration, temperature and pressure, these clusters continue to grow to larger entities by addition of atoms, coagulation, and coalescence. In the early 1980s, the development of precise mass (or size)-selected nanocluster molecular beam systems has enabled cluster formation with a well-defined size distribution, which paved the way for new opportunities for understanding gas-phase reaction dynamics and catalysts using atomic clusters.[145,146,147]

Cluster beam deposition (CBD) is a gas phase deposition technique which is central to this PhD thesis, to synthesize well defined, composition- and structure-controlled nanoclusters. In our work, we utilize a laser ablation cluster source for cluster production. The physical aspects of cluster production with a laser ablation source have been described in detail by Michael A. Duncan.[148] Laser ablation of a metal target involves generation of a hot metal plasma of any material using focused light of pulsed lasers. By rapid cooling of the plasma, clusters can be produced.[149,150] The laser vaporization technique was originally applied to the production of clusters in molecular beams by Smalley and co-workers.[146]

Laser ablation offers several advantages.[151] Laser ablation produces high-purity NPs because there is no need to use chemical precursors that can introduce contaminants. This method can be applied to many materials, including metals, semiconductors, and insulators, making it very versatile. The size and composition of NPs can be fine-tuned by adjusting laser parameters such as wavelength, pulse duration, and energy. This control is crucial for tailoring the properties of NPs for specific applications. Laser ablation is environmentally friendly compared to chemical synthesis methods that may use hazardous chemicals. The setup for laser ablation can be easily modified for different materials and conditions, offering significant flexibility. Additionally, NPs produced this way often do not need extensive post-processing to remove by-products or residual chemicals, simplifying the production process.[152]

A detailed view of CDA used in the thesis is presented in **Figure 2.1**. The CDA setup consists of four chambers: i) a source chamber for cluster production using laser ablation and inert gas condensation; ii) an extraction chamber for acceleration of charged clusters for mass spectrometry purposes. Charged clusters that reach the extraction chamber are accelerated towards the microchannel plate (MCP) detector by uniform electric fields. Those fields

originate from voltages (in the order of a few kilovolts) that are applied on the extraction grids; iii) a deposition chamber for soft-landing of the clusters on different kind of substrates and with a quartz crystal microbalance (QCM) for flux measurements and an *in-situ* reflectron time-of-flight mass spectrometer (RToF-MS); and iv) a load-lock for sample transfer.[153,154,155] All four vacuum chambers have a base pressure in the order between 10^{-7}- 10^{-8} mbar and a working pressure between 10^{-5} and 10^{-7} mbar.

2.1.1. Cluster production by laser ablation and inert gas condensation

The clusters production starts in the source chamber by laser ablation. Metal targets with dimensions 15 mm × 25 mm × 1mm or 7 mm × 25 mm × 1mm are ablated through focused green laser light of pulsed Nd: YAG lasers (Spectra Physics Quanta - Ray INDI, λ= 532 nm). The laser creates plasma of evaporated material, which nucleates into small clusters through collisions with helium gas (purity 99.9999%) that is introduced in the source at a stagnation pressure of 7.5 bar by a pulsed supersonic valve (Jordan C-211 PSV, repetition rate 10 Hz). After nucleation the clusters further grow through collisions with target atoms and other clusters, while collisions with the helium gas take care of heat exchange with the source body. The source body is either at room temperature, or cooled down to a temperature of around 200 K, through a continuous flow of liquid nitrogen. A lower source temperature aids the cluster formation process.

The initial nucleation process, *i.e.* the formation of dimers, relies on a three-body collision between two metal atoms and a helium atom. The helium is essential to remove the heat of formation that is set free when a chemical bond is formed between the metal atoms. The cluster formation process and the final size distribution depends on various parameters like the laser energy density, laser timings, pressure of the helium gas, target material properties, and temperature of the source.[156] A careful optimization of these parameters can result in clusters of desired size distribution. Because the pressure inside the formation chamber of the source is much higher (of the order of 100 mbar) as the pressure outside the source (10^{-4} - 10^{-5} mbar), the clusters and the helium gas expand into the vacuum through a nozzle forming a beam of clusters. This expansion terminates the cluster growth as there will no longer be collisions between the particles. A skimmer selects the central part of the cluster beam, which passes on towards the extraction and deposition chambers. Mono- and bimetallic NCs can be produced using single or alloy targets with varying compositions. Since the composition of the alloy target is fixed, produced NCs usually reflect the composition of the used alloy target.[157,158] This was confirmed

by our previous research.[113] Alternatively, the composition of the produced NCs can be controlled with the dual target-dual laser approach, where the laser energy density of the two lasers that ablate the two pure targets can be controlled independently.[156,159] In this thesis, all bimetallic clusters have been made by ablation of alloy targets using a single Nd:YAG laser.

2.2. Reflectron time-of-flight mass spectrometry

The CDA is equipped with reflectron time-of-flight mass spectrometer (RToF-MS) to probe the size distribution of the produced clusters. A cluster beam made by any kind of source always possesses a distribution of clusters of varying sizes and charge states. It is important to know the size distribution before depositing the clusters on the substrate of interest.

The basic principles of time-of-flight mass spectrometry are the following. Ions are accelerated by an electrical field, pass a field free region and impinge on a detector. If the particles have a common starting time, their mass-to-charge ratio can be calculated from flight time. All singly charged particles get essentially the same kinetic energy by traversing electric field. So clusters with the same mass obtain the same velocity,[160] while clusters with different size or mass, travel at different speeds. A detailed schematic representation of the mass spectrometer is given in **Figure. 2.2.**
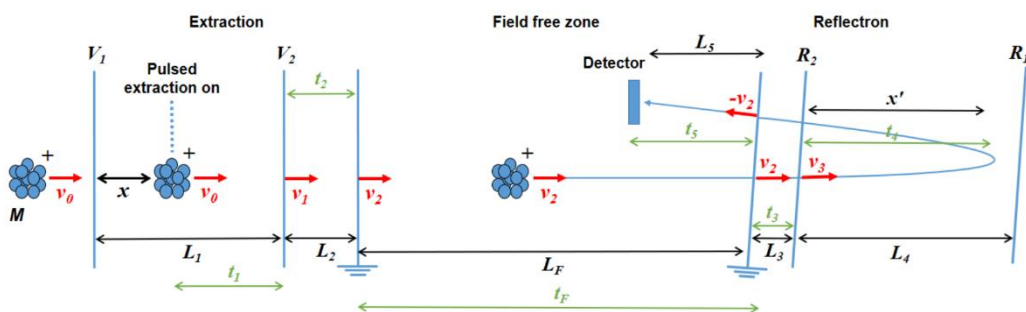
Figure 2.2. Schematic representation of the time-of-flight mass spectrometer. In red, velocities along the flight path are represented (the length of the arrows does not represent the speed). The distance x represents the distance from the first extraction electrode to the position of the clusters where extraction voltages are switched on. Flight times through the different parts of the setup are given in green. Figure is adapted from ref. [156].

After the production, clusters enter the mass spectrometer with an initial velocity v_0. Clusters enter extraction via the first acceleration stage and fly a distance x, measured from the first extraction grid, before the extraction grids are pulsed from ground to high voltage. Positively charged clusters are accelerated in the first extraction zone by an electric field with V_1 and V_2, the voltages applied in a pulsed way on the first and second grid of the extraction. This results in a velocity v_1 at the second extraction grid. The time elapsed from the moment when the potential is switched on to the moment when the clusters enter the second extraction stage is t_1. Then the clusters are accelerated by potential difference V_2 since the third extraction grid is grounded. The terminal velocity of clusters is v_2 and the corresponding flight time through the second extraction zone is t_2. The velocity is constant during the subsequent free flight zone, where the clusters spend a time t_F. Inside the reflectron an opposite potential is applied decreasing the clusters' velocities. Over the first reflectron stage, a potential difference of R_2 is applied, leading to a velocity v_3 at the second grid of the reflectron and the corresponding flight time to travel the distance L_3 is t_3. In the second stage of the reflectron, clusters are further decelerated by an electric field caused by permanent voltages R_1 and R_2, applied to the second and third grid of the reflectron, respectively. The clusters stop at a distance x', measured from the second reflectron grid and the time elapsed from the second reflectron grid to the stopping point x' is t_4. Finally, clusters return (are reflected) the field free zone until they reach the detector, with a corresponding flight time is given by t_5.

The total time of the flight is thus calculated as

$$t_{total} = t_1 + t_2 + t_F + 2(t_3 + t_4) + t_5 \qquad (2.1)$$

The function of the reflectron is to enhance the time or mass resolution of the mass spectrometer. After production, clusters of the same mass enter the mass spectrometer with a distribution of initial velocities v_0. This spread in velocities introduces a spread in detection times, broadening the observed peaks. Resolution in gained by a reflectron because clusters entering the spectrometer with a higher initial velocity will arrive faster at the reflectron but penetrate deeper into it (*i.e.* larger x' distance), while slower clusters will arrive at later times at the reflectron but penetrate it less. For an optimal set of reflectron voltages, these effects on the flight times perfectly cancel out each other, reducing the width of the mass spectral peaks. When the nanoclusters impinge on the MCP detector, the charge of the nanoclusters is amplified and

current signal is converted to a voltage signal. The voltage signal as a function of time is recorded by the digital oscilloscope. [156]

From the time the clusters take to reach MCP detector, mass, number of atoms and diameter of each cluster can be calculated using the formulae given in the next section.

2.2.1. Mass spectra with excimer laser

While the majority of the clusters in the cluster beam are neutral, only the size distribution of charged clusters can be probed by the time-of-flight mass spectrometry described in the previous section as neutral clusters evidently are not accelerated by an electric field. Determining the size distribution of the neutral clusters as produced in the source, is possible by post ionization of the clusters before they are extracted into the mass spectrometer. This post ionization is done with an excimer laser. The excimer laser emits far-ultraviolet light, with photon energies that are high enough for single photon ionization of the clusters. In this thesis an ArF_2 excimer laser that produces light with a wavelength of 193 nm or photon energies of 6.4 eV. If the 6.4 eV is higher than the particles' ionization energy, charged particle are created which then experience the electric field. In general, clusters have a lower ionization energy than single atom. The fraction of ionized particles will be a fraction of the total energy in the excimer pulse, which implies that the intensity of the excimer laser affects the end result. Consequently, when measuring neutral clusters, the extraction time is no longer determined by the moment when voltages are placed on the extraction grids. Instead, it is the firing of the excimer laser that initiates the extraction of the clusters in the mass spectrometer. When studying the size distribution of neutral clusters, the extraction voltages remain continuously applied (so the Behlke switches are not used). This means that ions from the source cannot enter the extraction zone as they are repelled by the high voltage. The distribution observed on the oscilloscope reflects only the neutral clusters that are produced in the source. An example of a mass spectrum of neutral niobium nanoclusters, postionised with the excimer laser, is shown in **Figure 2.3.** The time of flight of the clusters of different sizes is fitted with a parabolic equation. From the time of flight, the mass of the clusters (**Figure 2.3d)** is calculated using:

$$M = a(t_{total} - t_0)^2 + b \qquad (2.2)$$

where 't_{total}' is the time of flight. t_0, a and b are fitting parameters. t_0 is the internal time delay, which is in the first place originating from electronic delays. A typical value for t_0 is 1 μs. For the data in **Figure 2.3c** the slope a equals -1.512 ± 0.025 u/μs^2 and the intercept b is 0.4548 ± 0.0003 u).

From the mass, the number of atoms n (**Figure 2.3e**) and the diameter of the clusters d (**Figure 2.3f**) can be calculated using the formulae:

$$n = \frac{M}{M_{Nb}}$$ (2.3)

where M_{Nb} is the atomic mass of niobium, 92.9068 u.

Assuming a spherical cluster shape, the diameter of the clusters can be calculated from the number of atoms. The volume V is equal to the multiplication of the unit cell volume and number of unit cells contained by the cluster, i.e.,

$$V = a^3 \frac{n}{2}$$ (2.4)

where a = 0.33004 nm is the lattice constant of niobium body-centered cubic structure, $n/2$ is due to the two atoms in one unit cell. A denser material will have smaller lattice constant. Here the density of the clusters is assumed to be the same as bulk density.

Consequently, the diameter d of the cluster with n atoms is:

$$d = 2 \left(\frac{3na^3}{8\pi} \right)^{\frac{1}{3}}$$ (2.5)

Figure 2.3 gives the mass spectrum of Nb nanoclusters. Mass, number of atoms and diameter of the Nb clusters are calculated based on above formulae. The average diameter of the Nb clusters is around 1.5 nm (**Figure 2.3f**). Detailed applications of RToF-MS to determine the diameters of Au_xAg_{1-x} (x = 0, 0.1, 0.3, 0.5, 0.7, 0.9 and 1) and Au_xCu_{1-x} (x = 0, 0.25, 0.5, 0.75, and 1) BNCs produced by various cluster formation conditions using CDA are given in chapters 3 and chapter 4, respectively.
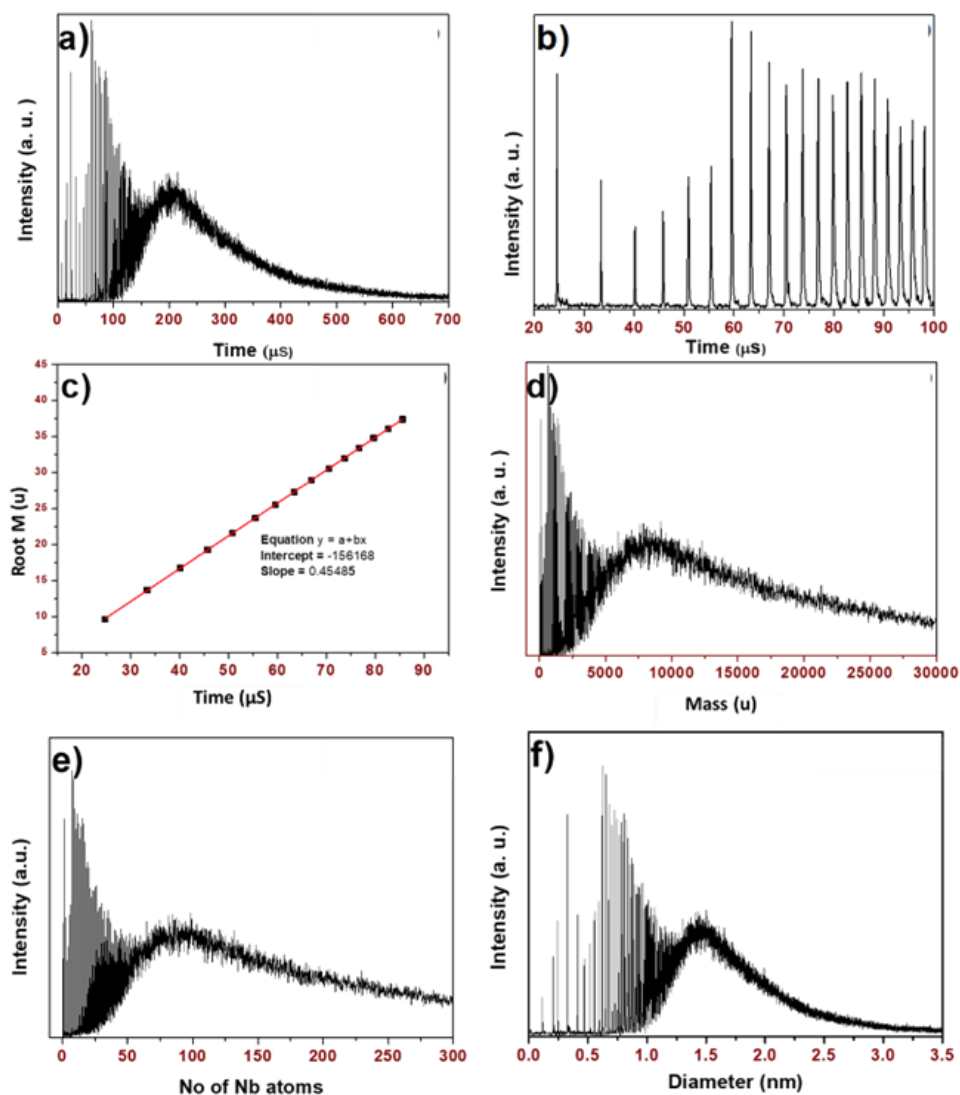
Figure 2.3. (a) ToF spectrum of Nb nanoclusters. (b) Zoom in of the ToF spectrum in (a) up to 100 µs. (c) Mass root as a function of flight time, extracted from (b) and used for the calibration. (d, e, and f) Mass, number of atoms and diameter of the Nb clusters as derived from the ToF spectrum in (a) using equations (2.2), (2.3), and (2.5).

2.3. (Scanning) Transmission electron microscopy

To visualize the structure, size and composition of nanoclusters at nanometer to atomic length scales, (scanning) transmission electron microscopy ((S)TEM) has been employed.

The electron microscope has changed the way humanity sees the micro and nanoscopic world. With today's technology, the electron microscope can zoom in millions of times to where it is able to capture images of individual atoms, whereas traditional microscopes that use visible light cannot image individual atoms due to diffraction limits. The ultimate resolution of light microscopy is limited by the wavelength of visible light, 400 -700 nm. Diffraction limits and lens imperfections limit magnifications of the best transitional microscopes to about 2000 times. When the image is zoomed in further, it becomes blurred without revealing more details. On the other hand, electron microscopy is limited by the wavelength of electrons which depends on the momentum of the electrons through the wave-particle duality:

$$\lambda = h/p \tag{2.6}$$

where h is Planck's constant, and p is the momentum. If p is high enough, this wavelength can be small enough to, in theoretically, obtain subatomic resolution.

The STEM used in this thesis was a probe-lens aberration corrected scanning transmission electron microscope (Jeol, ARM200F instrument) available in the KU Leuven Nanocentre. It was operated at an accelerating voltage of 200 kV, reaching a magnification of 200,000.

A schematic drawing of a typical TEM is shown in **Figure 2.4.** Imaging with TEM starts with the generation of a beam of electrons by the field emission source. It consists of a tungsten crystal needle, and a ring electrode, called extractor, is placed below the tungsten needle. A positive voltage of 5 kV is applied to this extraction ring. As a result, electrons, emitted from the tungsten needle, are pulled towards the extractor. The electric field's effect on the electrons is amplified by the sharply pointed tungsten crystal, which is only a few nanometers wide, and as a result the electrons are freed from the tungsten. To accelerate them to 70% the speed of light, a series of metal rings which are just below the extractor, with tens of thousands of volts apart from one another are used.
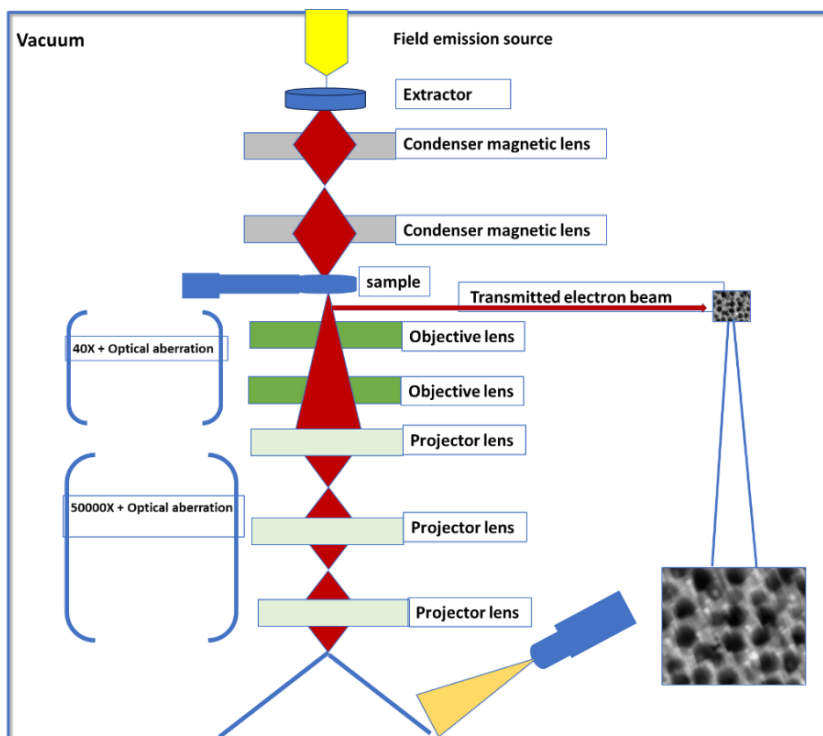
Figure 2.4. Schematic representation of transmission electron microscopy.

These positively charged rings accelerate the electrons further. Because electrons exhibit wavelike properties, the faster they are, the shorter the wavelength. One important detail is that when the microscope is running and electrons are being accelerated to relativistic speeds, vacuum pumps are used to remove all the atmospheric molecules. This is because incredibly fast -moving electrons will scatter in random directions as they collide with air molecules and thus ruin the images of sample. Then, a series of magnetic lenses focusses the electron beam onto a small area and directs them to the sample of interest. Depending on the different densities and materials inside the sample, the transmitted electrons are scattered, thereby imprinting an image of what is inside the sample onto the beam of electrons. The imprinted beam of electrons is then magnified 40 times using an objective lens. It is further magnified another 50,000 times using a set of projector lenses as shown in **Figure 2.4.** Their optical aberrations define the final resolution. At this point, the imprinted

image is large enough to be captured by a high-resolution camera sensor at the bottom of the microscope.[161]
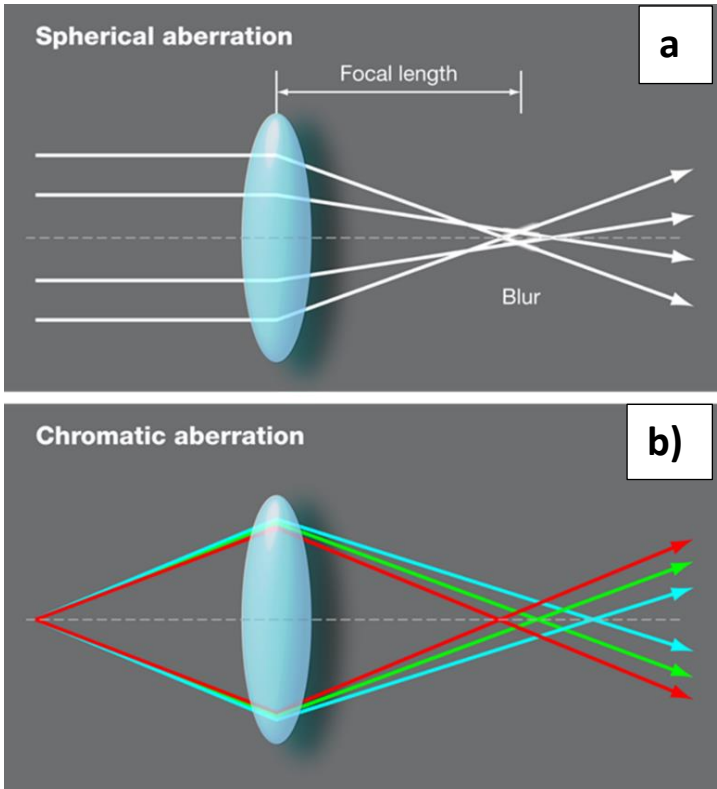
Figure 2.5. a) Spherical aberration: Parallel rays at different distance from the optical axis do not meet after the lens in one focal point. Shorter the focal length, the smaller the spherical aberration coefficient and hence smaller amount of blur. b) Chromatic aberration: The different colors do not meet after the lens in one focal point. The smaller the energy width of the electron source and/or the better the stability of the high voltage (the lens), the smaller the chromatic spread and hence smaller chromatic aberration. Figure is adapted from ref. [162].

To comment on optical aberrations, TEM's ability to resolve the smallest features is not limited by the momentum of the electrons in the beam, but rather by the lenses and the aberrations and distortions that they add to the

image-imprinted electron beam. The most important types of aberration, spherical and chromatic aberrations, are illustrated in **Figure 2.5**. Chromatic aberration is the inability to focus all wavelengths (colors) on the same point. Spherical aberration is the inability to bring all points of the image in focus on a flat surface**.** These aberrations add blurriness and impede resolution after the magnification. They can often be corrected by designing round lenses with negative aberrations. The projector lenses magnify what has already been magnified by the objective lens, including the added aberrations, and this second magnification adds its own aberrations. Therefore, a considerable amount of TEM engineering has been dedicated to reducing the aberrations introduced by the objective lens, as that is what ultimately limits the sub-nanometer scale resolution of the microscope.

STEM can be carried out on a wide range of materials, provided that electrons are able to pass through them. The electron beam cannot readily penetrate samples much thicker than 200 nm. Therefore, the samples must be ultrathin, generally less than 100 nm. Thinning should be done with care to reduce the risk of contamination or damage to the sample surface, as this can affect the quality of the final image. In this study, no thinning process was conducted on the samples since the deposited clusters, approximately 0.5 ML on the TEM grid, are sufficiently thin for the electron beam to penetrate.

STEM vs. TEM

Fundamentally, TEM and STEM are the same technique, with the key difference being that a TEM probe does not scan. Therefore, TEM provides the same benefits of being able to image materials on a nanoscopic scale with a high resolution. However, as the probe does not move across the surface, it is limited to individual scanning areas and does not provide an overall image of the material in the way that STEM does. Typical size of the scanned area in STEM is 1×1 μm^2.

Figure 2.6. provides the TEM images of single TiO_2 nanotube (TNT), showing its anatase crystalline structure on which $Au_{0.25}Cu_{0.75}$ NCs have been deposited. The TNTs with clusters were transferred onto a lacey carbon TEM grid by gentle scratching of the surface. From **Figure 2.6a,** it is observed that the single nanotube has a diameter of 120 nm and a length of 560 nm. Notably, the surface of the nanotube appears rough, likely due to the presence of AuCu NCs. **Figure 2.6b** gives the crystalline structure of TNT with lattice fringes of 0.35 nm, which can be assigned to the d-spacing of the of TiO_2 anatase (101). The transformation of TNTs into the anatase phase was achieved by heating the

anodized titanium film (TNTs grown on titanium film) at 450°C for 2 hours. The benefits of converting as-prepared TNTs to its anatase phase and its influence on PEC activity are extensively discussed in chapter 4.
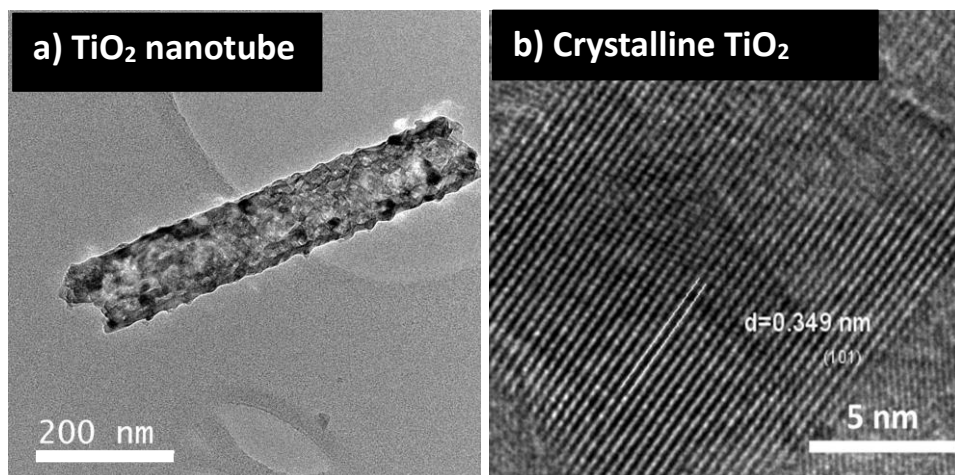
Figure 2.6. TEM image of a) a single nanotube with a rough surface, and b) crystalline structure of anatase TiO_2.

2.4. Scanning Electron Microscopy

Scanning electron microscopy (SEM), is part of the electron microscopy family. In contrast to STEM, which illuminates and captures an entire sample area simultaneously, a SEM generates a focused electron beam that scans across the target object in a raster pattern.

For the work presented in this thesis *ex situ* SEM was done with the Raith GmbH electron beam lithography and microscopy platform available in KU Leuven Nanocentre. It uses an accelerating voltage of 15 kV and an aperture size of 30 μm. A thermal source is used for electron emission. The schematic representation of SEM with its components is given in **Figure 2.7.**

The typical electron source used in SEM is a tungsten filament. When current flows through it, the filament heats up, leading to thermionic emission where some valence electrons gain enough energy to be set free. These liberated electrons are then, accelerated away from the filament by an applied voltage, typically reaching up to 30 kV. This highly accelerated electron beam is focused into a spot using magnetic lenses and directed towards the sample surface and the resulting image is formed from various signals emitted by the

sample. These signals include secondary electrons (low energy), back-scattered electrons (high energy), and X-rays that are generated when core electrons are ejected out and valence electrons fill the created vacancies.[163]

Electron gun

Accelerating anode

Condenser lenses

Objective lens

Back scattered electrons detector

X-ray detector

Scanning coils

Secondary electrons detector

Sample

Sample stage
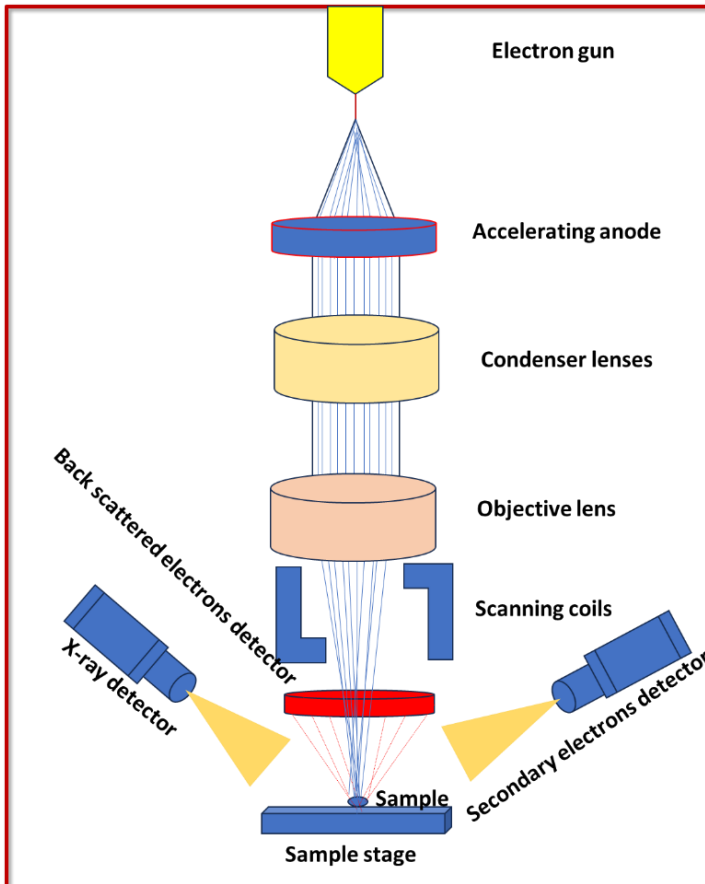
Figure 2.7. Schematic representation of a scanning electron microscopy.

While SEM cannot provide atomic resolution, typical SEM can achieve resolutions of the order of 1 to 20 nm. The maximum SEM resolution depends on multiple factors, including the size of the incident electron beam and the interaction volume of the beam with the sample. Higher accelerating voltages can also provide higher resolution, but the damage to the sample also increases. Therefore, a low accelerating voltage of several kV is favorable for more delicate samples. The choice of electron source also affects resolution. There are two categories of electron sources: thermionic emission sources and field emission sources. A thermionic source is capable of a resolution of 25 nm at 1 kV while a

field emission source can achieve around three nanometers. When we move up to 30 kV, a thermionic emission source is capable of around three nm and a field emission source can achieve around one nanometer resolution. SEM samples should be dry and conductive. Samples containing water cause problems when vacuuming the SEM chamber, also energetic electrons incidence on the sample may evaporate the residual water and reduce image quality. The conductivity of the sample surface is vital to prevent charge build-up on its surface.[164]
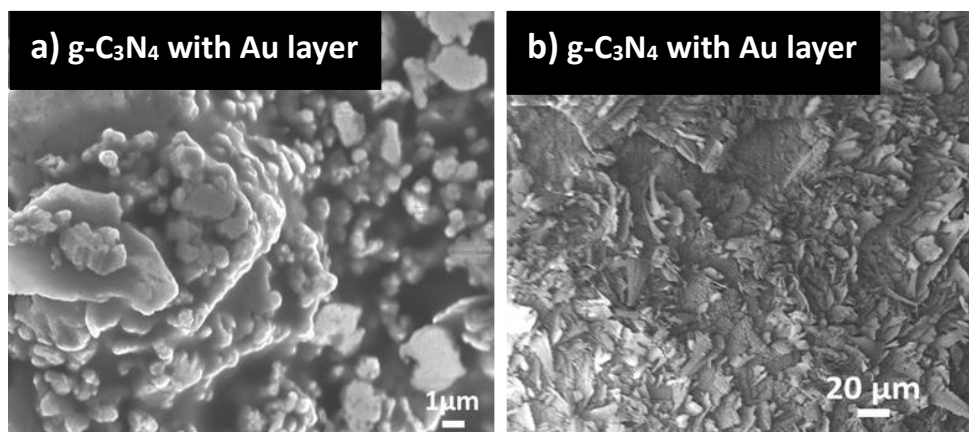
Figure 2.8 a) & b) SEM images of g-C_3N_4 on alumina with thin Au layer with length scales 1 µm and 20 µm.

SEM was used to characterize graphitic carbon nitride (g-C_3N_4) grown on quartz tube with ceramic cap. This was a side project done in collaboration with the research group of Dr. Tibor Höltzl (Furukawa Electric Institute of Technology Ltd., FETI, Hungary). The objective was to examine the surface morphology of g-C_3N_4 samples in preparation for subsequent testing for CO_2 reduction. The limited conductivity of the samples (support is a ceramic material) complicated SEM imaging since the electron beam is distorted by charging effects. For this reason, it was impossible to measure bare g-C_3N_4 samples without any conducting layer on it. To make g-C_3N_4 samples conductive, a thin Au layer was sputtered on top. Even on the samples with gold cover layer, the grounding contact had to be optimized. The use of a copper foil to connect clamp and target holder was helpful in this respect. Still, the charging effects are not fully solved limiting the time to acquire an image before the contrast was lost and thus the ultimate resolution of the Raith system of less than 10 nm

could not be reached. **Figures 2.8a & b** show the SEM images of g-C$_3$N$_4$ with thin Au layer at different length scales. The right image with the length scale 20 μm (**Figure 2.8b)** reveals that thickly populated flake like structures of g-C$_3$N$_4$, while in the left figure with a length scale of 1 μm (**Figure 2.8a)** cauliflower head like formations are seen. The size of such cauliflower formations ranges from 500-700 nm.

2.5. X-ray photoelectron spectroscopy

X-ray photoelectron spectroscopy (XPS) is a surface sensitive technique, which is widely used to identify elements on the surface of solid materials, their chemical states and atomic percentages. It can measure both conducting and insulating materials in variety of forms such as powders, pellets, and thin films. It has been widely applied in industry for characterization of semiconductors, plastics, adhesives, and catalysts.[165] The underlying principle in this technique can be explained as follows. The electrons in any atom have distinct binding energies. When an X-ray photon is absorbed by an atom, the photoelectric effect may result in the emission of a core electron if the photon energy is larger than the binding energy of that core electron. The photo-emitted electron has a kinetic energy (*KE*) equal to the difference of the X-ray photon energy and the electron's binding energy (*BE*) to the nucleus:

$$E_{kE} = h\nu - E_{BE} \tag{2.7}$$

where *h* is the Planck constant (6.62×10^{-34} J s) and *v* is the frequency (in Hz*)* of the impinging radiation. The binding energy (*BE*) is dependent on the chemical environment of the atom making XPS useful to identify the oxidation state of an atom. Since the energy levels in solids are conventionally measured with respect to the Fermi-level rather than the vacuum level, a correction should be made to equation (2.7) in order to account for the work function (Ø) of the solid.[166] The experimentally measured energies of the photoelectrons are thus given by

$$E_{kE} = h\nu - E_{BE}' - \emptyset. \tag{2.8}$$

where E_{KE} is the kinetic energy of the electron as measured by the instrument, $h\nu$ is the energy of the X-ray photons used, E_{BE}' is the binding energy of the emitted photo electron with respect to the Fermi level and ϕ is the work function. The work function term Ø is an adjustable instrumental

correction factor that accounts for the few eV of kinetic energy given up by the photoelectron as it gets emitted from the bulk and absorbed by the detector.
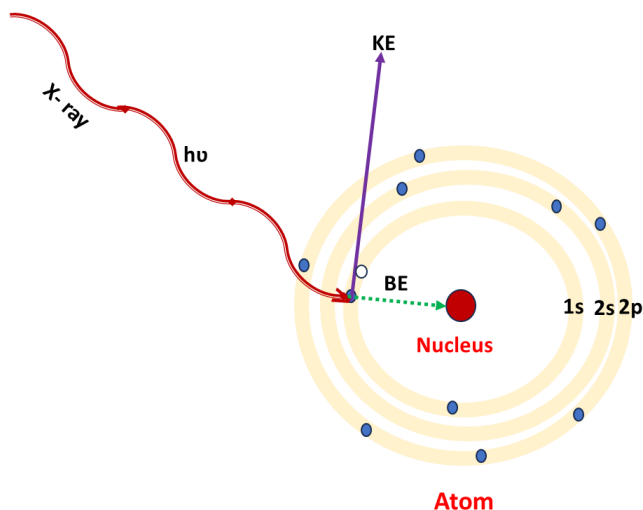
Figure 2.9. Schematic illustration of the principle of X-ray photoelectron spectroscopy, adapted from ref. [167].

X-rays are generated by bombarding a metallic anode with high-energy electrons. The energy of the emitted X-rays depends on the anode material and the beam intensity depends on the energy of the electron. XPS instrument used in this thesis utilizes a twin X-ray anode source with energy 1253.6 eV. It is fitted with two anodes, aluminum and magnesium. To generate X-rays, one of the two thoria-coated iridium filaments is heated and emits electrons, which are accelerated onto the anode. The impact of the electrons on the anode causes X-ray emission. X-ray generation requires the dissipation of a large amount of power by the anode, and the anode must therefore be water cooled.[168] A schematic representation of X-ray source is given in **Figure 2.10**.

The XPS measurements were performed using a laboratory setup equipped with a Mg Kα X-ray source with an energy of 1253.6 eV (XR4 Twin Anode source) and an Alpha 110 hemispherical analyzer. The spectra were acquired with an energy step of 0.1 eV and an energy resolution of 0.5 eV. The sample is kept at room temperature in an UHV (base pressure ~ 10^{-8} mbar) chamber to ensure the absence of collisions of the photoelectron on its way to the detector. The X-ray beam is 5 mm in diameter at the sample and the analyzer

has an aperture of 0.6 mm. X-rays are generated by the electron bombardment of source and focused onto a sample. Emitted photoelectrons escape from the sample surface and travel to the hemispherical analyzer for the determination of their kinetic energy.
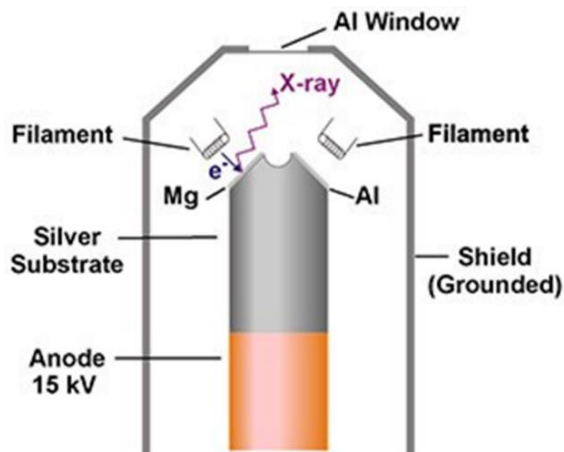
Figure 2.10. Schematic representation of X-ray source, adapted from ref. [168].
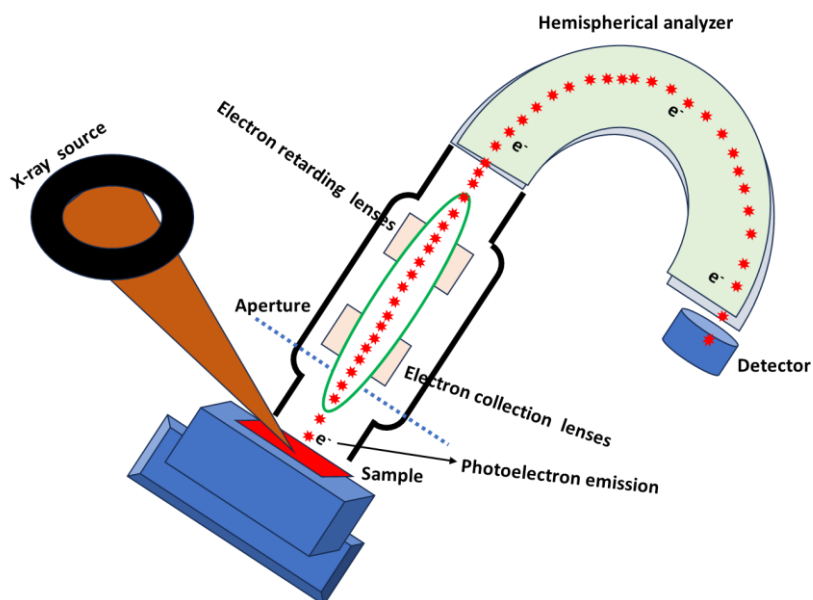
Figure 2.11. Schematic drawing of a typical experimental arrangement of XPS.
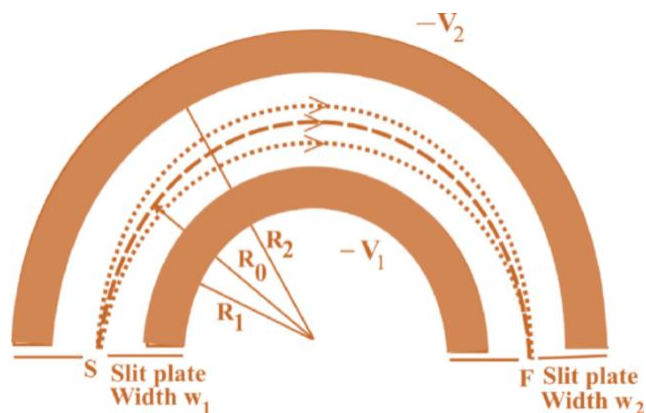
Figure 2.12. Schematic representation of a concentric hemispherical analyzer, adapted from ref. [166].

The components of the XPS instrument used in this thesis, are shown in **Figure 2.11.** It is composed of a photon source, an electron energy analyzer, and an electron detector. The photon energies are within the soft X-ray range and the travel distance of the electron is around 1 meter. X-rays illuminate an area of a sample causing electrons to be ejected (from the upper 1-10 nm of the material, i.e., XPS is surface sensitive) with a range of energies and directions. The electron optics, which consists of a set of electrostatic or magnetic lens units, collects a proportion of these emitted electrons that are transferred through apertures and focused onto the analyzer entrance slit. Electrostatic fields within the concentric hemispherical analyzer (HSA) are designed to only allow electrons of a specific energy to pass through detector slits and reach the detector.[169] Concentric Hemispherical Analyzer uses an electric field between two hemispherical surfaces to disperse the electrons according to their kinetic energy. Schematic representation of a concentric hemispherical analyzer is given in **Figure 2.12.**

Two hemispheres of radii R_1 (inner) and R_2 (outer) are positioned concentrically and potentials $-V_1$ and $-V_2$ are applied to these spheres, respectively, with $V_2 > V_1$. The potential of the mean free path analyzer is[166]

$$V_0 = \frac{V_1 R_1 + V_2 R_2}{2R_0} \qquad (2.9)$$

An electron of kinetic energy will travel a circular orbit through hemisphere at radius R_0. Since R_0, R_1, and R_2 are fixed, changing V_1 and V_2 will allow scanning of electron kinetic energy following free travel through the hemispheres. The main reasons to use a HSA are; first, a good energy resolution, and in the constant analyzer energy mode, the resolution is constant over the entire energy range measured. Second, and even more important is the high transmission, i.e. larger possible count rates enabled by the hemispherical analyzer, since it is focusing in two directions, while a cylindrical mirror analyzer that is a segment of a cylinder only focusses in one direction.

XPS spectra are generated by the count of electrons per second as a function of kinetic energy. Chemical elements in the sample can be identified by matching peak positions to their fingerprint binding energy values. In addition to the identification of elements, XPS can probe the chemical state of each element through the chemical shift effect. This is a unique advantage of XPS compared to other elemental analysis techniques. The chemical shift is the change in core electron binding energies with a change in the chemical bonding of the corresponding atom. The binding energy peak position of a specific element depends on the oxidation state and local chemical environment of that element. In the case a sample is modified, for example by doping with other more electronegative elements, the electron density around the base element decreases and the binding energies of its core electrons increase. Therefore, the binding energy peak shifts positively. Conversely, if the electronegativity of the doping element is lower than the base element, the electron density around the base element increases and the binding energy of its core electrons decrease, leading to a red shift in BE peak position.

2.6. UV-Visible diffuse reflectance spectroscopy

UV-Visible diffuse reflectance spectroscopy (DRS) is a widely used, basic spectrophotometric technique for the analysis of powders and surfaces. It is based on the surface dispersion of incident UV–Vis radiation. A UV–Vis collimated light beam is directed with a certain angle onto the sample and, as a result, an ensemble of optical processes leads to radiation reflection by the sample surface. As a rule, the radiation reflected by a sample consists of specular and diffuse reflection.[170] Specular reflectance occurs when incident radiation hits an ideally smooth and planar surface (i.e. without roughness) of

the sample, and it is then reflected at an angle equal to the angle of incidence (Fresnel law). Instead, diffuse reflectance is diffusing incoming light into a wide range of outgoing directions (at different angles).[171,172] A schematic representation of reflected and diffused reflected light is given in **Figure 2.13**.
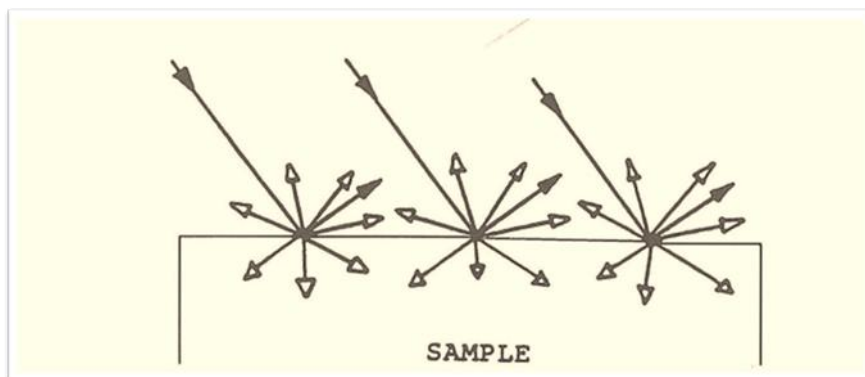
Figure 2.13. Specular reflection is denoted by the shaded arrows and diffuse reflection is denoted by hollow arrows, adapted from ref. [173].

In this thesis, the optical properties of the deposited metal nanoclusters (AuAg and AuCu) on TiO_2 (TiO_2 P25 and TNTs) are investigated using UV-Vis spectroscopy with the double beam UV 2600 spectrophotometer (Shimadzu, Kyoto, Japan) that is available at the University of Antwerp. A schematic diagram of this instrument is given in **Figure 2.14**.

The double beam UV-Vis spectrophotometer is equipped with film holders attached to a $BaSO_4$ coated integrating sphere of 60 mm in diameter. Optical diffuse reflectance spectra were recorded at room temperature and data were collected in the 300 nm to 800 nm range. A pristine TiO_2 P25 sample is used as a reference for the baseline correction. The most important component of the spectrophotometer is the integrating sphere. In a standard direct transmission configuration, light is focused on the light-sensitive surface of the detector. When a sample is introduced, the difference in refractive indexes between the air and the sample causes the focal point to shift, resulting in some transmitted light going undetected. An integrating sphere addresses this by capturing and detecting all transmitted light. The optical system has two light

beams: the sample light beam entering the sphere perpendicular to the sample reflectance window and the reference light beam entering at an incident angle of 8 degrees. Both beams are detected by the centre-mounted detector in the sphere. There are various ways light interacts with a sample. It can pass through the sample in the same direction it travels towards it, resulting in direct transmitted light. Alternatively, it can be refracted and scattered, leading to diffuse transmitted light. The sum of both types is termed total transmitted light. Light can also reflect from the surface of a sample, either through specular or diffusive reflection as explained above using **Figure 2.13.**
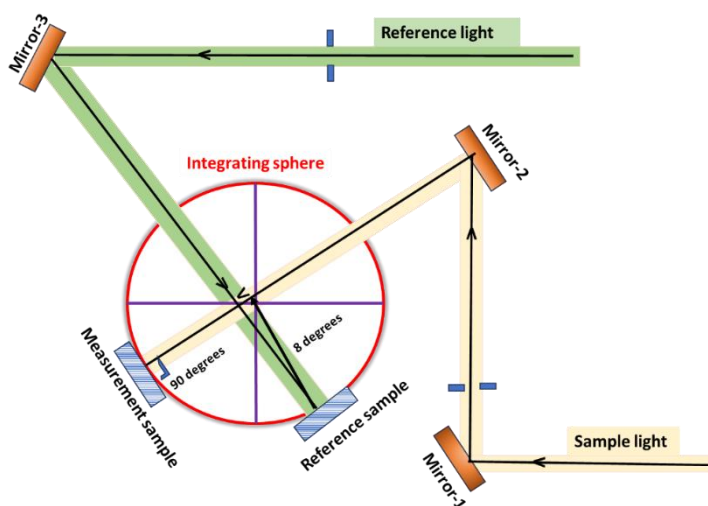
Figure 2.14. Schematic illustration of the operation principle of the double beam UV 2600 spectrophotometer of Shimadzu.

Before measurement, blank or reference samples are placed at both the measurement sample and reference sample windows to run a baseline correction. Then, the blank or reference sample at the sample window is replaced with the sample under investigation. By doing this, all specular reflected light can be removed from the measurement, leaving behind diffuse reflected light in the sphere which is detected by the detector placed in the middle of integrating sphere.[174]

From the diffuse reflectance data, absorbance can be calculated based on the Kubelka-Munk (KM) equation.[170]

$$KM = \frac{1-R^2}{2 \times R}$$ (2.10)

A = -log(KM) (2.11)

where R and A represent the diffuse reflectance and the absorbance, both are wavelength dependent.

2.7. X-ray absorption spectroscopy

Information about the electronic properties, oxidation states, and local atomic environment of cluster samples can be obtained by X-ray absorption spectroscopy (XAS). X-ray spectroscopy uses high-energy X-rays, ranging from a 100 to 50,000 eV, that are typically provided by synchrotrons. In contrast to optical spectroscopy, where valence electrons are excited, XAS involves core electrons occupying innermost shell and which are tightly bound to the nucleus. This distinction leads to various applications and implications. One significant advantage of XAS is that it is element selective, because every element has absorption edges at unique energies. Additionally, high energy X-rays penetrate deep into materials, making them suitable for studying samples with complex structures. X-rays are absorbed by an atom at energies near and above a specific absorption edge[175,176,177] and their absorption spectrum can be collected either in transmission mode by measuring the sample X-ray absorbance or in fluorescence mode by collecting the X-ray fluorescent photons. X-ray absorption spectroscopy specifically focuses on exciting core electrons into unoccupied orbitals, creating a spectrum with three distinct regions namely pre-edge, near-edge (X-ray absorption near edge structure - XANES) and extended regions (Extended X-ray absorption fine structure - EXAFS). A schematic representation of the three regions is given in **Figure 2.15b.**

The pre-edge region corresponds to the excitation of core electrons into low-energy empty orbitals. For 3d transition metals, the pre-edge results from 1s to 3d transitions, with the quadrupole transitions ($\Delta\ell$ = ±2) which are about 100 times weaker than dipole transitions ($\Delta\ell$ = ±1). These are weak transitions that occur before the main absorption edge. XAFS spectra are governed by the dipole selection rule. A photon has angular momentum (ℓ) of 1, so the electron

on the absorbing atom must undergo Δℓ = ± 1 (dipole transitions) in order to conserve momentum. **Figure 2.16** schematically illustrates permitted and prohibited transitions. The intensity of pre-edge can indicate the oxidation state of the atom, with higher oxidation states requiring more energy for the transition. Rising and near-edge, together called XANES, include transitions from core electronic states of the atom to the empty electronic states. The electronic and oxidation states can be obtained from XANES and this information can be derived from shift of the white line, a large, prominent peak just above the edge. EXAFS include transitions from core electronic states to continuum states. The local atomic structure of the element of interest, such as the type, coordination number and distance to neighboring atoms, can be revealed by EXAFS.
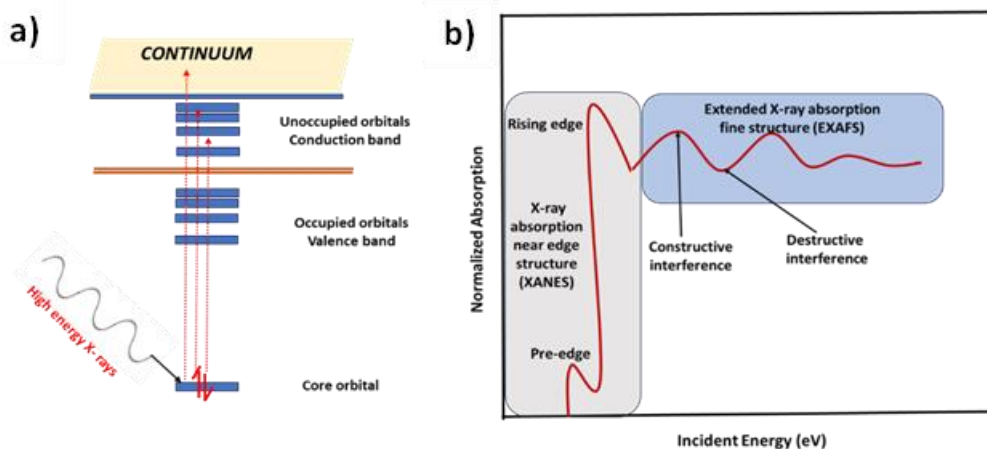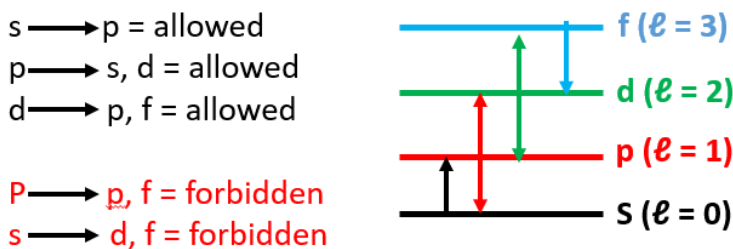

Figure 2.15. a) Illustration of the excitation processes that take place when an X-ray photon hits an atom, and b) example of XAFS spectra.

The XAFS measurements carried out in this thesis were performed in fluorescent reflection mode XAFS (Refl-XAFS) at the BM08 LISA beamline at the European Synchrotron (ESRF). A schematic drawing of a typical experimental

arrangement of Refl-XAFS is shown in **Figure 2.17.** Experimental details are provided in the PhD thesis of Ting-Wei Liao.[178]

s ⟶ p = allowed
p ⟶ s, d = allowed
d ⟶ p, f = allowed

P ⟶ p, f = forbidden
s ⟶ d, f = forbidden

f ($\ell = 3$)
d ($\ell = 2$)
p ($\ell = 1$)
S ($\ell = 0$)

Figure 2.16. Schematic drawing of allowed and forbidden transitions.

X-rays are generated when the direction of a high-energy electron beam circulating in a storage ring of synchrotron is altered. Therefore, the light emission from the energetic electron beam perturbed by the magnetic field is called synchrotron radiation. The electrons are initially generated and accelerated to a few giga electron volts (GeV), such as 6 GeV at facilities like ESRF, through a linear accelerator and a booster ring. Subsequently, the accelerated electron beam is transferred to the storage ring, where the energy of the electron beam is maintained, and provide synchrotron radiation to the beamlines.[179] The change of the direction of electron beam within the storage ring to emit synchrotron radiation is achieved using bending magnets, undulators, and/or wigglers. Undulators are positioned in straight sections of the storage ring, while bending magnets guide the electron beam between these sections. Once synchrotron radiation is produced, it is monochromatized and focused by a series of optical elements. In XAFS measurements, an ion chamber filled with N_2, Ar, or Kr gas is utilized to measure the incident X-ray's intensity I_0. This chamber absorbs approximately 10% of the incident X-ray photons, converting them into a current signal. Different detectors are employed, depending on the sample's nature, to measure the intensity. In transmission mode, an additional ion chamber directly gauges X-ray intensity. Alternatively, in fluorescence mode, a high-purity Ge multi-detector array captures the fluorescence radiation peaks produced by the atoms of interest in the sample. These fluorescence spectra can be transformed into the X-ray absorption signal. With a fixed incident X-ray intensity I_0, stronger X-ray absorption of the sample results in a stronger X-ray fluorescence signal. It can

also be obtained by collecting the photoelectrons generated from the sample by electron detector in total-electron-yield (TEY) mode. The fluorescence and electron-yield signals are correlated to the X-ray absorption and therefore can be converted to absorption signal.

The basic mechanism involved in X-ray absorption measurements is given by Beer-Lambert law which states that the intensity of an X-ray beam passing through a material depends on the thickness t and the material's absorption coefficient $\mu(E)$:

$$I = I_0 e^{-\mu(E)t} , \tag{2.12}$$

where I_0 is the incident X-ray intensity and I is the intensity of the transmitted BEAM. $\mu(E)$ is a function of incident X-ray photon energy E, or wavelength $\lambda = hC/E$, the sample density ρ, the atomic number Z, and the atomic mass A of the material.

$$\mu(E) \approx \rho \frac{Z^4}{AE^3} = \rho \frac{Z^4 \lambda^3}{A(hc)^3} \tag{2.13}$$
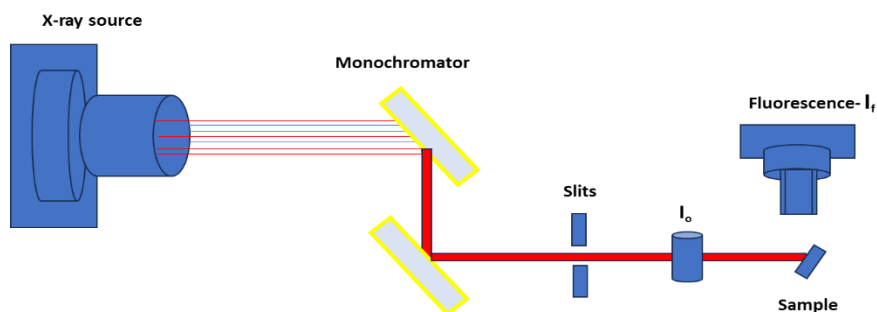
Figure 2.17. Schematic drawing of a typical experimental arrangement of Refl-XAFS.

As the energy of the incident X-ray equals the binding energy of a core-level electron, a sharp rise of the X-ray absorption will occur which is called an absorption edge, and corresponds to an excitation of the core level electrons to the continuum. The kinetic energy of that excited electron is following Einstein's photoelectron equation which is described in equation (2.8).

$$E_{kE} = hv - E_{BE} - \emptyset. \tag{2.14}$$

The decay of the excited atoms can follow two mechanisms: X-ray fluorescence and Auger electron emission. The probability of X-ray fluorescence and Auger electron emission is directly proportional to the X-ray absorption probability.

The binding energy of an electron is determined by the combined effects of the attraction from the positive nucleus and the repulsion from the negatively charged electrons. Therefore, in general, with a higher oxidation state of the metal, the excitation energy required is higher which will result in a blue shift of the absorption edge in the XANES spectrum. The excited photoelectron will propagate away from the absorbing atom with wave number k:

$$k = \frac{\sqrt{2m\,(E - E_{BE})}}{\hbar} = 0.512\,(E - E_{BE})^{1/2}, \tag{2.15}$$

where m is the mass of an electron and E is the photon energy of the incident X-ray photon. This wave number of emitted photoelectron depends on the photon energy of the incident X-ray photon. The outgoing photoelectron wave can be scattered by the neighboring scattering atoms and interact with the backscattered photoelectron wave. This leads to constructive or destructive interference, which depends on the type, the number, and the distance of the scattering atoms, resulting above an absorption edge in EXAFS spectra as shown in **Figure 2.15b**[180] A schematic drawing of the scattering process is shown in **Figure 2.18.**

EXAFS can be modelled using the following equation.[181]

$$\chi(k) = \sum_{j} \frac{N_j f_j(k)\, e^{-2\,\sigma_j^2 k^2}}{K R_j^2} sin\big[2kR_j + \delta_j(k)\big] \tag{2.16}$$

where $f_j(k)$ and $\delta_j(k)$ are photo-electron scattering properties of the neighboring atom.

The EXAFS oscillation amplitude is proportional to the number of neighboring scattering atoms. The frequency of the EXAFS oscillation is inversely proportional to the distance between absorbing atom to the scattering atom, and type of the scattering atom is revealed by the shape of the EXAFS oscillation. Therefore, from EXAFS, the distance from the scattering atom to the absorber (R), the number of scattering atoms or the coordination number (N), the root

mean-square of disorder of neighbor distance (σ^2) and the identities of scattering atoms can be obtained. The EXAFS data analysis can be done with EXAFS program packages to obtain the structural parameters. In this PhD thesis the EXCURVE77 software was utilized.
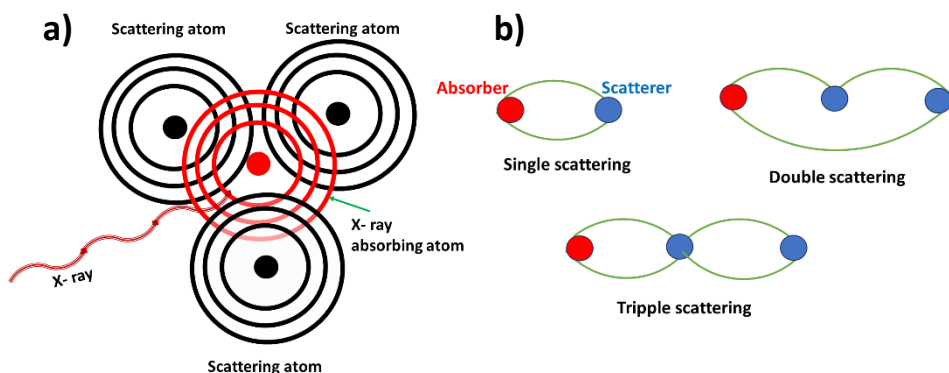
Figure 2.18. a) Schematic drawing of a scattering between absorbing atom and scattering atoms b) types of scattering

2.8. Photocatalytic degradation of stearic acid ($C_{18}H_{36}O_2$)

The photocatalytic degradation of stearic acid (SA) in which the decomposition of a thin layer of SA, deposited onto a film and exposed to light, is monitored as a function of time.[182,183,184,185] It is a popular and widely accepted approach to evaluate the self-cleaning activity of photocatalytic films. SA is preferred molecule for this test because it is representative for a group of organic fouling compounds that contaminate glass surfaces.[182,186,187] This approach has gained preference over the years for a number of other reasons, including: (a) SA is a reasonable model compound for solid films deposited on exterior and interior surfaces, (b) SA is very stable under UV illumination in the absence of a photocatalyst film, and (c) the kinetics of SA removal on dense thin films are usually simple and of zero-order, and so the SA film thickness is not a critical factor when assessing the photocatalytic activity, making the test much easier. A zero-order reaction is a type of chemical reaction where the rate of reaction is independent of the concentration of the reactant(s). This means that

the rate of reaction remains constant over time, as long as there is some reactant present.[188] The typical reaction involved in this SA test is described by the following reaction with TiO_2 as a semiconductor:[184,186,189]

$$CH_3(CH_2)_{16}CO_2H + 26\ O_2 \xrightarrow[h\upsilon \geq E_{bg}]{TiO_2} 18\ CO_2 + 18\ H_2O \qquad (2.17)$$
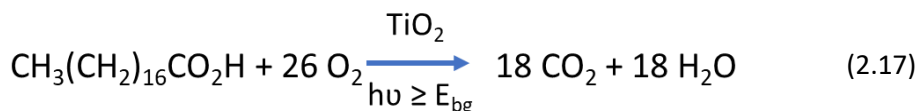
This reaction can proceed only in the presence of both oxygen and light with a photon energy that is larger than the TiO_2 anatase band gap, i.e. >3.2 eV. The degradation of SA can be the result of a direct reaction with photogenerated electrons/holes and/or photooxidation via the formation of highly reactive oxidant species (**equations 1.1 to 1.6 of chapter 1**). These latter are products of a reaction involving the adsorption of species (H_2O and O_2) on the TiO_2 surface.[187] The most commonly employed method to follow the SA photodegradation (**reaction 2.17**) uses infrared absorption spectroscopy. SA absorbs strongly in the 2700–3000 cm^{-1} region, particularly at 2958 cm^{-1}, 2923 cm^{-1}, and 2853 cm^{-1}, frequencies that are corresponding to asymmetric in-plane C–H stretching in the CH_3 group and asymmetric and symmetric C–H stretching in the CH_2 groups, respectively.[184] The absorption at those frequencies decreases together with the photocatalytic degradation of SA.
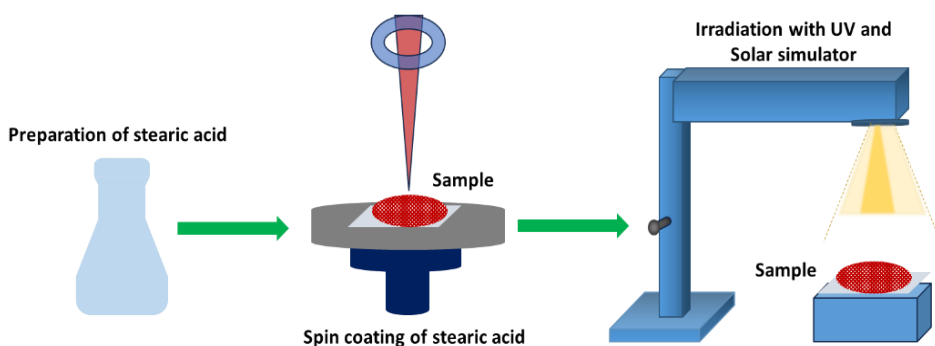
Figure 2.19. Schematic illustration of procedure of SA degradation test.

The experimental procedure is schematically provided in **Figure 2.19**. 100 µL of a 0.13 wt % SA (Sigma-Aldrich, ≥ 99.5%) in chloroform solution was spin-coated (1000 rpm, 1 min) at the samples and subsequently dried in an oven

at 80°C for 15 min. The photocatalytic activity tests were performed at ambient conditions under UV and AM (Air Mass) 1.5G simulated sunlight irradiation. The used UV light source is a fluorescent S 25 W UVA lamp (Philips) with a spectral range from 300 nm to 450 nm and a fluence of 2.6 mW cm^{-2}. The solar simulator (SciSun-300, Sciencetech) has the intensity of 100 mW cm^{-2} between 300 nm and 1100 nm as measured with a calibrated spectroradiometer (Avantes Avaspec-3648-USB2). The SA degradation upon illumination was measured by recording the absorbance with a Fourier transform infrared (FTIR) spectrometer (Nicolet^{TM} 380, Thermo Fisher Scientific), while the sample was placed under a fixed angle of 9° with the infrared beam to avoid internal reflection. The quantity of SA remaining on the sample surface was determined by integrating the spectral range from 2800 to 3000 cm^{-1} and plotting versus illumination time. Examples are shown in **Figures 2.20a and b.**
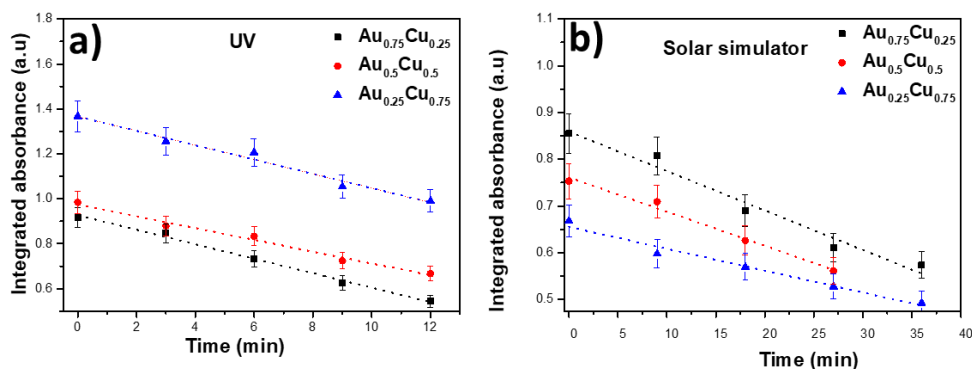
Figure 2.20 a) Evolution of integrated FTIR absorbance of stearic acid between 2800 to 3000 cm^{-1} as a function of illumination time on the AuCu clusters modified TiO$_2$ under UV and solar simulator illumination.

The self-cleaning nature of as-prepared samples, Au$_x$Cu$_{1-x}$ (x = 1, 0.75, 0.50, 0.25 and 0) is examined by monitoring the degradation of SA from their surface. The linear decrease in the concentration of reactant with time indicates that SA degradation is a zero-order reaction whose rate is independent of the initial concentration of SA.[190]

2.9. Photoelectrochemical work station

Photoelectrochemical (PEC) processes were already introduced in section 1.3. Here the components of the PEC cell used in this thesis are discussed.

A schematic diagram of PEC cell is given in **Figure 2.21**. The PEC cell consists of three electrodes: photoanode (working electrode (WE) - TNTs), cathode (counter electrode (CE) - Pt) and reference electrode (RE - Ag/AgCl). Both photoanode and cathode electrodes are crucial for initiating PEC reactions. In this three-electrode electrochemical setup,[191] the WE is the sample of interest where the first half-reaction, such as water oxidation, occurs (as illustrated in **Figure 2.21**). The CE provides the site for the second half-reaction of water splitting. This electrode should have a large surface area and exhibit fast kinetics to avoid limiting the circuit current. The RE ensures that the potential of the working electrode is applied and measured relative to a well-defined electrochemical potential scale. Commonly used REs include saturated calomel electrodes (SCEs) and Ag/AgCl electrodes.[3] Another important component is the electrolyte which is in contact with both photoanode and cathode and which works as a medium for the ions to flow between photoanode and cathode, thereby closing the electric circuit.

When the photoanode absorbs UV light, it generates electron-hole pairs; electrons in the conduction band and holes in the valence band. The generated electrons are utilized in the electrocatalytic half-reaction of water reduction to produce hydrogen gas (H_2), while the generated holes are utilized in the electrocatalytic half-reaction of water oxidation to produce oxygen gas (O_2).[193] There is an external circuit that connects the photoanode and cathode allowing the flow of generated electrons from the photoanode to the cathode where the reduction reactions take place and photogenerated holes are consumed by the oxidation reactions at the photoanode.[8]

---

[3] In publications on PEC water splitting, the applied potential, initially measured with respect to an SCE or Ag/AgCl reference electrode, is often converted to the reversible hydrogen electrode (RHE) scale using **equation (4.1).**[192]

51

Evaluating the performance of a PEC cell involves various analytical techniques to measure its efficiency, stability, and other key parameters. Some commonly used techniques are linear Sweep Voltammetry (LSV), Chronoamperometry (CA), and Electrochemical Impedance Spectroscopy (EIS).
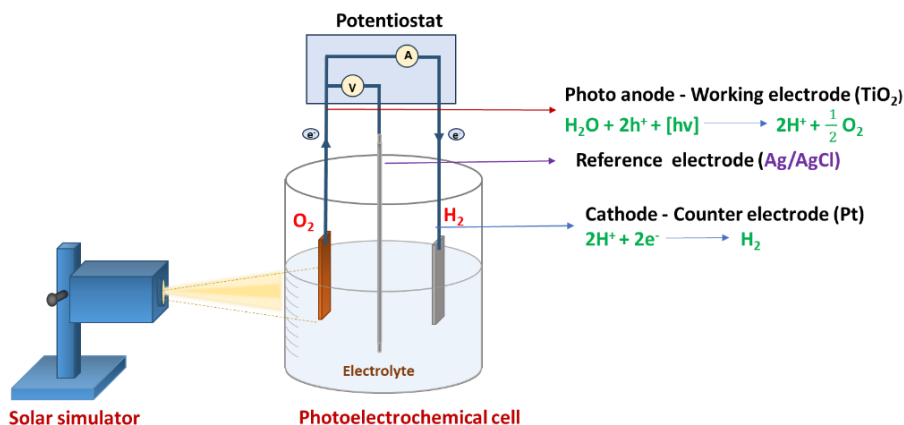
Figure 2.21. Schematic representation of a photoelectrochemical cell that is used for the water-splitting: evolution of oxygen at the photoanode and evolution of hydrogen at the cathode.

2.9.1. Linear Sweep Voltammetry

LSV is an electrochemical technique where the current at a working electrode is measured, while the potential between the working electrode and a reference electrode is linearly swept from an initial to a final value.[194] The resulting current response is recorded and plotted against the applied potential, producing a voltammogram. This technique is particularly useful in photochemistry for several reasons: [195]

- LSV can measure the photocurrent generated by a photoelectrode when illuminated by light. Comparing a curve of current density vs. applied potential with and without light illumination provides valuable insights about the photoactivity of the material.
- Important parameters such as the onset potential and maximum photocurrent can be derived from LSV curves. The onset potential is the

potential at which the photocurrent begins to rise significantly, indicating the energy level at which the photoelectrode starts driving redox reactions effectively. A low onset potential is desirable as it means the material can operate efficiently at low applied voltages.

- The shape and slope of the LSV curve provides information about the kinetics of charge transfer at the photoelectrode-electrolyte interface. A steep rise in the current indicates efficient charge separation and fast kinetics,[196] essential for high-performance PEC systems.

- LSV is an effective method for comparing different photoelectrode materials under identical conditions. By examining the photocurrent response and onset potentials of various materials, researchers can identify which materials offer the best performance for applications such as water splitting or CO_2 reduction.

- In PEC cells, catalysts are often used to enhance the efficiency of redox reactions. LSV curves help evaluate catalytic activity by comparing photocurrent responses with and without the catalyst. An increase in photocurrent in the presence of a catalyst indicates its effectiveness in promoting the desired reactions. Examples of LSV curves are given in **Figure 2.22.**
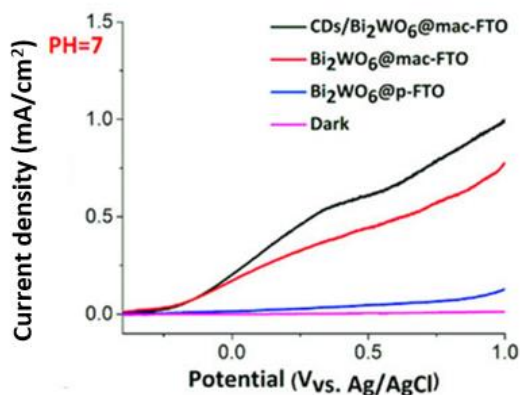
Figure 2.22. Linear sweep voltammetry (LSV) curves of the Bi2WO6@p-FTO photoelectrode, Bi2WO6@mac-FTO photoelectrode and CDs/Bi2WO6@mac-FTO photoelectrode, adapted from ref. [197]

2.9.2. Chronoamperometry

CA is an electrochemical technique that measures the current as a function of (an extended) time at a fixed potential. A constant potential is applied to the working electrode and the current is recorded as a function of time, which provides information about the kinetics of electrochemical processes. [198,199] An example of CA is given in **Figure 2.23.**
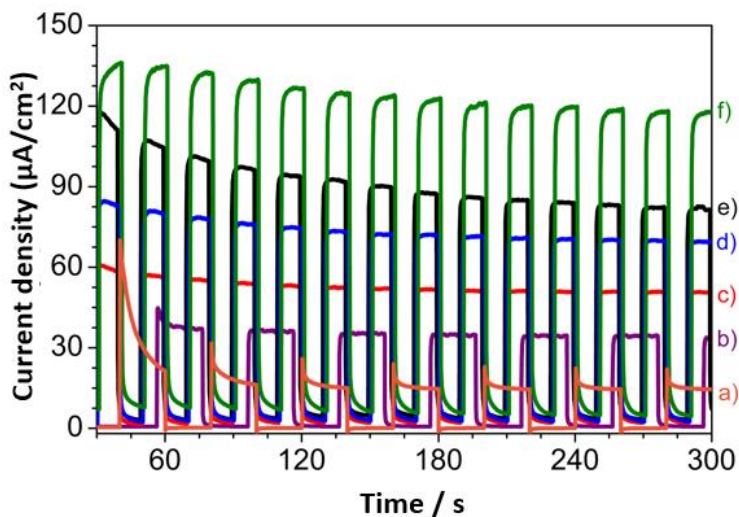
Figure 2.23. Chronoamperometry curves recorded at 0.5 V *vs*. Ag/AgCl (0.1 M KCl) under intermittent illumination (100 mW·cm^{-2}, AM1.5) in 0.5 M K$_2$SO$_4$ for different electrodes: a) Ti/BiVO$_4$, b) Ti/TiO$_2$, c) Ti/TiO$_2$/BiVO$_4$, *d*) Ti/TiO$_2$/BiVO$_4$/Au, e) Ti/TiO$_2$/Au/BiVO$_4$ and f) Ti/TiO$_2$/Au/BiVO$_4$/Au. Figure is adapted from ref. [200].

- CA is essential for evaluating the long-term stability and durability of photoelectrodes. By applying a constant potential and measuring the photocurrent over time, degradation of photoelectrode can be monitored, which is critical for practical PEC water splitting devices. Specifically, CA can identify photocorrosion, indicated by a decline in photocurrent over time, showing material degradation under operational conditions.[191]

- CA captures the transient behavior of the photocurrent, allowing analysis of the charge carrier dynamics. The initial spike in current followed by a decay can reveal details about recombination processes and the efficiency of charge separation within the photoelectrode.

- CA offers a quantitative measure of the photocurrent under controlled conditions, crucial for comparing the performance of different photoelectrodes. This data aids in optimizing the design and fabrication processes of PEC systems.

2.9.3. Electrochemical impedance spectroscopy

EIS is a frequency sweep technique used to measure the impedance of an electrochemical cell over a broad frequency range usually between 0.1 Hz to 100 kHz.[201] There are two ways to visualize electrochemical impedance spectroscopy measurements. One is a Bode plot, which will show the impedance at different frequencies. The other is a Nyquist plot, which compares the real and imaginary parts of electrochemical impedance.[202] They provide complementary information about the performance and efficiency of the PEC cell.

- **Bode plot:** It displays the frequency response of a system via the phase shift between the input and output signals as a function of frequency. Peaks in the plot help to identify different time constants of the system, which are related to processes such as charge transfer, recombination and diffusion. The maximum phase shift can be associated with the frequency range where the interplay between double-layer capacitance and charge transfer resistance is most pronounced. This typically occurs in the mid-frequency range.

- **Nyquist plot:** It is constructed by plotting the negative imaginary part of the impedance versus the real part of the impedance, either for individual electrodes or for the electrochemical cell as a whole. The real part of the impedance contains information about the resistances, while the imaginary part tells us about the capacitance of the electrode. The plot typically shows a semicircular arc, with each point on the arc representing the impedance at different frequencies. The diameter of the semicircle is related to the charge transfer resistance (R_{ct}) at the

electrode/electrolyte interface, indicating how efficiently charge is transferred.[203] Examples of bode plot and Nyquist plots are given in **Figures 2.24.**
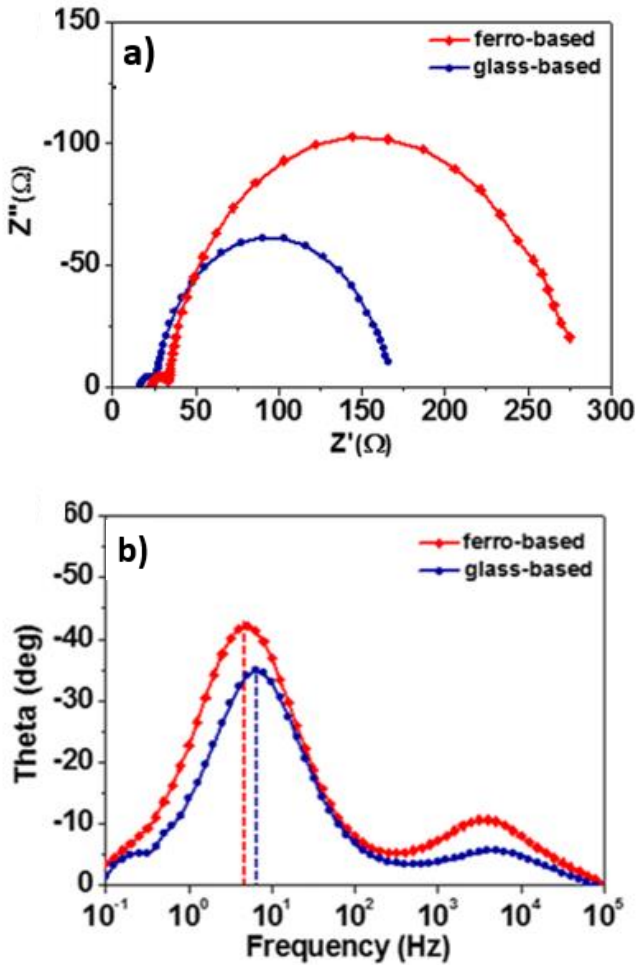
Figure 2.24. (**a**) Nyquist plot and (**b**) Bode plot of ferro-based and glass-based cells, adapted from ref. [204].

Chapter 3

Composition-tuned well-defined gold-silver clusters-modified TiO₂ film as efficient self-cleaning surfaces under visible light

This chapter is based on the following publication:

Author contributions

Chapter 3 – AuAg on TiO$_2$ as an efficient self-cleaning photocatalyst

3.1 Introduction

Titanium dioxide (TiO$_2$) has been intensely investigated as a photocatalyst for the decomposition of many organic compounds[15,19,26] due to its very good photocatalytic self-cleaning activity, chemical and thermal stability, large scale production, and low cost.[10,11,12,205] Redox reactions are initiated at the TiO$_2$ surface with photogenerated electron-hole pairs. One of its important applications is in self-cleaning surfaces widely adopted on tiles, tent fabric,[186] or glasses[206] where the surfaces covered by a thin film of TiO$_2$ decompose the pollutants under UV light irradiation. The residues are photo-mineralized and/or subsequently washed off by rainwater.[207,208] TiO$_2$ self-cleaning activity is conveniently assessed by monitoring the photocatalytic destruction of stearic acid (SA), a model compound for the class of organic contaminants typically found on fouled glass surfaces.[186,190,187] The main limitations of the current self-cleaning materials lie in their modest solar-light response due to the large band gap of TiO$_2$ (3.2 eV for anatase) that requires UV irradiation making up only *ca.* 4% of the solar spectrum,[209] and their low quantum yield (fast recombination of charge carriers). Modifying TiO$_2$ surface with NPs of plasmonic metals such as Au, Ag and their bimetallic combinations that are capable of absorbing visible light accounting for *ca.* 42% of the solar irradiation via their (localized) surface plasmon resonance (L)SPR[71,210,211] is being investigated extensively.[212] The plasmonic collective oscillation of the metal nanoparticle conduction electrons generates energetic hot electrons and holes[213,214,215] that can potentially induce and/or accelerate chemical reactions at the surface of the nanoparticle,[213,216,217,218] but with strong limitations due to their rapid recombination. These hot charge carriers can more efficiently directly generate an electron in the strongly coupled TiO$_2$ semiconductor acceptor through a plasmon-induced metal to semiconductor interfacial charge-transfer transition with a quantum yield for electron injection exceeding 24% independently of the incident photon energy.[218,219] Recent work also points out the major role played by plasmonic hot holes mainly concentrated near the gold–semiconductor interface, which is further identified as the reaction site for plasmonic water oxidation.[215] Finally, beside direct charge transfers, the near-field effect originating from SPR induces strong electric fields of orders of magnitude higher than the incident field, close to the plasmonic nanoparticle's surface.[61,220]

The (L)SPR absorption band of the NPs deposited on TiO$_2$ can be further tuned and extended over the entire visible light range to maximize the overlap

with the incident light spectrum by mixing two plasmonic metals with tailored compositions. This generally results in significant improvements in the photocatalytic performance,[221,222] particularly with respect to the activity and selectivity as compared to their monometallic counterparts.[107] Additionally, BNPs deposited on TiO$_2$ are expected to display not only the combination of the chemical properties associated with two individual metals, but also new properties due to synergy between two metals. The effects of the structure of plasmonic hybrids in different photocatalytic applications are detailed in a recent review by Ninakanti et al.[223]

Colloidal Au-Ag alloy NPs display highly tunable, composition-dependent LSPR maxima over a broad visible light range (*ca.* 420–520 nm).[224,225,226] In that context, plasmonic 'rainbow' nanoparticles (gold-silver composite nanoparticles of various sizes and compositions) supported on TiO$_2$ P25[4] and coated by a protecting layer exhibited a 56% increase in efficiency compared to pristine P25 combined with a good stability under simulated solar light.[227] This corroborates numerous studies highlighting the higher visible light photoactivity of bimetallic Au-Ag/TiO$_2$ nanocomposites compared to their monometallic Ag/TiO$_2$ and Au/TiO$_2$ counterparts.[228,229] This demonstrates that Au-Ag NPs are appropriate candidates for harvesting a large portion of the solar spectrum, in view of outdoor photocatalytic applications.[230] Although wet-chemical synthesis of Au, Ag or bimetallic plasmonic nanostructures is at the origin of significant enhancements in visible light photoactivity of self-cleaning TiO$_2$-based surfaces,[231] these colloidal techniques that generally involve large volumes of solvents (waste) as well as hazardous chemical agents, do not allow a strict control over the particle size and composition. The resulting polydispersed nature of these alloy nanomaterials hampers further investigation of their detailed structural and electronic properties as well as of bimetallic synergistic effects, mainly due to the lack of reliable information at the atomic scale.

Well-defined plasmonic nanostructures can be fabricated in an efficient and sustainable way by using the gas-phase cluster beam deposition (CBD) technique that allows for a precise control over cluster size and composition, and does not require the use of solvents.[232] The physical aspects of size

---

[4] P25 is a frequently used commercial titania material containing crystalline phases of higher anatase and lower rutile ratio.

controlled cluster production with laser ablation sources developed almost four decades ago[233] have been described in detail in the literature.[234,148] Our laser ablation cluster setup is equipped with a reflectron time of flight mass spectrometer (RToF-MS) that analyses in line the mass distribution of the produced clusters in the gas phase allowing an excellent control of their size distribution by fine-tuning the cluster formation conditions including the helium gas pressure, the temperature of the source block and the nozzle, as well as the ablation laser power and timing (careful timing of the laser pulse relative to the carrier gas pulses is instrumental for cluster production).[156] It was already demonstrated that TiO$_2$ P25 modified by Au clusters deposited by CBD has a remarkable four-fold increase in its photocatalytic efficiency under 515 nm green light compared to its pristine counterpart.[235]

We have fully exploited the possibilities of the CBD method to prepare high performance solar light photocatalysts by decorating TiO$_2$ with soft-landed Au-Ag clusters of uniform size and compositions precisely tuned over their miscibility range. These photocatalysts show a remarkable increase in their photocatalytic efficiency along with a clear experimental correlation between the cluster composition and the spectral output of the light source. Electromagnetic light-matter simulations in combination with detailed characterization of these well-defined photocatalysts bring more insight into the main mechanisms responsible for the composition-dependent enhancement of their activity. This demonstrates not only the added value of controlling the composition of metal clusters to tune and enhance plasmonic photocatalytic effects, but also the excellent potential of the CBD technology to fabricate efficient noble metal modified photocatalytic surfaces.

3.2. Sample preparation and methods

This section describes the preparation of titania substrates (TiO$_2$ P25 powder coated SiO$_2$ surfaces) and their surface modification with AuAg NCs. Additionally, the experimental methods employed in this study are presented within this section.

3.2.1. Preparation of AuAg nanoclusters modified samples

Precleaned Si wafers (3 × 1.5 cm²) were spin-coated for 1 min at 1500 rpm with 150 µL of a 1 wt.% TiO$_2$ P25 (ACROS Organics, ≥ 99.5%, ~ 80% anatase, ~ 20% rutile) in ethanol suspension to get a thin layer of titania. The P25 suspension was made in a sealed glass vial and ultrasonicated for 30 min to

homogenize the suspension. Afterwards, the samples were dried at 105˚ C overnight. Next, the prepared TiO$_2$ P25 samples were modified with AuAg NCs with equivalent atomic coverages of 2 ML, 4 ML, 6ML, and 8 ML using laser ablation cluster course (Cluster Deposition Apparatus - CDA). Chapter 2, section 2.1 offers a detailed account of the laser ablation setup and its operation, as well as the process of cluster production.

3.2.2. Sample characterization

The size and shape of the deposited clusters on TEM grid (ultrathin carbon film on lacey carbon support film, 400 mesh, copper, purchased from TED Pella, INC) was determined using a probe-lens aberration corrected scanning transmission electron microscope (STEM) (Jeol, ARM200F instrument) for two samples (pure gold clusters and Au$_{0.7}$Ag$_{0.3}$ alloy clusters) measured at an accelerating voltage of 200 kV and a magnification of 200,000. The cluster size distribution was obtained using image analysis software. Ex situ Scanning Electron Microscopy (SEM) was used to acquire the sample images at an accelerating voltage of 10 kV, and an aperture size of 30 µm using an electron beam lithography and microscopy platform (Raith GmbH). Ultraviolet-Visible light absorbance spectra (UV-Vis) of cluster decorated P25 samples were obtained in the 300-700 nm wavelength range using a double beam UV 2600 spectrophotometer (Shimadzu, Kyoto, Japan) equipped with film holders attached to a BaSO$_4$ coated integrating sphere of 60 mm in diameter. A pristine TiO$_2$ sample was used as the background. X-Ray Photoelectron Spectroscopy (XPS) measurements were performed at room temperature using a laboratory setup equipped with a Mg Kα X-ray (XR4 Twin Anode X-ray source, non-monochromatic) and an Alpha 110 hemispherical analyzer and the spectra were acquired in Ultra High Vacuum (UHV) (base pressure $\sim 10^{-8}$ mbar) with an energy step of 0.2 eV and energy resolution of ≈ 1 eV, and a beam diameter of 5 mm.

XAFS data were collected at the Au L$_3$-edge (E = 11919 eV) in grazing incidence (incidence angle ~ 2° with the beam polarization perpendicular to the surface) in fluorescence detection mode at the LISA beamline (BM08)[236] at The European Synchrotron (ESRF, Grenoble, France) operating in a 7/8 multi bunch mode with a current of 200 mA. The monochromator was equipped with a pair of flat Si (111) crystals and was cooled at liquid nitrogen temperature. The harmonic rejection was carried out by using a pair of Si mirrors. The samples were measured in ambient conditions up to a k = 12 Å^{-1} wave number with

typical acquisition times of 40 min (i.e. 6–12 s per data point). The incoming beam was measured via a nitrogen filled ion chamber, the fluorescence signal from the Au L$_\alpha$ line was collected by a 12 elements High Purity Germanium detector. Two spectra were generally averaged to improve the signal to noise ratio. Data reduction of the experimental X-ray absorption spectra was performed with the program EXBROOK. Background subtraction and normalization were carried out by fitting (i) a linear polynomial to the pre-edge region in order to remove any instrumental background and (ii) cubic splines simulating the absorption coefficient from an isolated atom to the post-edge region. EXAFS refinements were performed with the EXCURVE package. Phase shifts and backscattering factors were calculated ab initio using Hedin-Lundqvist potentials. The data were fitted both in k^2 and k^3 spaces. Possible asymmetric oscillation effects in the interatomic radial distribution were fully accounted for in the refinements.

3.2.3. Photocatalysis towards stearic acid degradation

100 µL of a 0.13 wt% SA (Sigma-Aldrich, ≥ 99.5%) in chloroform solution was spin-coated on the wafers (1000 rpm, 1 min) and subsequently dried in an oven at 80 °C for 15 min. The photocatalytic activity tests were performed at ambient conditions under UV and AM (Air Mass) 1.5G simulated sunlight irradiation. In Chapter 2, section 2.8 provides an elaborate explanation of the procedure involved in measuring the samples.

3.3 Results

3.3.1. Structural characterization of Au-Ag clusters

The gas-phase size distribution of Au$_x$Ag$_{1-x}$ clusters with x = 0, 0.1, 0.3, 0.5, 0.7, 0.9 and 1, produced by ablating alloy targets and inert gas condensation in a dual target laser ablation source, is recorded using *in situ* time of flight mass spectrometry (ToF-MS). Prior to cluster deposition, the gas phase size distribution of charged clusters of all the compositions peaks around 2 nm assuming a spherical shape (**Figure 3.1**) and the cluster flux is measured prior and after cluster deposition using a quartz crystal microbalance (QCM). Based on the cluster flux, the deposition time is set to correspond to the required amount of clusters, which are expressed in an equivalent number of atomic monolayers (ML, i.e. a thickness equivalent to a film of 0.25 nm). Most depositions had an amount equal to 4 ML equivalents, but also 2 ML, 6 ML, and

8 ML were prepared. Taking into consideration the average cluster diameter and random deposition, the 4 ML loading corresponds to a ca. 59% coverage of the surface with clusters.
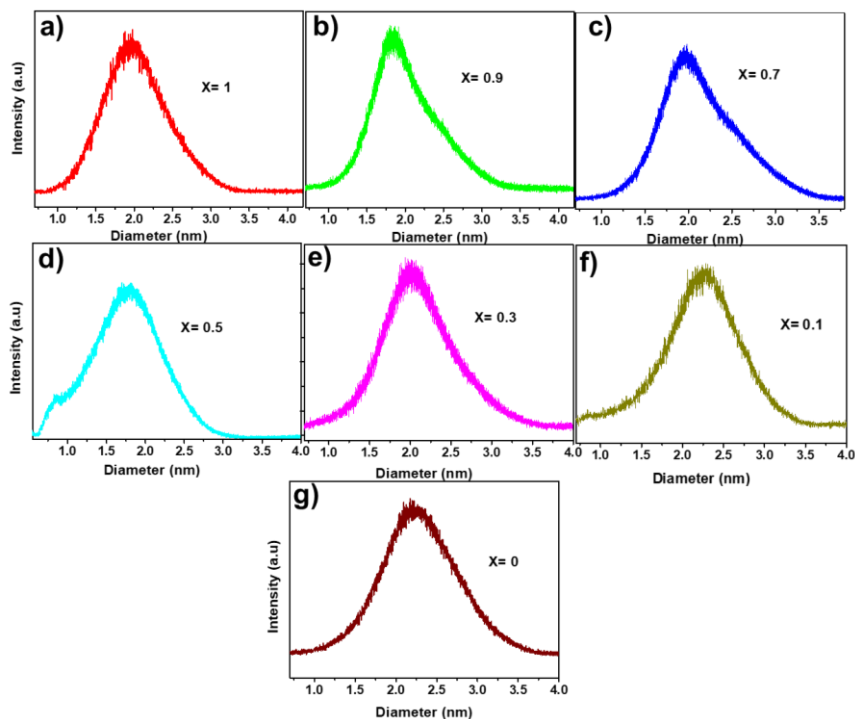
Figure 3.1. Size distribution of Au_xAg_{1-x} (x = 1, 0.9, 0.7, 0.5, 0.3, 0.1 and 0) bimetallic clusters as measured by time-of-flight mass spectrometry prior to cluster deposition. The cluster diameter is deduced from the measured mass assuming a spherical shape and bulk density.

STEM images of $Au_{0.7}Ag_{0.3}$ and Au clusters, deposited on lacey carbon TEM grids at a loading of 0.26 ML and 0.63 ML, respectively, and their corresponding size distributions were obtained by image analysis, leading to mean diameters of the spherical clusters of 3 nm and 3.5 nm for the $Au_{0.7}Ag_{0.3}$ and Au clusters, respectively (**Figure 3.2**). The slightly larger size distribution observed with STEM compared to the mean diameters obtained in the gas phase may be attributed to a less efficient detection of the larger mass clusters

by the microchannel plate (MCP) of the ToF-MS particularly under the conditions of relatively low acceleration voltages [237, 238] (in our case it is < 3 kV). Additional flattening of the clusters due to cluster-support interaction after deposition combined with a limited cluster agglomeration on the support may also contribute to this effect. The clusters are uniformly distributed over the surface and are crystalline, forming the common icosahedral structure as illustrated by the insets in **Figure 3.2a and 3.2b** which is consistent with the literature for gold clusters with sizes below 5 nm.[239] Computational methods predict the shape and structure of face-centered cubic gold nanocrystals
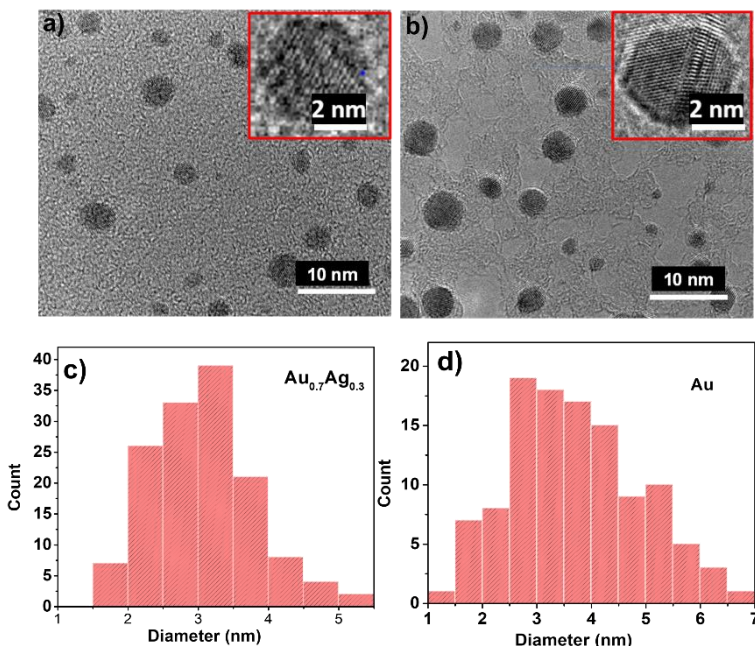
Figure 3.2. STEM images of (a) Au$_{0.7}$Ag$_{0.3}$ and (b) Au clusters on lacey carbon supports. The insets show a high-resolution images of a single cluster. Size distributions resulting from image analysis of the (c) Au$_{0.7}$Ag$_{0.3}$ and (d) Au cluster samples.

smaller than 3 nm [240] and provided a clear picture of the nanoparticles' size-structure relationship.[241] A detailed study of size-structure relationship is beyond the scope of this thesis.
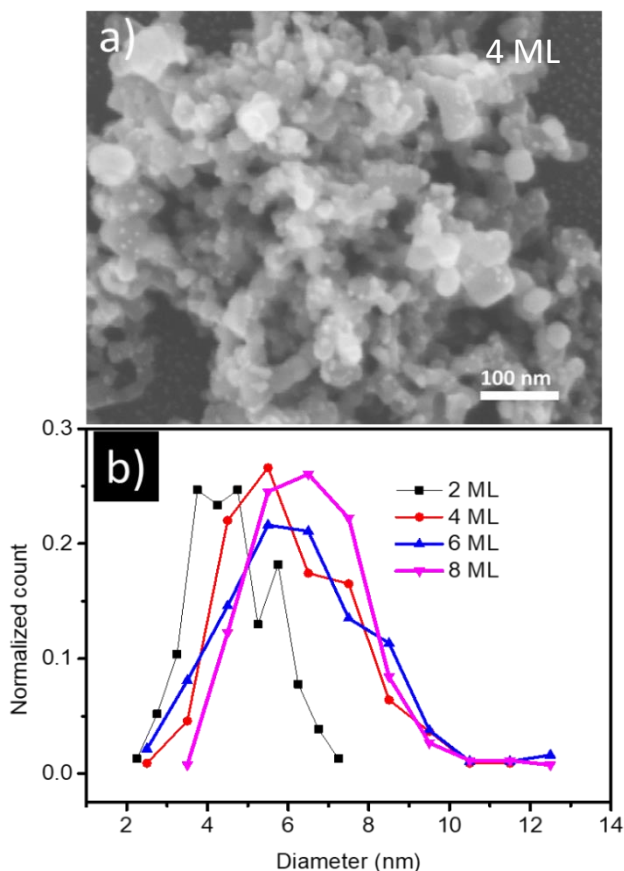
Figure 3.3 (a) SEM image of Au$_{0.3}$Ag$_{0.7}$ cluster-modified TiO$_2$ P25 (small white spots are clusters). (b) Size distribution of Au$_{0.3}$Ag$_{0.7}$ clusters for different loadings as obtained from analysis of SEM images. About 200 clusters are analyzed per image. The average sizes are 4.1 ± 0.2, 5.7 ± 0.2, 6.1 ± 0.1, and 6.4 ± 0.1 nm for the 2, 4, 6, and 8 ML samples, respectively.

A SEM image of a 4 ML Au$_{0.3}$Ag$_{0.7}$ cluster-modified titania surface (**Figure 3.3a**) shows that the TiO$_2$ covers the silicon substrate uniformly, though on a larger scale there are regions with more or less spin-coated material, which is typical for a powder coating. The bimetallic Au$_{0.3}$Ag$_{0.7}$ clusters are clearly present and show up as small white spots.

Corresponding cluster size distributions were obtained for different cluster loadings using image analysis software (**Figure 3.3b**). Although SEM provides information about the supported catalyst and explores cluster agglomeration with increasing coverage (**Figure 3.4**), its lower resolution (1.5 nm @ 10 keV) as compared to that of TEM results in a lower accuracy in the determination of the clusters diameters.
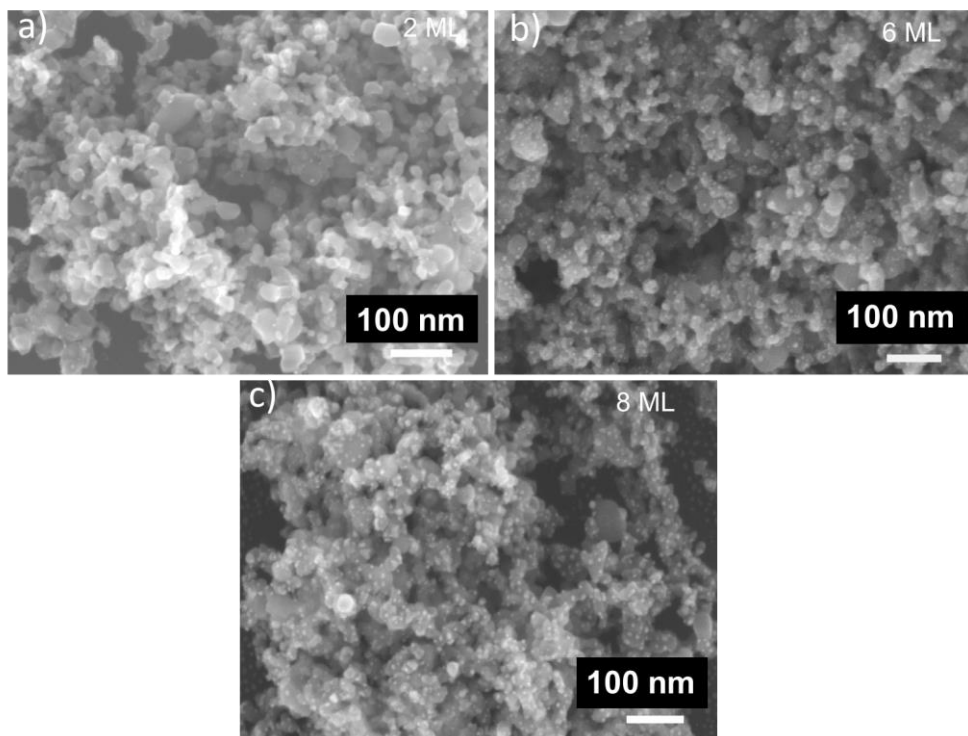
Figure 3.4. SEM images of Au$_{0.3}$Ag$_{0.7}$ clusters for different loading of 2 ML (a), 6 ML (b), and 8 ML (c). The apparent cluster sizes become larger with the increased loading, which indicates cluster coalescence.

At the highest coverage (8 ML) the Au$_{0.3}$Ag$_{0.7}$ clusters display a larger average size of 6.4 nm and more irregular shapes, suggesting a significant level of cluster coalescence. At a coverage of 6 ML the particles have an average diameter of 6.1 nm. A gradual increase in the size of the particles with an increase in loading from 2 ML to 8 ML is evident (**Figure 3.3b**). This indicates that the extent of cluster coalescence increases with the cluster coverage, resulting in larger and less regularly shaped particles. An additional drawback of

66

loadings above 4 ML is the reduced accessibility of active sites on the TiO$_2$ surface by the clusters, which may in turn result in a lower photocatalytic efficiency.[235]
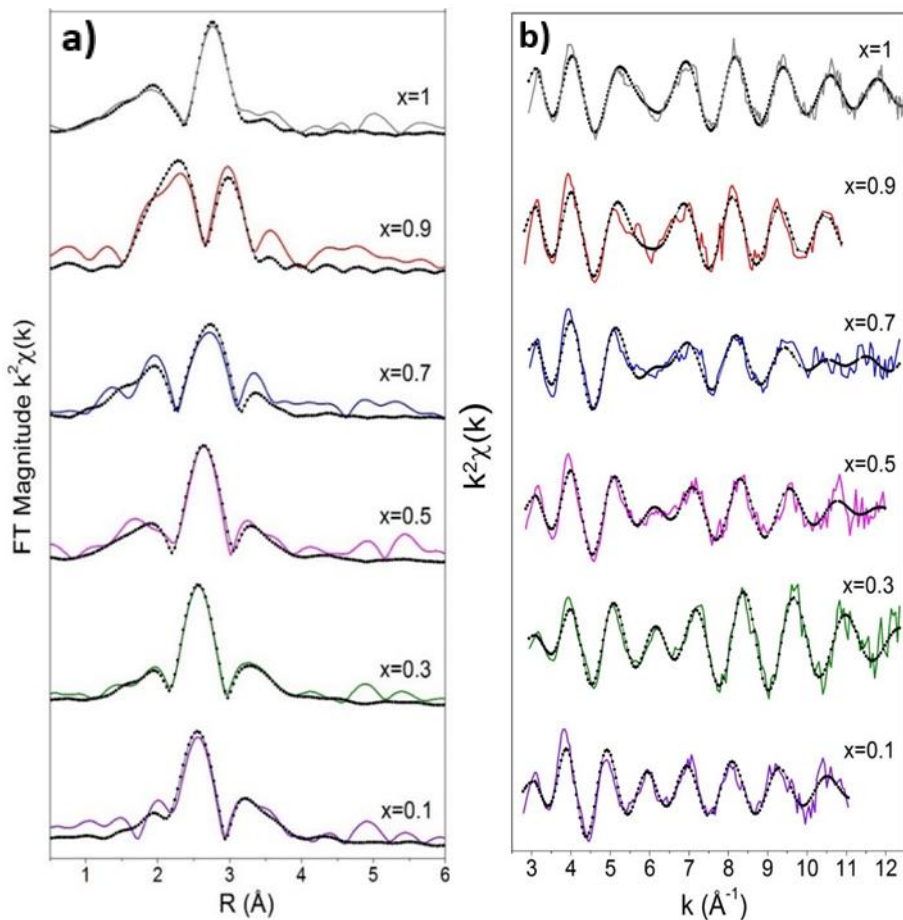
Figure 3.5. a) Phase-corrected Fourier-transformed Au L$_3$-edge XAFS spectra from gold rich to silver rich clusters along with pure Au clusters (x=1). b) k^2 weighted XAFS spectra of the Au$_x$Ag$_{1-x}$ bimetallic clusters on TiO$_2$ and carbon supports from x = 1 to 0.1, along with a spectrum from pure Au clusters, colour full line is the data and dashed black line is the fit.

The detailed atomic structure of the Au$_x$Ag$_{1-x}$ bimetallic clusters deposited on TiO$_2$ and carbon supports with a 4 ML loading was further characterized by X-ray absorption spectroscopy carried out at the Au L$_3$-edge. Extended X-ray Absorption Fine Structure (EXAFS) is element specific and does not need long-range order in the material. This allows for a precise detection of the alloyed structure in nanostructured Au-Ag bimetallic systems.[242,243]

As representative investigation of the entire surface of the materials, it offers complementary information to electron microscopy. Phase corrected Fourier Transforms (**Figure 3.5a**) of the k$_2$-weighted EXAFS spectra (**Figure 3.5b**) at the Au-L$_3$ edge show a doublet between 2 and 3 Å associated with a beat at 6 Å^{-1} in the EXAFS spectra that is characteristic of Au-Ag alloys.[243] Detailed fitting of the data was carried out with a 2-shell structure model based on Au-Au, and Au-Ag as no significant additional shells were present at higher distances. No Au-O interactions could be detected, indicating the fully metallic state of Au in the clusters. The fitting results of Au$_x$Ag$_{1-x}$ bimetallic clusters deposited on TiO$_2$ and carbon supports with a 4 ML loading are presented in **Table 3.1**. The amplitude reduction due to many-electron processes (AFAC) was set to 0.8. In each cluster, the relative N$_{Au-Au}$ and N$_{Au-Ag}$ coordination numbers showed an excellent agreement with the expected composition while the sum of the two N$_{Au-Au}$ and N$_{Au-Ag}$ contributions was almost identical and equal to *ca*. 11 for each bimetallic cluster sample. Assuming that Au-Ag bimetallic clusters adopt a cubooctahedral structure, this reduced coordination value N (due to the high fraction of atoms on the surface) is in agreement with the average size of 5.7 nm obtained by analysis of SEM images when using the tabulated values of N vs particle size.[244] The matching compositions **(Table 3.1)** indicate that silver and gold atoms are mostly forming metallic alloys with very limited amount of pure phases or oxides as previously reported.[242]

Although Au-Au atomic bond distances remain mostly constant over all compositions at 2.87 Å, **(Table 3.1)** which is only slightly shorter than the bulk value (2.88 Å), Au-Ag distances are sharply decreasing with increasing Au content from 2.86 Å in silver rich Au$_{0.1}$Ag$_{0.9}$ to 2.82 Å in gold rich Au$_{0.9}$Ag$_{0.1}$. In Au$_{0.5}$Ag$_{0.5}$ relatively short and identical Au-Au and Au-Ag distances of 2.85 Å are observed. These distance differences reflect the variety of local structures and electronic configurations in each composition and may also explain the composition-dependent structural arrangements observed in the same clusters deposited on SiO$_2$.[242] In Au$_{0.5}$Ag$_{0.5}$ the identical distances may favor the formation of an homogenous alloy over the whole bimetallic clusters while in

the other compositions different Au-Au and Au-Ag distances may be at the origin of the core-shell arrangements consisting of a gold rich and silver rich alloy with the minority element always at the core as previously reported.[242] This combined structural characterization is pointing out the remarkable homogeneity in terms of surface density, mean size and composition of the Au-Ag cluster samples obtained by the CBD technology. This will pave the way for the design of photocatalysts with tuneable properties.

Table 3.1. Summary of structural results of Au L$_3$-edge EXAFS refinements of the Au$_x$Ag$_{1-x}$ clusters.

Sample	Au$_{0.1}$Ag$_{0.9}$	Au$_{0.3}$Ag$_{0.7}$	Au$_{0.5}$Ag$_{0.5}$	Au$_{0.7}$Ag$_{0.3}$	Au$_{0.9}$Ag$_{0.1}$
Support	TiO$_2$	Carbon	Carbon	Carbon	TiO$_2$
E$_f$ (eV)	-8.6 (9)	-7.7 (6)	-7.7 (8)	-7.9 (8)	-8.2 (8)
AFAC	0.8	0.8	0.8	0.8	0.8
k-range (A$^{\circ-1}$)	2.8-11	2.8-11.5	2.8-11.5	2.8-11.5	2.8-10
N$_{Ag}$	10.0 (9)	8.3 (6)	5.6 (8)	3.0 (5)	1.0 (2)
R$_{Ag}$ (A$^{\circ}$)	2.86 (3)	2.85 (1)	2.85 (2)	2.84 (3)	2.82 (5)
A$_{Ag}$ (Å^2)	0.027 (3)	0.021 (2)	0.021 (4)	0.017 (4)	0.03 (4)
N$_{Au}$	1.0 (3)	2.9 (4)	5.5 (8)	8.0 (9)	10.0 (9)
R$_{Au}$ (A$^{\circ}$)	2.87 (9)	2.86 (1)	2.85 (2)	2.87 (1)	2.87 (1)
A$_{Au}$ (Å^2)	0.02 (1)	0.015 (2)	0.016 (4)	0.018 (3)	0.019 (3)
N$_{Ag}$+ N$_{Au}$	11	11.2	11.1	11	11
Diameter (nm)	~5	~5	~5	~5	~5
N$_{Au}$/ N$_{Ag}$+ N$_{Au}$	0.09	0.26	0.50	0.72	0.91
R (%)	42%	34%	45%	46%	41%

E_f = contribution of the wave vector of the zero photoelectron relative to origin of k

AFAC (amplitude reduction due to many-electron processes) was set to 0.8.

k= photoelectron wavenumber

N = number of atoms in each shell

R = distance between neighboring atoms in each shell

A = Debye-Waller term of each shell (A=2σ^2 with σ = Debye-Waller factor)

R(%) = percentage fit- Agreement fraction.

3.3.2. Electronic characterization

Insight in the electronic properties of the Au-Ag clusters was obtained by combining X-ray photoemission (XPS) and absorption spectroscopies (XANES). XPS was used to study the Au-Ag clusters interaction with the TiO$_2$ support, as well as the charge transfer occurring between Au, Ag and the support by monitoring the core level binding energy (BE) shifts of the different elements. The survey spectra **(Figure 3.6)** confirm the exclusive presence of Si, O, C, Ti, Au and Ag in all samples. The presence of gold and silver on the surface is verified by the dominant peaks of Au 4f and Ag 3d. Bulk Ag 3d (Ag 3d$_{5/2}$ at 368 eV and Ag 3d$_{3/2}$ at 374 eV)[245] and Au 4f states (Au 4f$_{7/2}$ at 84 eV and Au 4f$_{5/2}$ at 87.7 eV) are split due to spin-orbit coupling. The observed energy shifts in the Au$_x$Ag$_{1-x}$ (X = 0.9, 0.7, 0.5, 0.3 and 0.1) clusters on TiO$_2$ are consistent with those reported for Au-Ag alloyed nanoparticles.[246]
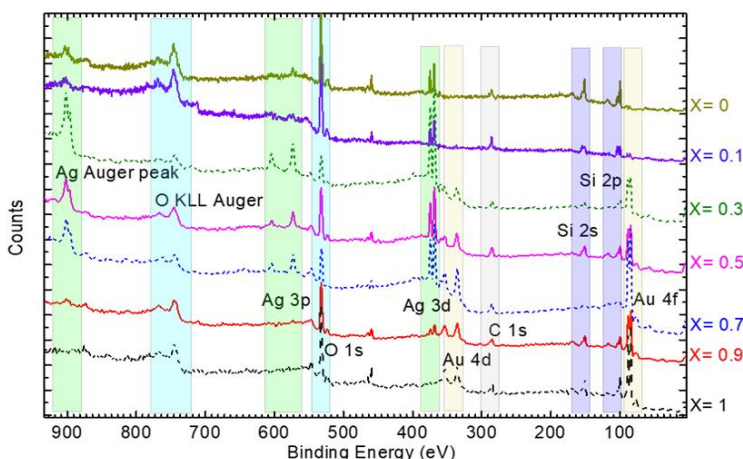
Figure 3.6. XPS survey spectra obtained for Au$_x$Ag$_{1-x}$ (x = 1, 0.9, 0.7, 0.5, 0.3, 0.1, and 0) clusters on TiO$_2$.

Analysis of the BE peak positions of Au 4f$_{5/2}$, Au 4f$_{7/2}$, Ag 3d$_{3/2}$ and Ag 3d$_{5/2}$ as a function of composition shows that the Ag 3d BE in all Au$_x$Ag$_{1-x}$ clusters is smaller than that of pure Ag clusters, but slightly higher than that of bulk silver 3d (368 eV and 374 eV). This is again in very good agreement with the values reported in the literature.[247,248] **Figure 3.7** presents the variation of the O 1s, Ag 3d and Au 4f core level XPS spectra of the Au$_x$Ag$_{1-x}$ bimetallic clusters on TiO$_2$ supported silicon wafers as a function of the Au fraction x. The deconvolution peaks of oxygen species O 1s located at a BE around 530 eV come from O^{2-} ions

in the TiO$_2$ and O$^-$ and O^{2-} ions in the oxygen vacancies induced defect regions, which mainly contribute to the photocatalytic reaction.[249,250] Peaks appearing at a BE value of 533 eV correspond to SiO$_2$, while the ones at 531 eV are associated with C-O bonds.
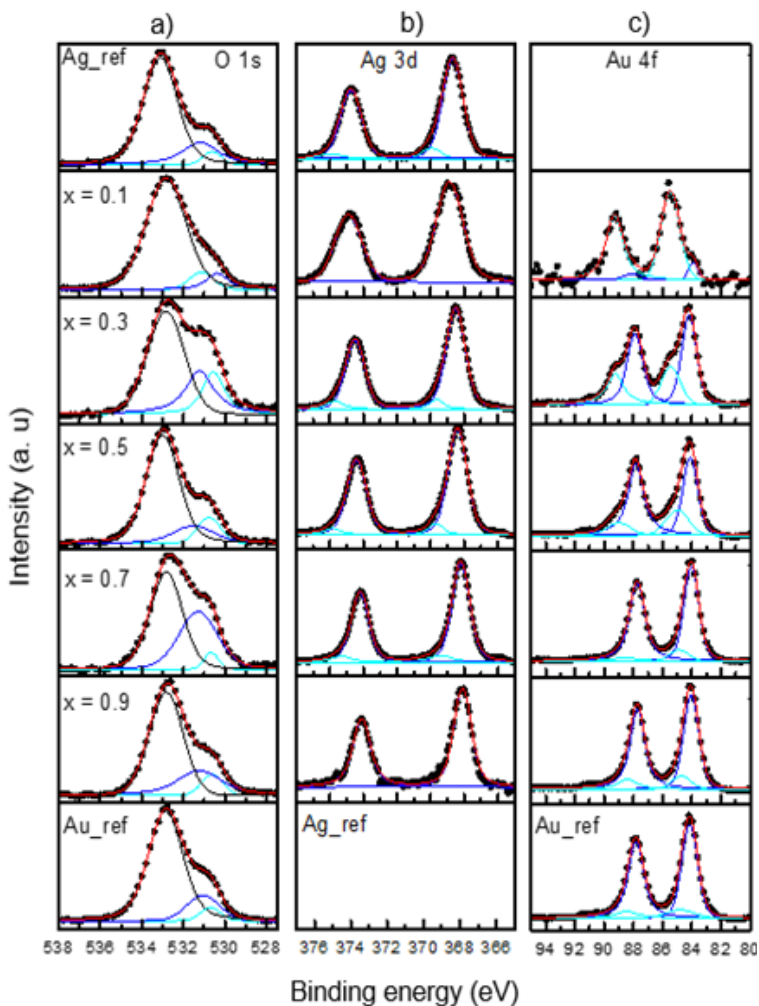
Figure 3.7. (a) O 1s, (b) Ag 3d and (c) Au 4f XPS spectra of the Au$_x$Ag$_{1-x}$ bimetallic clusters on TiO$_2$ from x = 1 to 0.

Upon increasing Ag concentration in the alloy (or decreasing the Au concentration), an increase of the Au 4f level is observed (**Figure 3.8**). This points towards a limited oxidation of Au by electron transfer from Au to Ag. A similar trend was previously observed for gas phase Au-Ag clusters deposited by CBD technique on a more inert SiO$_2$ support.[242] Detailed comparison of the BE peak positions of Au 4f$_{5/2}$ and Ag 3d$_{5/2}$ of Au$_x$Ag$_{1-x}$ bimetallic clusters on TiO$_2$ and SiO$_2$ supports (**Figure 3.9**) shows a relatively similar electronic state for Au in Au$_x$Ag$_{1-x}$ bimetallic clusters on both supports, whereas Ag is slightly more oxidized on TiO$_2$ than on SiO$_2$ support. This suggests an higher electron transfer from Ag to the TiO$_2$ support.
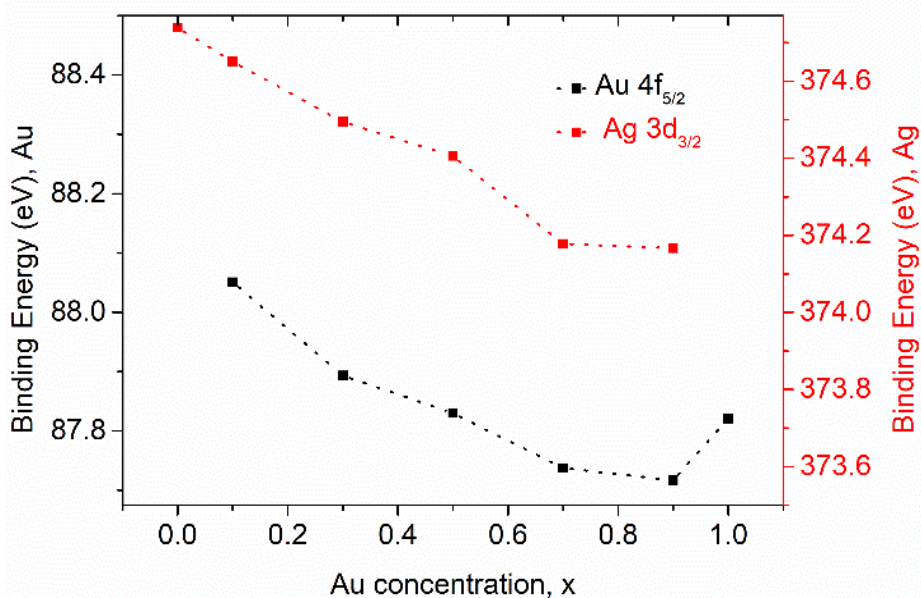
Figure 3.8. Binding energy shift of Au 4f$_{5/2}$ and Ag 3d $_{3/2}$ as a function of the Au concentration in bimetallic Au$_x$Ag$_{1-x}$.
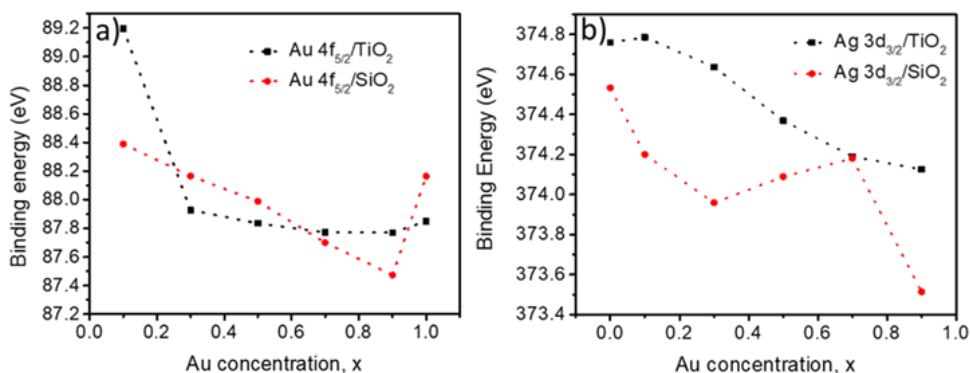
Figure 3.9. Binding energies of Ag 3d $_{3/2}$ and Au 4f $_{5/2}$ states in Au$_x$Ag$_{1-x}$ bimetallic clusters deposited on TiO₂ and SiO₂. The values for the clusters on SiO₂ are taken from ref. [146].

To complement the XPS analysis, X-ray absorption near edge structure (XANES) spectra at Au L₃-edge spectra of the series of Au-Ag bimetallic clusters deposited on TiO₂ (Au$_{0.1}$Ag$_{0.9}$ and Au$_{0.9}$Ag$_{0.1}$) and on carbon (Au$_{0.7}$Ag$_{0.3}$, Au$_{0.5}$Ag$_{0.5}$ and Au$_{0.3}$Ag$_{0.7}$) along with that of the Au foil reference are presented in **Figure 3.10**. When two transition metals form an alloy, the overlap of their d orbitals occurs, causing the energy levels to split and shift. This interaction can lead to the formation of new electronic states, including some that are unoccupied. These new states appear near the Fermi level because the mixing of d orbitals from different metals can push some states closer to or above the Fermi level.[251] In XANES, these new unoccupied d states can be identified. As X-rays are absorbed, core electrons can be excited to these unoccupied states (typical photon energy range of 0.1 to 100 keV). The resulting absorption spectrum reveals the electronic structure of the material, highlighting any new states created by the d orbital overlap. In **Figure 3.10**, although all spectra feature a metallic profile, a gradual blue shift of the edge position accompanied by a marked increase in the white line area (0-20 eV above the onset of absorption reaching a maximum for the Au$_{0.5}$Ag$_{0.5}$ composition) are observed upon alloying Au with Ag. Since the Au L₃-edge white line corresponds to the 2p$_{3/2}$-5d$_{5/2}$ and 5d$_{3/2}$ dipole-allowed transitions, this indicates an increase in the number of unoccupied states of d character in the vicinity of the Fermi level in the

73

bimetallic clusters, similar to what was reported in Au-Ag bulk alloys.[252,253,254] This results from a complex charge-compensation mechanism where Au loses d and gains s-p electrons, while Ag loses s-p and gains d electrons.[243]

Electron depletion on Au atoms supports the increase of the Au 4f BE with decreasing x in the XPS spectra. Although the net charge flow between Au and Ag atoms is expected to be extremely small,[255] this composition-dependent charge redistribution may impart chemical stability to the bimetallic cluster and protect the Ag atoms against oxidation.[252] Moreover, as the d-band centre of the metal surface is related to the adsorbate binding energy, this electron transfer may directly affect the catalytic properties of the clusters.[256, 257, 258]
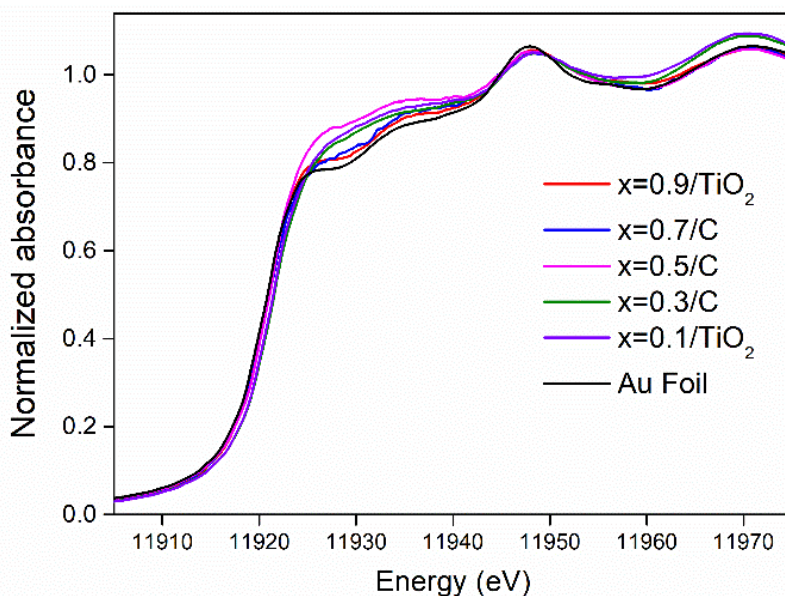
Figure 3.10. XANES spectra of gold rich to silver rich clusters on TiO₂ and carbon and of a gold foil reference.

3.3.3. Optical characterization

The optical properties of the cluster-modified films were characterized by UV-Vis (diffuse reflectance) spectroscopy. The spectra with clusters were normalized to a pristine P25 spin-coated substrate (*i.e.* P25 was taken as background). The subtraction of the P25 sample from the measurements is required to get a glimpse of the clusters' plasmon bands, since small few-nm clusters are known to exhibit a rather weak and broad plasmon response in the absorbance spectrum.[59,259,260] Optical characterization of Au-Ag bimetallic clusters deposited on TiO₂ highlights the modification of the surface plasmon resonance absorbance of Au-Ag clusters on TiO₂ upon changing the composition.
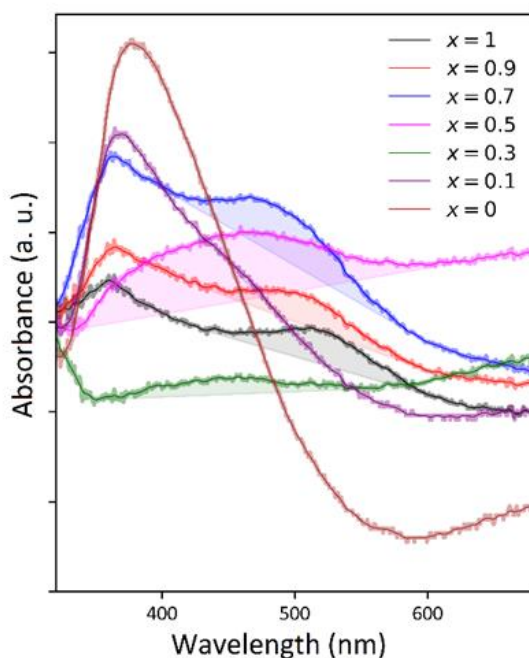
Figure 3.11. UV-Vis absorption spectra of TiO₂ modified samples with $Au_x Ag_{1-x}$ (x = 0.9, 0.7, 0.5, 0.3 and 0.1) after subtraction of pristine TiO₂ as background. The overall shape of the curves is dominated by the background subtraction, but the plasmonic features in the 400-550 nm range are apparent (shaded areas).

The UV-Vis spectra in **Figure 3.11** show two characteristic absorption bands for all compositions except for pure Ag and Au$_{0.1}$Ag$_{0.9}$: one below 400 nm and the other between 400 nm to 550 nm. The band below 400 nm can be attributed to the band gap of TiO$_2$ substrate, which dominates the absorbance of most samples. Its varying intensity among the different samples is related to the inherent inhomogeneity of the powder coating. Therefore, the P25 background subtraction cannot perfectly remove this contribution. Actually, for the x = 0.5 and x = 0.3 compositions it is overcompensated, resulting in an effective dip in the absorbance. A low intensity but clearly discernible broad absorbance bands can be observed in the visible region between 400 nm and 550 nm for all samples, except for the two most silver-rich samples. This is the LSPR band, which for the most silver-rich samples overlaps with the absorption edge of TiO$_2$ and can therefore not be distinguished. Furthermore, there is a distinct red-shift of the plasmon band maximum with increasing gold content in the clusters, as is known for Au-Ag alloys.[261,262] As size-dependent plasmon shifts are only expected in case of large particle size differences (i.e. tens of nm),[210,226,263,264,265,266] the very minor variations in the mean cluster diameter detected with EXAFS between the samples (**Table 3.1**) indicate that the tuning of the LSPR wavelength of Au-Ag clusters in this work mainly originates from changes in the Au$_x$Ag$_{1-x}$ alloy composition.

3.3.4. Photocatalytic self-cleaning activity

The photocatalytic self-cleaning activity of films consisting of clusters on TiO$_2$ was tested for all compositions by monitoring the degradation of stearic acid from their surface. The quantity of stearic acid remaining on the sample surface was determined by integrating the area of the IR band between 2800 and 3000 cm^{-1}. The values for each composition are plotted versus illumination time under both UV and simulated solar light in **Figure 3.12**. The small differences in the initial values of the integrated absorbance of the different samples are attributed to slight variations in the SA loading. However, the linear decrease in the concentration of reactant with time indicates that SA degradation is a zero-order reaction whose rate is independent of the initial concentration of SA, which is typical for non-porous self-cleaning surfaces.[190, 262]

The photocatalytic performance is expressed by means of the formal quantum efficiency (FQE):

$$\text{FQE} = \frac{\text{(the rate of stearic acid degradation in molecules/cm}^2\text{/s)}}{\text{(the rate of incident light in photons/cm}^2\text{/s)}}$$

FQEs of the degradation experiments under both UV light and the solar simulator are given in **Figure 3.13** as a function of the cluster composition and loading. Upon UV excitation, the photoactivity of the Au-Ag clusters-modified TiO$_2$ films towards stearic acid degradation remains basically unchanged compared to pristine TiO$_2$ (the measured FQE of P25 is 2.89×10^{-3} molecules/photon) (**Figure 3.13a**). Only for pure silver clusters (x = 0), a 20% enhancement for the cluster samples is observed, which may be explained by the fact that LSPR of silver is in the UV range. On the other hand, a significant activity enhancement is observed under the solar simulator with a very clear composition-dependent volcano-type trend peaking at the Au$_{0.3}$Ag$_{0.7}$ composition (**Figure 3.13b**). The FQE of the Au$_{0.3}$Ag$_{0.7}$ sample (39×10^{-6} molecules/photon) is twice as high as that of pristine TiO$_2$ (19×10^{-6} molecules/photon). The non-zero FQE of the pristine TiO$_2$ can be attributed to the small fraction of UV light present in the broad spectrum of the solar simulator that becomes the baseline level for all samples. Under green light illumination the pristine sample was found to have a FQE of only 0.45×10^{-6} molecules/photon.[235]
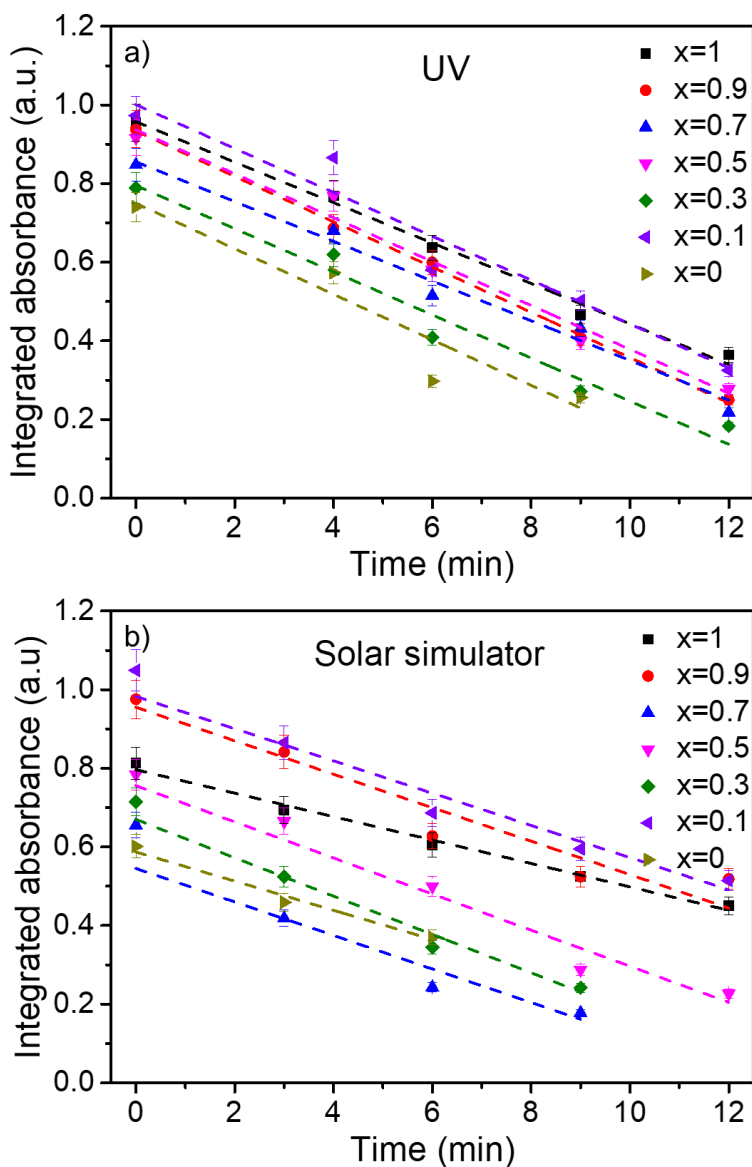
Figure 3.12. Evolution of integrated FTIR absorbance of stearic acid between 2800 to 3000 cm^{-1} as a function of illumination time on the Au$_x$Ag$_{1-x}$ clusters modified TiO₂ under a) UV and b) Solar Simulator illumination.
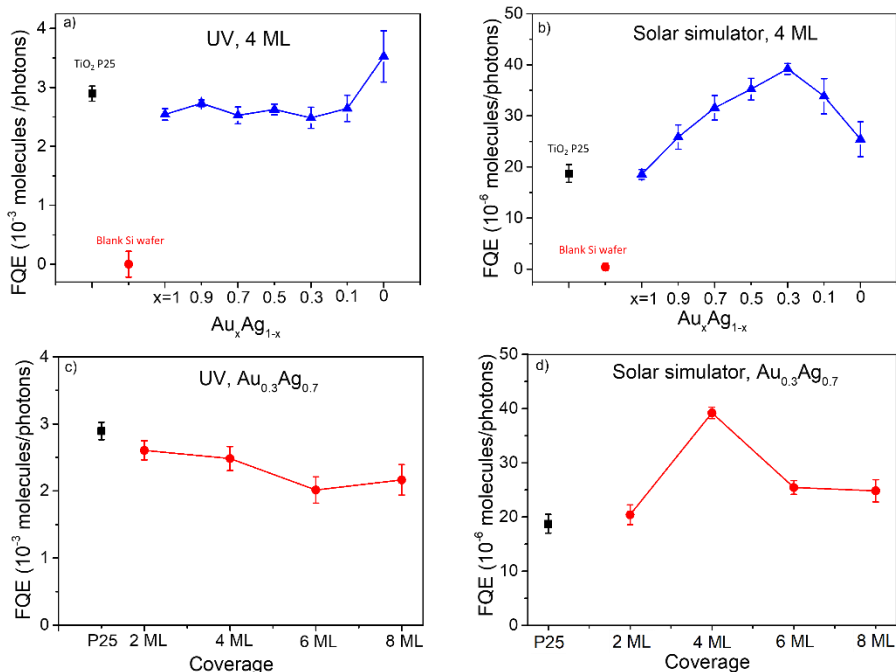
Figure 3.13. FQE under (a) UV and (b) solar simulator as a function of bimetallic Au$_x$Ag$_{1-x}$ cluster composition on TiO$_2$ for 4 ML coverages. FQE under (c) UV and (d) solar simulator as a function of the bimetallic Au$_{0.3}$Ag$_{0.7}$ cluster coverage.

The dependence of the photoactivity on the cluster loading was investigated for the best performing composition, Au$_{0.3}$Ag$_{0.7}$. Clusters of this composition were deposited on TiO$_2$ with 2, 4, 6 and 8 ML loadings. Under UV illumination, the performance of all samples is similar, except for a 20% decrease in degradation efficiency at the highest loadings of 6 ML and 8 ML (**Figure 3.13c**) due to the blocking of catalyst active sites by large amount of material. Under solar light, the 4 ML loading of Au$_{0.3}$Ag$_{0.7}$ clusters shows the highest photoactivity in comparison to other loadings (**Figure 3.13d**). It proves that the 2 ML loading is not optimal for the nanoclusters to exhibit higher efficiency while higher loadings, 6 ML and 8 ML, prevented light from reaching the TiO$_2$ catalyst resulting in lower efficiency.

3.3.5. Electromagnetic Simulations

Among the different enhancement mechanisms of the photocatalytic activity driven by plasmonic nanoparticles in contact with TiO_2 semiconductor, hot electron injection from the plasmonic metal to the TiO_2 conduction band, and near-field enhancement in close proximity of the plasmonic structures, are the two most widely adopted mechanisms in literature.[212,267,268,269] Electromagnetic simulations were performed to investigate the dependence of the LSPR position and the degree of near-field enhancement on the cluster composition. Although quantum size effects grow stronger for sizes below 5 nm,[270] that is the mean size of our clusters, the relative plasmonic response remains similar to larger nanoparticles [230] as proven by several literature studies.[271] Ag nanoparticles exhibit a plasmonic response even at sizes down to *ca*. 2 nm which is not over-shadowed by the quantum effects in the optical response.[272] However, for Au of the same diameter the quantum size effects dominate hiding the plasmon band in the optical spectra.[273] Similar trends are assumed for bimetallic clusters. Thus, although the quantum effects can be quite significant in small clusters, the classical plasmonic response can still be evaluated for a comparative analysis. Details of the computational procedures can be found elsewhere.[274] The main assumptions are that (i) the bulk alloy optical parameters are representative and (ii) the effect of the TiO_2 substrate is the same for all samples and can be ignored in the comparison. Consequently, the simulations were performed with air as surrounding medium for computational simplicity. In **Figure 3.14**, Mie extinction spectra and near-field enhancement spectra of clusters of different Au-Ag compositions are compared with the solar spectrum.[275] Silver is a superior plasmonic material with a higher optical cross section and near-field enhancement than gold, whose plasmonic response is damped by direct interband transitions. However, the high affinity of silver towards oxygen can lead to a drastic reduction of the plasmonic excitation while Au is more chemically stable.

Our results suggest that the bimetallic Au-Ag may thus combine a high plasmonic response (due to Ag) with chemical stability (due to Au). The electron transfer from Au to Ag identified by XANES and XPS and the absence of detectable trace of oxide in the EXAFS analysis point toward a significant synergetic effect upon alloying Ag with Au, that could significantly increase the stability of the bimetallic Au-Ag clusters. The simulated near-field enhancement spectra of the different Au-Ag clusters presented in **Figure 3.14b**. $(E_{sc}/E_{inc})^2$ is the near-field enhancement averaged over the surface of the clusters up to a

radial distance of 10% of the cluster. E_{sc} is the scattered electric field resulting from the interaction of the incident light with the nanoparticle, and E_{inc} is the incident electric field that interact with the nanoparticle. The near-field enhancement map of Au$_{0.3}$Ag$_{0.7}$ at 420 nm presented in the inset clearly shows the dipolar response of the cluster. Although silver-rich Au$_{0.1}$Ag$_{0.9}$ clusters feature the strongest near-field enhancement (**Figure 3.15**), their maximum resonance wavelength occurs at 380 nm where the intensity of the solar simulator is low. Thus, in spite of the high extinction cross section and near-field enhancement, Au$_{0.1}$Ag$_{0.9}$ clusters cannot effectively enhance the photocatalytic process under solar light. Despite featuring the best overlap of the plasmon resonance with the spectrum of the light source, the band maximum of pure gold clusters that is positioned at 500 nm is far below the TiO$_2$ band-gap energy (3.2 eV or 387 nm). In contrast, the alloy Au$_{0.3}$Ag$_{0.7}$ that has an intermediately strong resonance, centered on the high energy wavelengths of the solar simulator (UV blue-teal), with thus sufficiently high energetic photons, presents the best compromise between available photons, energy of the photons and strong field enhancement (**Figure 3.14b**).

The fact that Au$_{0.3}$Ag$_{0.7}$ features the best activity strongly suggests that near-field enhancement is one of the dominating mechanisms for improving the photocatalytic degradation of stearic acid under solar simulator. This is consistent with the poor activity measured for pure Au clusters, whose modest near-field enhancement due to interband transition is limiting its plasmonic enhancement and associated hot electron mediated processes.[276] Mixing Au with silver is both reducing gold interband transition and stabilizing silver in a metallic form.[277,278] This is also in agreement with earlier work suggesting the dominant role played by the near field enhancement as well as hot electron injection in plasmonic photocatalytic self-cleaning reactions.[220,276] To further explain the superior activity of the Au$_{0.3}$Ag$_{0.7}$ clusters under solar light, one should also take note of the well-known blue-shift of the LSPR for small clusters.[279, 280] The electron spill-over effect in small clusters that leads to such blue-shifts requires atomic scale investigations that are out of the scope of this thesis.[281]
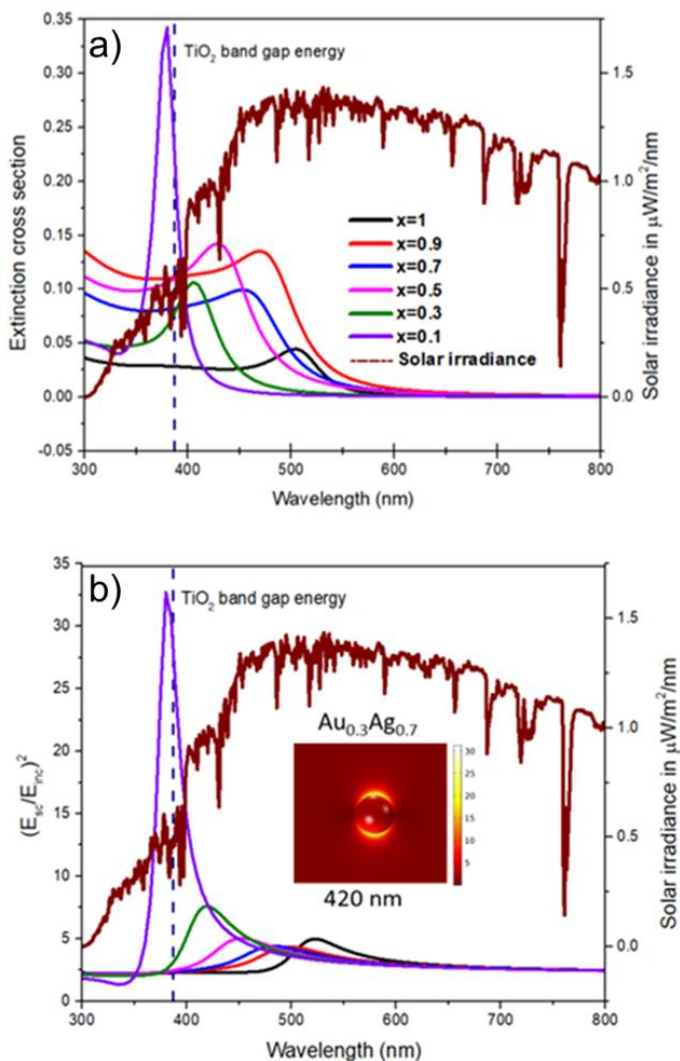
Figure 3.14: a) Mie extinction spectra (normalized by the projection area of the nanoparticles) of nanoparticles of different compositions compared with the solar spectrum used. b) Near-field enhancement spectra of nanoparticles (averaged over the surface of the nanoparticles up to a radial distance of 10% of the diameter) of different compositions compared with the solar spectra. Solar spectrum refers to right axis.
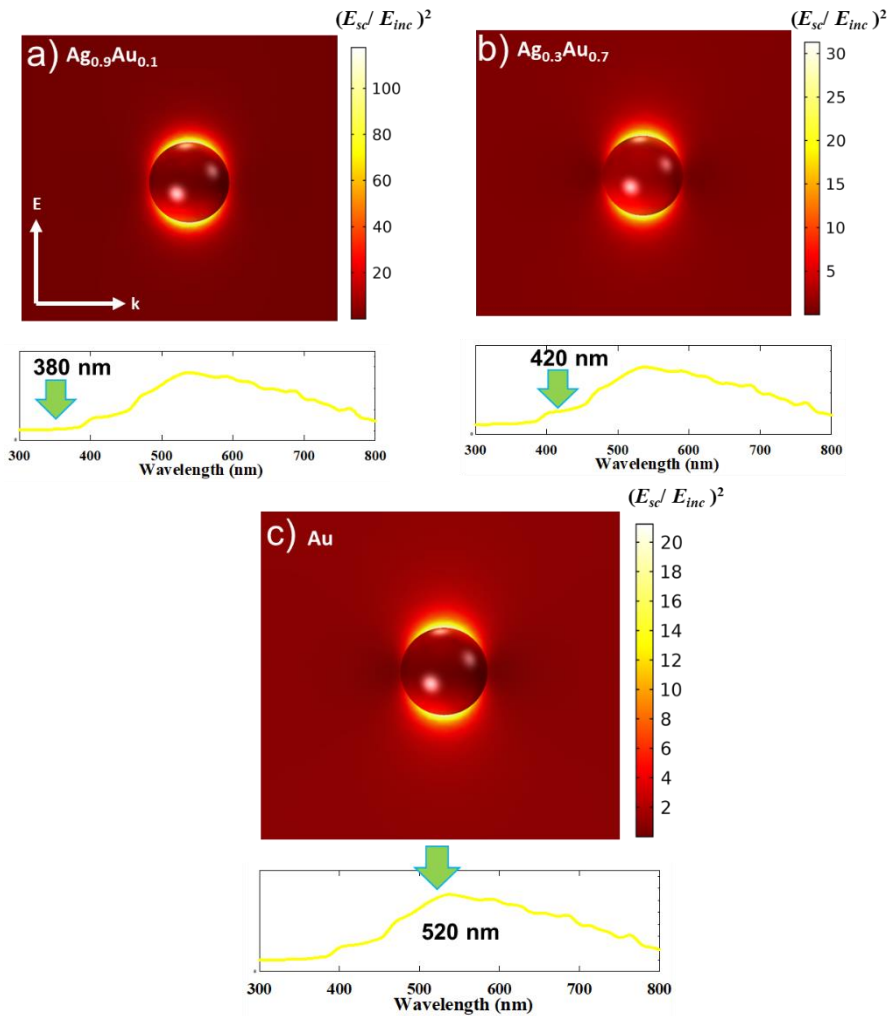
Figure 3.15. Near-field enhancement maps of isolated nanoparticles of three different compositions namely (a) Au$_{0.1}$Ag$_{0.9}$, (b) Au$_{0.3}$Ag$_{0.7}$ and (c) Au with the solar light intensity at their LSPR wavelengths 380 nm, 420 nm and 520 nm, respectively. E and k vectors in (a) represent direction of electric field and the light wave, respectively.

3.4. Discussion

The well-defined nature and uniformity of the Au$_x$Ag$_{1-x}$ bimetallic deposited clusters has allowed their precise characterization highlighting strong structural (atomic arrangement), electronic (electron transfer from Au to Ag) and plasmonic (Mie extinction and near-field) synergetic effects tailored by the cluster composition. The 20% enhancement for samples containing silver-rich clusters under UV light can be explained by the LSPR of silver nanostructures being in the UV range of the spectrum. This leads to efficient near-field enhancement, and is consistent with earlier work.[282,283] The UV light source has a broad spectral width and there is a good overlap of the light source emission spectrum and the band gap absorption band of the semiconductor, resulting in the observed enhancement in silver-modified (FQE of 3.5×10^{-3} molecules/photon) compared to pristine TiO$_2$ (2.9×10^{-3} molecules/photon). These values are of the same order of magnitude as for TiO$_2$ films of Mills et al., ($1.5\text{-}4.8 \times 10^{-3}$ molecules/photon),[189,284,285,286] which is similar to the range found by Kenanakis et al.[287] and Queseda-Cabrera et al.[288] for ZnO films on N-doped TiO$_2$ with FQE's reaching up to 2.77×10^{-3} molecules/photon. A FQE of 1.09×10^{-3} molecules/photon was found for TiO$_2$ (10 nm) modified by Ag (2 nm) nanoparticles generated by a liquid flame spray technique.[289] It should however be noted that true comparisons remain difficult, due to the lack of standardized measuring conditions. Even though all the mentioned studies use the same UVA light source and model reaction, different photocatalyst amounts still hamper the comparison. Under simulated solar light, plasmonic samples are more active than P25 and therefore this photoactivity cannot be attributed only to the UV part of the simulated solar light, but also to the presence of clusters on the surface of P25 that interact with visible light. These results support the hypothesis that an additional synergistic effect occurs between the plasmonic clusters and the TiO$_2$ support excited under solar irradiation (i.e. by simultaneously exciting the semiconductor with UV light and the plasmonic clusters with visible light).[290,291]

Nonetheless, the FQE under solar light remains much smaller than that under UV. Interestingly, some studies have observed traces of activity of P25 even under pure visible light (which is unexpected due to large band gap of TiO$_2$). This activity is generally attributed to the presence of intrinsic surface defect levels in P25 as demonstrated by means of EPR and photoluminescence studies.[292,293] The FQE obtained for 4 ML Au$_{0.3}$Ag$_{0.7}$ under solar light is two orders of magnitude higher (39×10^{-6} molecules/photon) than the value found in the

literature under pure visible light (490 nm) illumination (0.39×10^{-6} molecules/photon) where colloidal Au$_x$Ag$_{1-x}$ nanoparticles were synthesized using a modified Turkevich procedure.[261] This likely is not only due to the usage of solar illumination with some part of UV but also to the smaller sizes of the ligand-free clusters (< 5 nm) synthesized through the CBD technique in comparison with the sizes of nanoparticles prepared through colloidal methods in literature (20-40 nm).[231] Smaller particles deposited on semiconductors, have been reported to lead to enhanced photocatalytic efficiencies, as compared to larger ones.[294,295] This has been attributed to the ability of smaller nanoparticles, more effectively channeling photoelectrons between the semiconductor and the metal nanostructure, which may in turn contribute to higher FQE.

In our experiments, the observed decrease in efficiency of ca. 20% for the higher loadings of 6 ML and 8 ML can be attributed to the blocking of the catalyst active sites by the clusters that prevents a large fraction of the incoming light from reaching the catalyst in contrast with less loaded samples. This is supported by the SEM images of 6 ML and 8 ML in **Figure 3.4** Under solar light, 4 ML loaded Au$_{0.3}$Ag$_{0.7}$ clusters shows the highest photoactivity. This results from the combination of the following four contributing factors: (i) the LSPR effect of the bimetallic nanoparticles in the visible light wavelength range that can give rise to either hot electron injection or strong enhancement of the near electric field or both; (ii) a quantitative overlap of LSPR wavelength of Au$_{0.3}$Ag$_{0.7}$ composition with the sun's irradiance spectrum and a strong near-field enhancement in this wavelength range that has significant intensity as well as sufficient individual photon energy; (iii) the low and optimal total metal loading (4 ML) which still leaves enough TiO$_2$ surface available for UV light absorption; (iv) electron transfer (from Au to Ag).

3.5. Conclusions

We have demonstrated that CBD is an efficient approach for fabricating well-defined tunable Au$_x$Ag$_{1-x}$ plasmon-based photocatalysts, outperforming their counterparts obtained through a colloidal method in photocatalytic self-cleaning applications. The photocatalytic performance of TiO$_2$ P25 under both UV and simulated solar light was tested by modifying its surface with Au$_x$Ag$_{1-x}$ plasmonic clusters of different compositions. Their detailed investigation facilitated by their low polydispersity highlighted clear beneficial synergetic effects, including an excellent stability due to alloying as well as a large specific surface area due to their small sizes. The surface plasmon resonance induced by Au$_x$Ag$_{1-x}$ clusters helps the TiO$_2$ to absorb light over a broad wavelength range

85

by tuning the composition of the clusters. The photoactivity of all the compositions (x= 0, 0.1, 0.3, 0.5, 0.7, 0.9 and 1) towards SA degradation is basically unchanged compared to pristine TiO$_2$ under UV, while a significant enhancement is observed under simulated sunlight with a very clear composition-dependent volcano-type trend peaking at the Au$_{0.3}$Ag$_{0.7}$ composition, for an optimal loading of 4 MLs. We have devised that this cluster composition combines a good overlap of its plasmon band with the irradiance spectrum, and the availability of sufficiently high energy photons in that wavelength range. These results do not only support the tuning of the LSPR wavelength with changing composition to design highly efficient tailored photocatalysts, but also showcases the prospects of CBD technology in synthesizing gas-phase Au-Ag bimetallic clusters with controllable small sizes and compositions, without the use of solvents or organic ligands, which is a clear benefit over wet chemistry or colloidal methods.

Chapter 4

Composition-dependence of PEC water splitting by atomically restructured AuCu nanocluster modified titania nanotubes

This chapter is based on the following manuscript (under preparation):

Composition-dependence of PEC water splitting by atomically restructured AuCu nanocluster modified titania nanotubes

Vana Chinnappa Chinnabathini, Karthick Raj Ag, Imran Abbas, Thi Hong Trang Nguyen, Zviadi Zarkua, Thi Hang Hoang, Peter Lievens, Didier Grandjean, Sammy W. Verbruggen, and Ewald Janssens

Author contributions

4.1. Introduction

The n-type semiconductor TiO_2 is known for its good stability, high resistance to corrosion, non-toxicity, bio-compatibility and low cost production. TiO_2 nanostructures, including nanoparticles,[296] nanowires,[297] nanorods,[298] nanotubes,[299] and nanopores[300] are intensively studied, particularly for photocatalysis. Anodic oxidation of a metallic titanium foil allows for the simple and efficient synthesis of highly ordered titania nanotubes (TNTs), whose length and diameter can be conveniently tuned by the applied voltage, anodizing time, annealing temperature, and the composition of the electrolyte.[301,302,303,304] Since the pioneering work of Zwilling et. al.,[305] about the anodic oxidation of titanium into highly ordered titania nanotubes, the morphology of TNTs has extensively been studied as well as their potential applications in catalysis. Self-assembled TNT arrays possess exceptional structural, electrical, thermal and optical properties that render them suitable for a lot of applications.[90,91,306,307,308,309,310,311,312] TNTs have important applications in photocatalysis[121] in solar cells, environmental purification, water photolysis, gas sensing, and bio-medical applications[122,123] due to their highly ordered structure, mechanical and chemical stability, corrosion resistance, high specific surface area,[313,314] enhanced charge transfer, and large number of active sites.[315,316] By diminishing dimensions to the nanoscale, the specific surface area increases, while the modified electronic structure of TNTs diminishes the electron-hole recombination rate. The large effective surface area in direct contact with the electrolyte enables diffusive transport of photogenerated holes to the oxidizable species in the electrolyte of photoelectrochemical (PEC) cells. The effects of parameters like annealing temperature, crystallinity, wall thickness, tube length and diameter of the TNTs on the PEC activity has been discussed in several reviews.[125,317,318]

Although TiO_2 has suitable band-edge positions for electrochemical water splitting because bottom of the conduction band is more negative than the H_2/H_2O redox potential (0 V) and the top of the valence band is more positive than the H_2O/O_2 redox potential (-1.23 V),[319,320,321,322] its bandgap (about 3.2 eV for anatase) allows only UV light to be efficiently used. Various modifications, particularly the incorporation of metal NPs, have been employed to enable visible light driven processes. The NPs such as Ag, Au and Cu possess strong ability to absorb solar photons due to their LSPR effect[323] and transfer the energetic electron formed in the process of SPR excitation to the nearby semiconductor.[52] SPR induced near field enhancement at surface of the metallic

nanostructures can contribute to the generation of electron-hole pairs during photocatalysis. It has been well established that metal NPs on the surface of TiO$_2$ can act as traps for photo-induced electrons, preventing fast charge carriers recombination[44,324,325] and thus enhancing the PEC activity of TNTs. Several examples of improved photocurrents in TNTs decorated with monometallic Au, Cu or Ag NPs can be found in the literature.[326,327,328,329,330,331,332] For instance, the photocurrent densities of about 90 µA/cm^2 and 80 µA/cm^2 were recorded under 350 nm irradiation and 1 V vs. SCE for TNTs modified with Cu and Ag NPs, respectively.[333] The modification of TNTs with plasmonic BNPs combines LSPR effect with synergistic properties arising from the combination of two metals, [113,334, 335,336] and provide highly active metal–support interfaces suitable for PEC reactions.[337,335,338] For example, TNTs modified with atomically precise AuCu alloy BNPs exhibit improved photocurrent (150 µA/cm^2 at 0.61 V) in comparison with blank TNTs substrate under visible light (λ > 420 nm) irradiation.[339] TNTs modified with AuCu nanoparticles thermally treated in argon exhibited higher photocurrent (64 µA/cm^2 at -0.2 V) under UV–Vis light range as pristine TNTs electrode (32 µA/cm^2).[340]

To the best of our understanding and knowledge, there is limited information available on modifying TNTs for PEC water splitting with AuCu NCs. We have synthesized and deposited small-sized (< 5 nm) AuCu nanoalloys at a low metal loading (4 atomic monolayers, equivalent to a 0.25 nm film or about 0.5 µg/cm^2) on TNTs with a precise control over the composition and coverage and tested their PEC water splitting performance. The AuCu NCs-modified TNT photoanodes exhibit an excellent photostability, high composition-dependent photoactivity in the visible range of the solar spectrum. The nanoclusters with different compositions were synthesized through the CBD process[113] that produces ligand-free, size- and composition-tuneable NCs with high degree of purity and uniform coverage. We demonstrate the exceptional enhancement in PEC performance of the as-prepared AuCu NCs modified TNTs as photoanodes for photocurrent generation as compared to pristine TNTs.

4.2. Sample preparation and methods

Figure 4.1 schematically summarizes the synthesis of TNTs from a titanium foil and the subsequent deposition of Au$_x$Cu$_{1-x}$ (x = 1, 0.75, 0.5, 0.25 and 0) BNCs using the CBD technique.
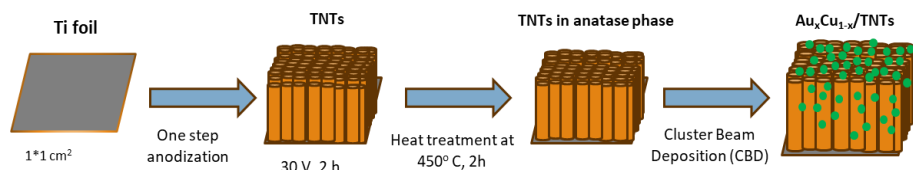
Figure 4.1. Schematic illustration of synthesis of AuCu nanocluster   modified titania nanotubes.

4.2.1. Preparation of AuCu NCs modified samples

Anodization of 1 mm thick titanium foil (1×1 cm^2) was carried in an electrolyte mixture containing 40 ml of ethylene glycol, 0.5 wt% of ammonium fluoride, and 2 vol% water. A platinum foil (1×1 cm^2) was used as the cathode and a DC voltage was applied using a Voltcraft PPS DC power supply. Before anodization, the Ti foil was ultrasonically cleaned and rinsed with acetone, ethanol, distilled water, and then dried under N$_2$ gas flow for a few seconds. A one-step anodization was used to form a porous titanium oxide film with controllable pore size and good uniformity.[341] The initial stage of the anodization process was carried out at 30 V for 2 h. The grown TNTs were then cleaned with distilled water and dried under a N$_2$ stream. Subsequently, the samples were subjected to a 2 h heat treatment at 450 °C, aiming to transform the amorphous titania into the anatase phase.[342,343] This step is crucial because decreasing the amorphous regions in the nanotube walls diminishes the presence of charge carrier recombination centers. Next, the prepared TNTs substrates were modified with AuCu BNCs with equivalent atomic coverages of 4 ML using laser ablation cluster course.

The NCs are produced by pulsed laser (10 Hz, Nd:YAG laser, INDI, Spectra Physics) ablation of mono and bimetallic Au$_x$Cu$_{1-x}$ (x = 1, 0.75, 0.5, 0.25 and 0) plate targets (ACI Alloy, purity 99.995%) and condensation in a helium atmosphere (introduced though a pulsed valve with a backing pressure of 7.5 bar). Following expansion into vacuum a beam of clusters is formed. The cluster size distribution can be tuned by adjusting the laser energy density, the helium pressure, and the time lag between the target ablation and the introduction of the He carrier gas.[156] Prior to cluster deposition, the gas phase size distribution of cationic clusters is characterized by time-of-flight mass spectrometry.

Assuming a spherical shape and bulk density for all NC compositions, the diameter distribution has a maximum around 2 nm as shown in **Figure 4.2.**

The size distribution obtained here reflects the distribution of cationic clusters accelerated by extraction in the *in situ* ToF-MS. However, all charge states, including neutral and anionic clusters, are deposited on the substrate. The cluster beam predominantly contains neutral clusters. The slight variation in the average cluster size of different compositions (difference of around 0.5 nm) is due to the adjustment of parameters, specially laser energy and laser and extraction timings, to maximize the mass flux measured by the QCM. This size variation is not expected to have a significant impact on the activity because plasmonic effects are expected to change only slightly with size, particularly when size changes are small (here between 1.8 and 2.5 nm).[226] But the final size of the particles on the substrate is different because of some mobility and aggregation (as discussed in section 4.3.1) On the other hand, increasing the loading results in larger particle sizes on the support and this does affect the activity of the photocatalysts, as will be discussed in section 4.3.1.
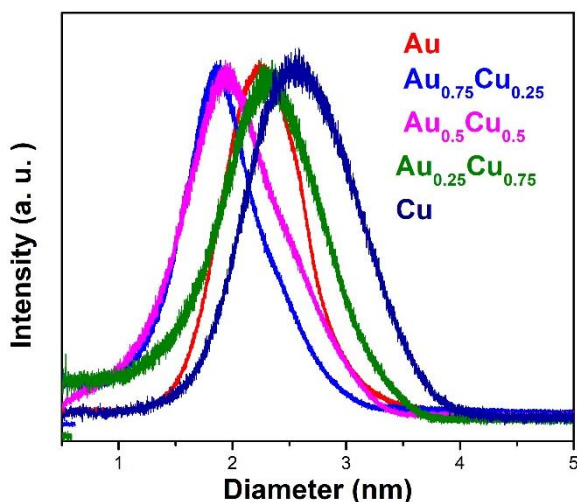
Figure 4.2. Size distributions of Au_xCu_{1-x} (x = 1, 0.75, 0.5, 0.25, and 0) NCs as measured by time-of-flight mass spectrometry prior to cluster deposition (Normalized). The cluster diameter is deduced from the measured mass assuming a spherical shape and bulk density.

The AuCu NCs are deposited on the TNTs supports by simply placing the supports perpendicular to the molecular beam in an ultra-high vacuum deposition chamber (6.8×10^{-8} h Pa). The depositions occur under soft-landing conditions, given a speed of the cluster beam of about 700 m s^{-1} (corresponding to a kinetic energy of 0.3 eV per atom). The loading of the NCs is determined by the deposition time and the mass flux measured before and after cluster deposition using a quartz crystal microbalance (QCM). Typical fluxes are 0.062 µg /cm^2/minute. The mass loading can also be expressed in an equivalent number of atomic monolayers (ML, *i.e.* a thickness equivalent to a film of 0.25 nm).

4.2.2. Sample characterization

Different characterization techniques were applied to investigate the structural (X-ray diffraction, electron microscopy), optical (UV-Vis and photoluminescence), and photoelectrochemical properties of the BNC-modified TNTs.

X-Ray Diffraction (XRD) was performed on all Au$_x$Cu$_{1-x}$ BNC modified TNTs samples using a Bruker D8 advance diffractometer equipped with a LYNXEYE XE-T detector and Cu Kα source emitting radiation of 1.54 Å. Measurements spanned a 2θ range from 10° to 90°, with a scan rate of 0.5 s step^{-1}. The diffractograms were analyzed using Bruker's DIFFRAC.EVA software, with phase identification achieved by comparison with the ICDD database.

The surface morphology of the as-prepared samples was characterized with Scanning Electron Microscopy (SEM) using a FEI Helios Nanolab G3 CX system (acceleration voltage of 10 kV). The cluster size distributions and compositions were analyzed with Transmission Electron Microscopy (TEM) using an aberration corrected Thermo Fischer Scientific Titan instrument. For the TEM studies, the AuCu NCs were deposited on molybdenum grids. The TEM was used at an accelerating voltage of 120 kV. Particle size distributions were obtained via the 'ImageJ' image analysis software.

Ultraviolet-Visible light absorbance spectra (UV-Vis) of cluster decorated TNTs samples were obtained in the 300-700 nm wavelength range using a double beam UV 2600 spectrophotometer (Shimadzu, Kyoto, Japan) equipped with film holders attached to a BaSO$_4$ coated integrating sphere of 60 mm in diameter. Steady state photoluminescence (PL) spectra were measured at room temperature using Shimadzu RF-6000 fluorescence spectrophotometer

equipped with a 150 W xenon lamp and a resolution of the measured emission spectra is 1 nm. All PL measurements were performed at an excitation wavelength of 310 nm.

Extended X-ray Absorption Fine Structure (EXAFS) and X-Ray Absorption Near Edge structure (XANES) experiments were performed at the LISA beamline (BM08)[236] of the European Synchrotron Radiation Facility (ESRF, Grenoble, France), operating in a 7/8 multi bunch mode with a current of 200 mA. Data was collected at the Au L_3-edge (E = 11919 eV) and the Cu K-edge (E = 8979 eV) in grazing incidence (incidence angle ~ 2° with the beam polarization perpendicular to the surface) and using fluorescence detection mode.

4.2.3. Photoelectrochemical applications

The photoelectrochemical performance of the pristine and Au_xCu_{1-x} (x = 1, 0.75, 0.5, 0.25 and 0) NCs-modified TNTs was studied using a three-electrode configuration in 0.5 M Na_2SO_4 at pH = 7.21. The pristine and NC modified electrodes (1 cm^2), platinum foil (1 cm^2) and aqueous silver/silver chloride (Ag/AgCl) electrodes[5] were used as a working, counter and reference electrodes, respectively. The performance of each working electrode was evaluated using linear sweep voltammetry (LSV), chronoamperometry (CA), and electrochemical impedance spectroscopy (EIS). EIS of the prepared photoanodes was measured under both illumination and dark conditions by applying an AC voltage amplitude of 10 mV at open circuit potentials (OCV) with a frequency ranging from 0.1 Hz to 100 kHz. The frequencies between 0.1 Hz to 1 Hz probe processes such as diffusion and mass transport. They can reveal information about the Warburg impedance, which is associated with ion diffusion through the electrolyte or porous electrodes. The frequencies between 1 Hz to 10 kHz correspond to charge transfer processes and double-layer capacitance at the electrode/electrolyte interface. They provide insights into the kinetics of electrochemical reactions and the capacitance of the double layer. High Frequencies from 10 kHz to 100 kHz are sensitive to the resistive components of the system, including solution resistance and contact

---

[5] Ag/AgCl reference electrode is a widely used reference electrode. It consists of a silver wire coated with silver chloride, which is immersed in a solution containing chloride ions.[344]

resistances. They can help in identifying the ohmic resistance of the electrolyte and the intrinsic resistance of the electrode materials.[345]

All measured potentials were converted to reversible hydrogen electrode (RHE) scale using the Nernst equation (4.1).

$$E_{RHE} = E_{Ag/AgCl} + (0.059 * pH) + E^o_{Ag/AgCl} \qquad (4.1)$$

where $E^o_{Ag/AgCl}$ = 0.098 V at 25° C, E_{RHE} is the potential versus RHE, and $E_{Ag/AgCl}$ is the measured potential with Ag/AgCl reference electrode.

The Scisun-300 solar simulator from Sciencetech, equipped with a xenon arc lamp and AM 1.5G filter, was used as a light source. The intensity of the light source was adjusted to 100 mW cm^{-2} by changing the working distance, and the intensity is measured using an Avantes photo spectrometer. To check and screen the PEC performance, the prepared electrodes were tested in a single PEC cell and the electrodes were positioned as close as possible to the front of quartz window to minimize the influence of light absorption by water.

The applied bias to photon conversion efficiency (*ABPE*) was calculated from the LSV data under AM 1.5G illumination.

$$ABPE = \frac{J_{ph}(\text{mA cm}^2) \times (1.23 - V)(\text{V})}{P_{total}(\text{mW cm}^2)} \qquad (4.2)$$

Where J_{ph} is the photocurrent obtained under applied potential *V* and P_{total} is the power density of incident illumination (100 mW cm^{-2}).

The charge transfer at the interface between the electrode and the electrolyte was studied through bode phase analysis. The hole-relaxation time or electron lifetime τ and the hole diffusion length L_d are given by equations (4.3) and (4.4):

$$\tau = \frac{1}{2\pi f_{max}} \qquad (4.3)$$

$$L_d = D\tau \qquad (4.4)$$

with f_{max} the frequency corresponding to the maximum phase in the range of 10 to 100 Hz and

D is hole diffusion coefficient = 5×10^{-2} cm^2 s^{-1} [346,347]

4.3. Results

4.3.1. Structural characterization of AuCu NC modified TNTs electrodes

XRD patterns of the annealed TNTs modified by AuCu NCs measured after PEC measurements are given in **Figure 4.3.** They show the typical pattern of TiO_2 anatase as well as the underlying metallic titanium substrate of the electrode on which the TNTs were grown on. No diffraction peaks of the deposited clusters could be detected likely due to their small loading in line with previous studies on TNTs modification with small metal clusters.[348,98] The abnormal enhancement of (004) diffraction peak intensity observed for all the samples indicates a preferred [001]-oriented anatase phase in TNT with the (004) lattice plane perpendicular to their axis. The variation of the ratio of the diffractions peaks corresponding to the anatase (004) and (011) planes can reflect variations of the orientation of the TNTs relative to the Ti substrate.[349]

Figure 4.4 shows top-view and cross-sectional SEM images of the pristine and NC decorated TNTs. The TNTs have an ordered nano-morphology with an average tube diameter of *ca*. 60 nm with a wall thickness of *ca*. 15 nm, or an inner diameter of *ca*. 30 nm, and an average tube length of ca. 2.5 μm (**Figure 4.4a** in the inset**)**. The BNC-decorated samples are found to have randomly distributed clusters (i.e. the small bright white dots in **Figures 4.4c and 4.4d**) on the top surface and the inner walls of the TNTs. There is no sign of cluster agglomeration, although this cannot be excluded with certainty because the resolution of the SEM (0.8 nm @ 30 keV) is of the order of the size of the clusters. Pure gold NCs appear more shiny and noticeably larger on the surface. **(Figure 4.4b)**. In contrast, the BNCs appear slightly smaller than the Au clusters.
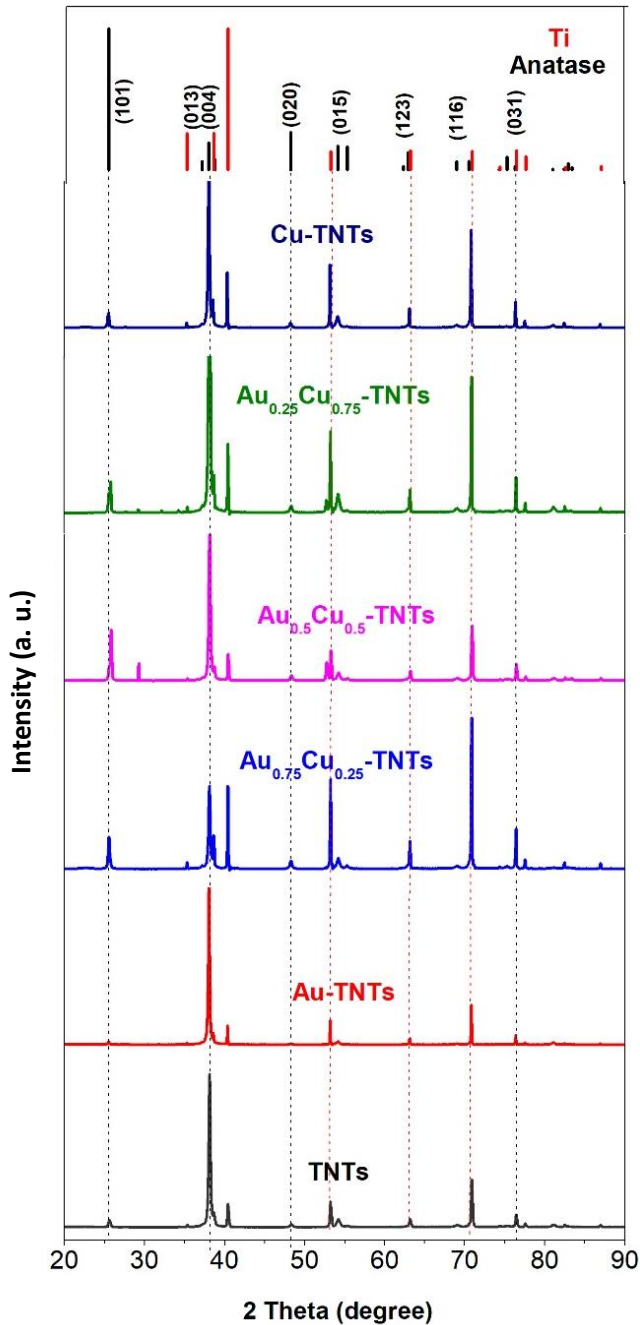
Figure 4.3. XRD pattern of pristine TNTs and Au_xCu_{1-x} NCs modified TNTs electrodes.
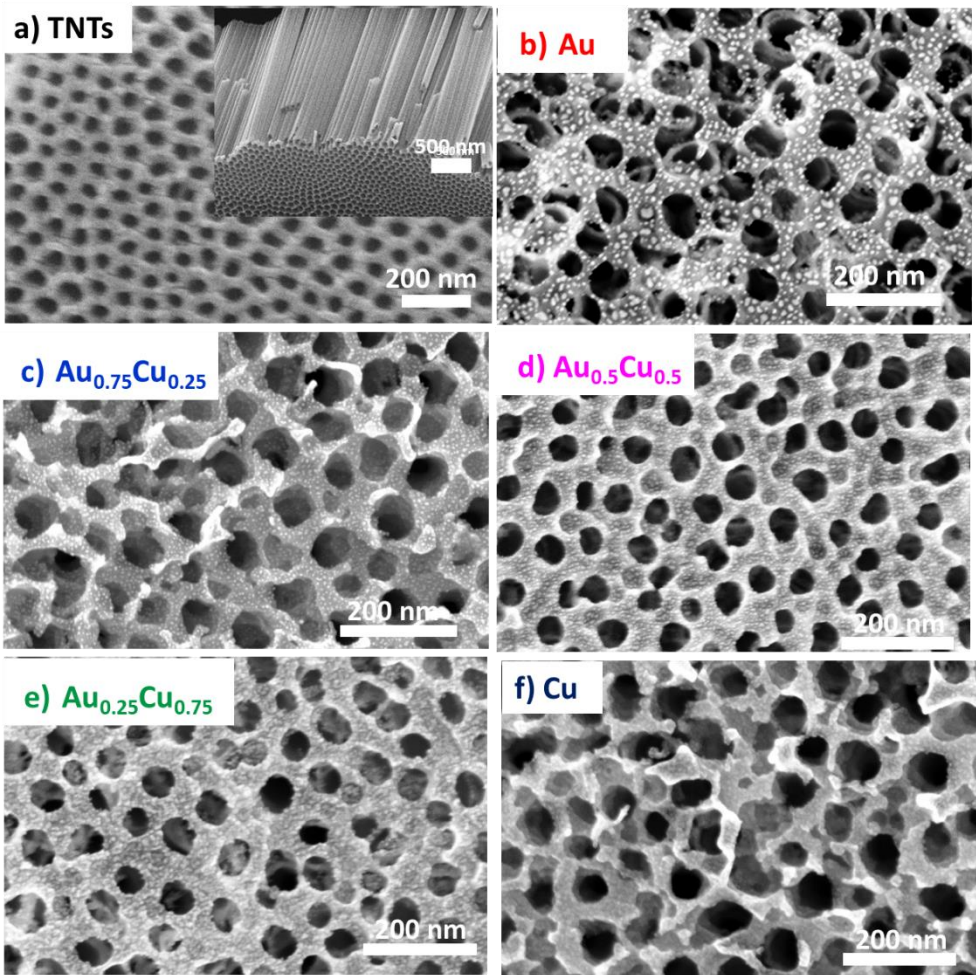
Figure 4.4. SEM images of a) top-view of pristine TNTs with a cross-sectional image in the inset. TNTs covered with 4 ML of b) Au clusters c) $Au_{0.75}Cu_{0.25}$ clusters d) $Au_{0.5}Cu_{0.5}$ clusters e) $Au_{0.25}Cu_{0.75}$ clusters and f) Cu clusters.
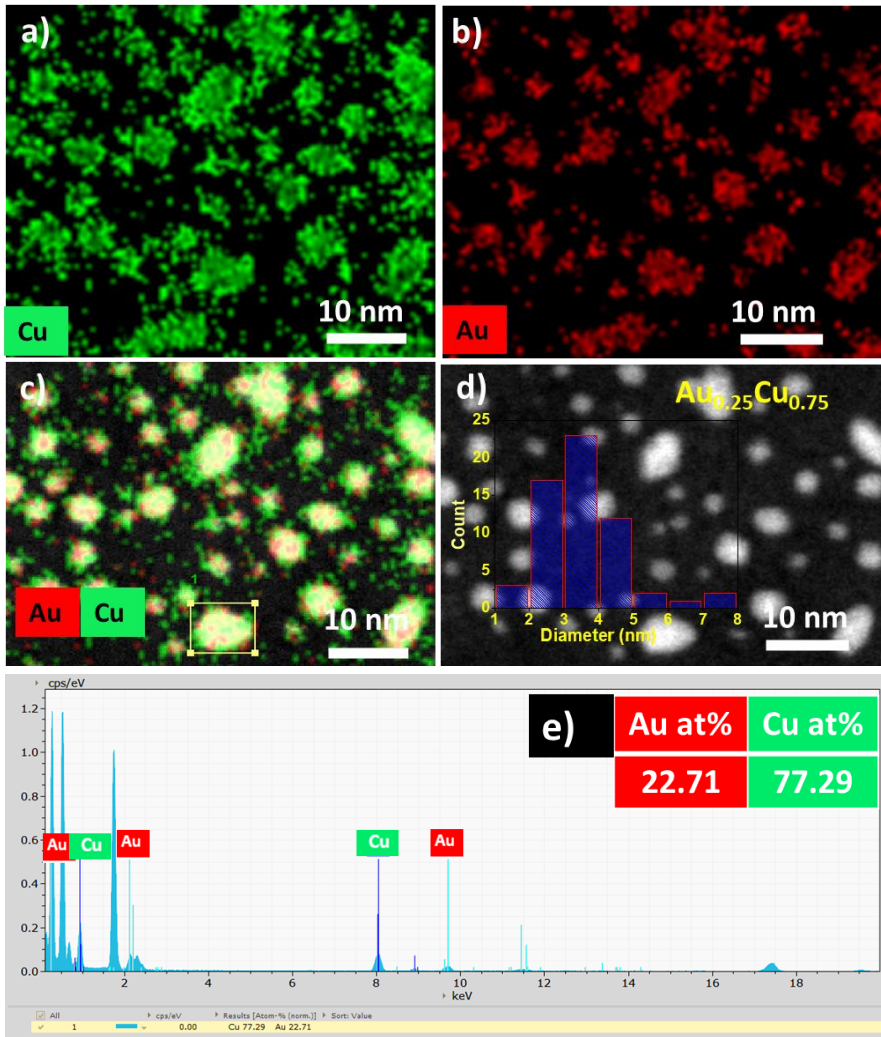
Figure 4.5 (a-d) HAADF-STEM elemental mapping images of $Au_{0.25}Cu_{0.75}$., Cu (green), Au (red) with size distribution of NCs obtained from image analysis software. e) EDX mapping of Au and Cu for 4 atomic monolayer loading of $Au_{0.25}Cu_{0.75}$ NCs on TNTs.

More information about the morphology, size, structure and composition of alloy NCs is provided by HAADF-STEM studies. As shown in the **Figure 4.5,** 0.67 ML of $Au_{0.25}Cu_{0.75}$ NCs deposited on carbon TEM grid show uniform dispersion with Cu grains position on the surface of the cluster with Au at the core **(Figure 4.5c).** The average diameter of clusters is found to be 3.5 ± 0.5 nm **(Figure 4.5d)**. **Figure 4.5e** gives the EDX mapping which provides Au and Cu elemental distributions across the scanned area. It confirmed the composition of an ensemble of NCs that were deposited, *i.e.,* Au = 22.71% and Cu = 77.29%. This shows that BNC composition usually reflects that of the alloy target.[157,158,113] Slightly larger size distribution observed with TEM compared to the mean diameters obtained in the gas phase may be attributed to a less efficient detection of the larger mass clusters by the microchannel plate (MCP) of the ToF-MS particularly under the conditions of relatively low acceleration voltages[350] (in our case it is < 3 kV). Additional flattening of the clusters due to cluster-support interaction after deposition combined with a limited cluster agglomeration on the support may also contribute to this effect.
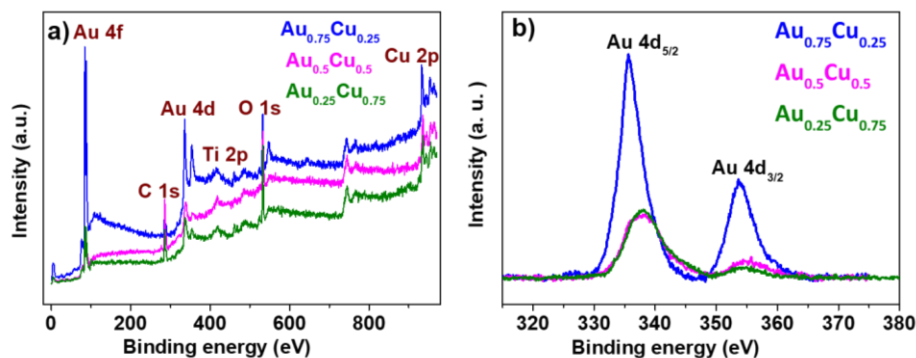
Figure 4.6. XPS a) survey spectra, and b) core level Au-4d spectra recorded for Au_xCu_{1-x} (x = 0.75, 0.5, and 0.25) BNCs on TiO_2.

XPS was performed to get information on the composition and the oxidation states of gold and copper in the Au_xCu_{1-x} (x = 0.75, 0.50, and 0.25) clusters on the TiO_2 (**Figure 4.6**). The survey spectrum (**Figure 4.6a**) shows that O, C, Ti, Au and Cu are present on the surface of all samples. O 1s contribution highlights the oxidation of the Cu phase, while the peak intensity of C 1s is relatively consistent for all the samples despite varying compositions and it appeared at the binding energy value of 285 eV. Au $4f_{7/2}$, Au $4f_{5/2}$ contributions are observed at binding energies of around 84 eV, 88 eV, while the Au $4d_{5/2}$ and

Au-4d$_{3/2}$ core levels (**Figure 4.6a)** are positioned around 334 eV and 355 eV. Upon increasing Cu concentration, a blue shift of the Au 4d$_{5/2}$ BE **(Figure 4.6b)** from 337.8 eV both in Au$_{0.5}$Cu$_{0.5}$ and Au$_{0.25}$Cu$_{0.75}$ relative to that of Au$_{0.75}$Cu$_{0.25}$ at 335.8 eV is observed. The fact that Au 4d BE in Au$_{0.75}$Cu$_{0.25}$ matches that of bulk gold indicates the presence of pure gold or a gold-rich alloy in these nanoalloys. The 2 eV blue shift observed for Au$_{0.5}$Cu$_{0.5}$ and Au$_{0.25}$Cu$_{0.75}$ NCs indicates a d charge depletion at the Au site, highlighting the formation of an alloy as reported in the AuCu system and in a variety of other Au-based intermetallics.[351,352,353,354,254]

The detailed atomic structure of Au$_x$Cu$_{1-x}$ NCs was further characterized by X-ray absorption spectroscopy carried out at edges of both Cu and Au before PEC studies. XANES spectra of Au$_{0.75}$Cu$_{0.25}$ and Au$_{0.5}$Cu$_{0.5}$ NCs measured at the Au L$_3$-edge (mainly 2p to d dipole transitions) **(Figure 4.7a)**, show similar profiles as that of the Au foil reference, indicating that nearly pure gold is present in these two samples. On the other hand, a sharp increase of the white line intensity, probing the unoccupied densities of d states above the Fermi level, is observed in Au$_{0.25}$Cu$_{0.75}$. This indicates that Au atoms lose electrons likely, due to the formation of a AuCu alloy in which a charge transfer from Au to Cu occurs.[355] Similar observations were made for AuAg NCs produced in the same source.[113] This is supported by the positive binding energy shift of the Au 4d peak, observed in the XPS spectra of Au$_{0.5}$Cu$_{0.5}$ and Au$_{0.25}$Cu$_{0.75,}$ relative to that of Au$_{0.75}$Cu$_{0.25}$. The presence of unoccupied d states above the Fermi level in Cu, Ag, and Au alloys, supported by band theory and related calculations,[356,357,358,359] is generally compensated by a gain of mainly s-p charge from Cu.[353] In Au$_{0.5}$Cu$_{0.5}$ a discrepancy is observed between the XPS measured a few days after the synthesis, showing the formation of an alloy, and the XANES measured a few months later, pointing out an Au rich phase. This indicates that for this composition Cu segregates from the alloy upon time in the ambient. Cu K-edge XANES (1s to 3p dipole transitions) **(Figure 4.7b)** profiles indicate the presence of significant amounts of copper oxide in all the AuCu BNCs samples as indicated by the systematic blue shift of the edge position, accompanied by the marked increase in the white line. Au$_{0.5}$Cu$_{0.5}$ contains a large amount of CuO while a complex mixture of Cu metal, Cu$_2$O and CuO is found in Au$_{0.75}$Cu$_{0.25}$ and Au$_{0.25}$Cu$_{0.75}$ **(Figure 4.7b)**.
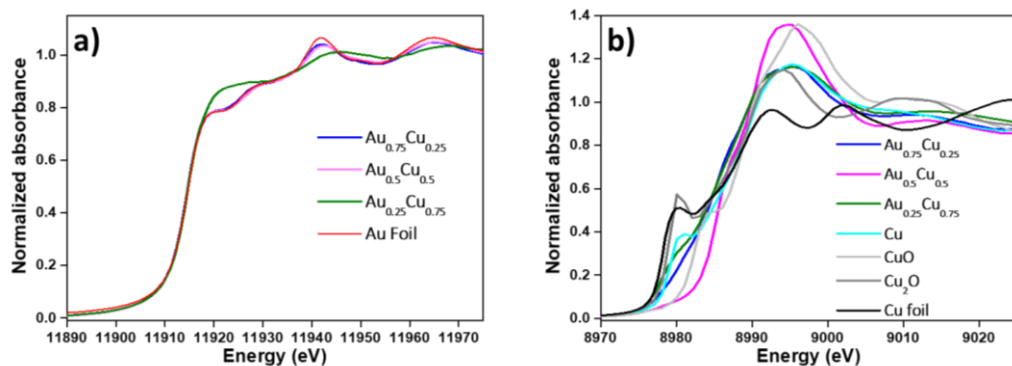
Figure 4.7. XANES spectra of a) Au- L3 edge and b) Cu K-edge.

Extended X-ray Absorption Fine Structure (EXAFS) that does not require long-range order in the material allows for a precise detection of the alloyed structure in the nanostructured Au-Cu bimetallic systems.[242,243] Detailed fitting of the EXAFS data at the Au L_3-edge was carried out with a 2-shell structure model based on Au-Au and Au-Cu, and the values are tabulated in **Table 4.1.** No significant additional shells were present at higher distances. No Au–O interactions could be detected, indicating the fully metallic state of Au in the clusters. Au-Au atomic bond distances sharply decrease with increasing Cu content from 2.85 Å in gold-rich $Au_{0.75}Cu_{0.25}$ over 2.84 Å in $Au_{0.5}Cu_{0.5}$, to 2.82 Å in copper rich $Au_{0.25}Cu_{0.75}$, which is shorter than the bulk value (2.88 Å). Au-Cu bond distances vary from 2.79 Å in $Au_{0.75}Cu_{0.25}$, 2.82 Å in $Au_{0.5}Cu_{0.5}$, down to a remarkable short distance of 2.67 Å in $Au_{0.25}Cu_{0.75}$. These distance differences reflect the variety of local structures and electronic configurations occurring in each composition. In $Au_{0.75}Cu_{0.25}$ and $Au_{0.5}Cu_{0.5}$ the similar Au-Au and Au-Cu distances suggests the formation of a gold-rich random solid solution type of alloy, while in $Au_{0.25}Cu_{0.75}$ the significant discrepancy suggests the formation of an AuCu ordered intermetallic alloy supported by the comparable N_{Au-Au} and N_{Au-Cu} coordination numbers **(Table 4.1).**

Table 4.1. Summary of structural results of Au L_3-edge EXAFS refinements of the Au_xCu_{1-x} clusters.

Sample	$Au_{0.75}Cu_{0.25}$	$Au_{0.5}Cu_{0.5}$	$Au_{0.25}Cu_{0.75}$
Support	TiO_2	TiO_2	TiO_2
E_f (eV)	-8.273	-8.104	-8.120
AFAC	0.800	0.800	0.800
k-range ($A^{°-1}$)	3-11.5	3-11.5	3-11.5
N_{Au1}	9.919	10.287	5.580
$R_{Au1}(A^°)$-	2.851	2.840	2.8158
A_{Au1} (Å^2)	0.01917	0.022	0.02409
N_{Cu2}	0.9896	0.98291	5.5015
R_{Cu2} ($A^°$)	2.789	2.8223	2.66478
A_{Cu2} (Å^2)	0.024	0.02443	0.02375
R (%)	36.61%	36%	30.66%

The structural EXAFS fitting results at the Cu K-edge of bimetallic AuCu and pure Cu clusters is summarized in **Table 4.2**. The first coordination shell consists of 2.25 O at 1.93 Å in pure Cu, 1.7 O at 1.95 Å in $Au_{0.75}Cu_{0.25}$, 2.5 O at 1.97 Å in $Au_{0.5}Cu_{0.5}$, and 1.4 O at 1.96 Å in $Au_{0.25}Cu_{0.75}$. As Cu is four-fold coordinated to O at 1.96 Å in CuO and two-fold coordinated at 1.85 Å, the fraction of copper oxide in each sample, either CuO or Cu_2O, can be calculated using a combination of both coordination numbers and bond distances. Fractions are obtained of 73%, (40% of Cu_2O and 33% of CuO), 45 % (4.5% of Cu_2O and 40.5% of CuO), 62% of CuO and 35% of CuO for Cu, $Au_{0.75}Cu_{0.25}$, $Au_{0.5}Cu_{0.5}$, and $Au_{0.25}Cu_{0.75}$ respectively. The coordination numbers of Cu-Au in

$Au_{0.75}Cu_{0.25}$, $Au_{0.5}Cu_{0.5}$, and $Au_{0.25}Cu_{0.75}$, are 2.53, 2.35, and 3.3, respectively and those of Cu-Cu in $Au_{0.75}Cu_{0.25}$, $Au_{0.5}Cu_{0.5}$, $Au_{0.25}Cu_{0.75}$, and Cu are 2.101, 1.12, 2.1 and 1.702, respectively.

Based on the obtained bond lengths, coordination number, and the fraction of copper oxide, structures can be proposed for all the samples. Those are presented in **Figure 4.8.** All the Cu containing samples have copper oxide at the outer shell, protecting copper metal inside. The pure Cu cluster sample **(Figure 4.8d)** has the highest fraction of oxides, as could be anticipated because Cu is prone to oxidation at ambient conditions. From **Figure 4.8,** $Au_{0.75}Cu_{0.25}$ has higher Au content (70% of $Au_{0.9}Cu_{0.1}$) at the core, covered by 20% $AuCu_3$ alloy followed by 10% copper oxide while, $Au_{0.5}Cu_{0.5}$ has 50% of $Au_{0.9}Cu_{0.1}$ at the core covered by 10% $AuCu_3$ alloy followed by 10% pure copper metal and 31% copper oxide (CuO). $Au_{0.25}Cu_{0.75}$ has 50% of intermetallic $Au_{0.5}Cu_{0.5}$ alloy at the core covered by 15% Au_3Cu alloy followed by 10% pure copper metal and 26% copper oxide (CuO) on the surface. In the case of pure Cu NCs, 73% of the copper is oxidized and it protects the remaining 27% percent of copper metal at the core. The above results suggest that the Au_xCu_{1-x} NCs restructure themselves over time with CuO species dominantly forming on the surface because of oxidative ambient conditions, protecting the metallic nature of formed alloy at the core from further corrosion. This contributes to the stability as well as efficient separation and transfer of charge carriers between TNTs and BNCs which will result in higher PEC activity. Though both $Au_{0.5}Cu_{0.5}$ and $Au_{0.25}Cu_{0.75}$ appear to have similar structures, their cores are different, the first has a random alloy core ($Au_{0.9}Cu_{0.1}$), while the latter has intermetallic alloy ($Au_{0.5}Cu_{0.5}$) core, which may have consequences for the PEC activity.

Table 4.2. Summary of structural results of Cu K-edge EXAFS refinements of the Au_xCu_{1-x} clusters.

Sample	Cu	$Au_{0.75}Cu_{0.25}$	$Au_{0.5}Cu_{0.5}$	$Au_{0.25}Cu_{0.75}$
Support	TiO_2	TiO_2	TiO_2	TiO_2
E_f (eV)	-10.135	0.666	-3.017	0.3920
AFAC	0.85	0.9	0.85	0.85
k-range (A^{-1})	3-10	3.5-11	3-11	3-10
N_{O1}	2.248 (73% Cu_xO of which 40 % of Cu_2O and 33 % CuO)	1.702 (45% of Cu_xO of which 4.5 % of Cu_2O and 40.5% CuO)	2.5122 62% of CuO	1.4 35% of CuO
$R_{O1}(A°)$-	1.933 O	1.951 O	1.97 O	1.96 O
A_{O1} ($Å^2$)	0.0153	0.013	0.01074	0.01
N_{Cu2}	1.702 Cu	2.101	1.122	2.1
R_{Cu2} ($A°$)	2.902 Cu	2.626	2.5183	2.658
A_{Cu2} ($Å^2$)	0.062 Cu	0.038	0.0224	0.022
(N_{Cu3}) N_{Au3}	3.477 Cu	2.523 Au	2.3455 Au	3.3 Au
$(R_{Cu3}$ ($A°$)/R_{Au3} ($A°$)	3.173 Cu	2.737 Au	2.8405 Au	2.843 Au
$(A_{Cu3}$ ($Å^2$)/A_{Au3} ($Å^2$)	0.0474 Cu	0.029 Au	0.03049 Au	0.036 Au
N_{Cu4}	0.9602 Cu	0.852	0.93174	1.0
R_{Cu4} ($A°$)	3.056	2.845	2.91362	2.514
A_{Cu4} ($Å^2$)	0.0122		0.038	0.014
N_{Cu5}	1.04266		1.9299	1.2
R_{Cu5} ($A°$)	2.567		3.137	2.91
A_{Cu5} ($Å^2$)	0.0129		0.03251	0.016
N_{Cu6}			0.86834	
R_{Cu6} ($A°$)			2.6978	
A_{Cu6} ($Å^2$)			0.01358	
R (%)	33.62%	50.41%	37.73%	38.08%

a) $Au_{0.75}Cu_{0.25}$

CuO_x 11%
(CuO-9.9%
Cu_2O-1.1%)

$AuCu_3$ 20%

$Au_{0.9}Cu_{0.1}$
70%

b) $Au_{0.5}Cu_{0.5}$

CuO 35%

Pure Cu metal 3%

$AuCu_3$ 10%

$Au_{0.9}Cu_{0.1}$
50%

c) $Au_{0.25}Cu_{0.75}$

CuO 29%
Cu_2O 13%
Pure Cu metal 8%

Au_3Cu

$Au_{0.5}Cu_{0.5}$
50%

d) Cu

CuO 40%

Cu_2O 33%

Cu metal
27%
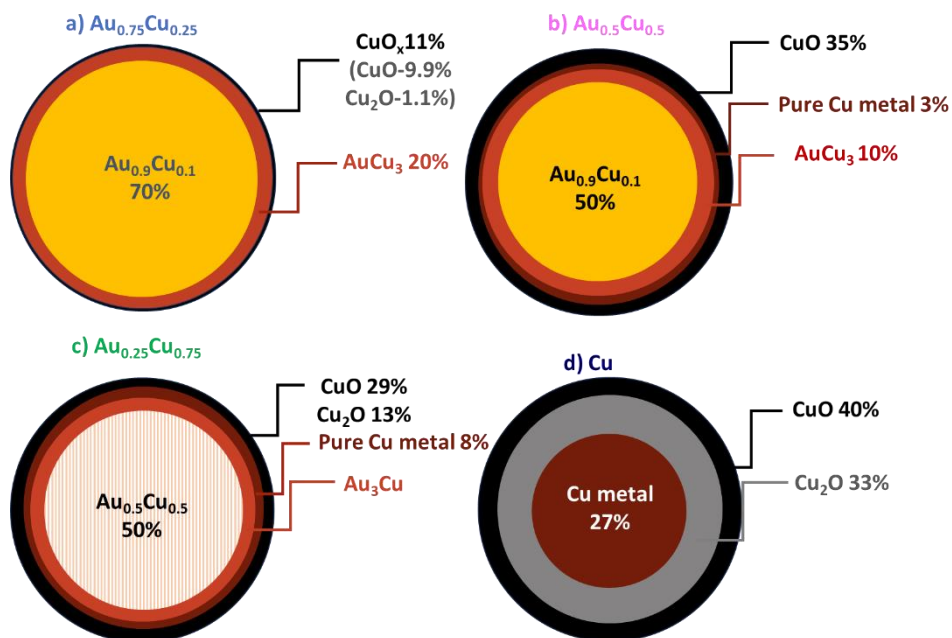
Figure 4.8. Different structures predicted with varying composition from XAFS data analysis.

E_f = Contribution of the wave vector of the zero photoelectron relative to origin of k
$AFAC$ (amplitude reduction due to many-electron processes) was set to 0.8.
K = Photoelectron wavenumber
N = Number of atoms in each shell
R = Distance between neighboring atoms in each shell
A = Debye-Waller term of each shell ($A=2\sigma^2$ with σ = Debye-Waller factor)
$R(\%)$ = Percentage fit - Agreement fraction.

4.3.2 Optical characterization

The UV-Vis absorption spectra (300 - 800 nm) of pristine and Au_xCu_{1-x} (x = 1, 0.75, 0.5, 0.25 and 0) NCs-modified TNTs with 4 ML loading are shown in **Figure 4.9a**. All Au-Cu cluster-modified TNTs samples exhibit a photo-response below 400 nm, which could be attributed to intrinsic band gap of TiO_2. This confirms that the modification of TNTs surface with NCs does not affect the

inherent absorption of TiO_2 in the ultraviolet region. At the wavelengths above 400 nm, the absorption is significantly modified by the presence of the NCs. All cluster-based samples show more intense absorption in the visible range and the absorption maximum shifts to larger wavelengths. For the pure Au NCs, the SPR of gold Au is observed around 530 nm. LSPR intensity of Cu NCs damps quickly and is comparable to TNTs[360] because of its susceptibility to oxidation in air to Cu_2O and CuO.[361,362,363]
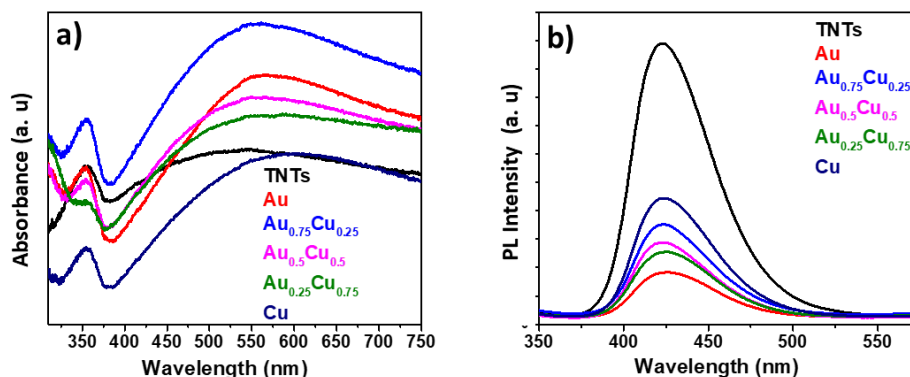
Figure 4.9. a) UV-Vis absorbance spectra of pristine TNTs and Au_xCu_{1-x} (x = 1, 0.75, 0.5, 0.25 and 0) clusters-modified TNTs with a loading of 4 ML. b) Photoluminescence spectra of pristine TNTs and Au_xCu_{1-x} (x = 1, 0.75, 0.5, 0.25 and 0) clusters-modified TNTs at an excitation wavelength of 310 nm.

Although the photo response of TiO_2 is usually exclusively in the ultraviolet region with wavelengths below 390 nm, the pure TNTs studied in this work show a broad and less intense absorption band in the visible light range as well. This can be more likely from the scattering of light caused by the pores or cracks in the nanotubes or the presence of oxygen vacancies and Ti^{3+} species as shown by previous researches.[364,365] Oxygen vacancies and Ti^{3+} species states hundreds of millielectronvolts below the TiO_2 conduction band can be produced during anneal process. Previous studies have also demonstrated that the periodic top-porous layer on the TNTs surface acts as a photonic crystal, facilitating significant optical absorption for TNTs even in the infrared region.[366,367,133] Additionally, the absorption in the visible range may also stem from the reflection or absorption in the underlying Ti metal related to interband d-d transitions.[133] However, incident photon-to-electron conversion efficiency (IPCE) measurements show that no significant photocurrent is generated when

the pristine TNTs are illuminated with purely visible light.[368] Therefore, the absorption above 500 nm in all the samples could arise not only from the distinctive highly periodically porous structure of TNTs, as previously reported[366,367] but also due to LSPR of BNCs active in the visible range.

Photoluminescence (PL) measurements of 4 ML Au_xCu_{1-x} (x = 1, 0.75, 0.5, 0.25 and 0) NCs decorated TNTs have been carried out and the measured spectra at an excitation of 310 nm are presented in the **Figure 4.9b**.

Photoluminescence (PL) is a light emission process observed when a material has absorbed photons.[369] When a material is exposed to light, photons with sufficient energy are absorbed, exciting electrons from their ground state (S_0) to a higher energy level (usually from the valence band to the conduction band in semiconductors). These excited electrons can lose energy through radiative or non-radiative emissions. In non-radiative relaxation, the energy can be lost through interactions with phonons (vibrations within the lattice of the material) typically taking place on timescales between 10^{-14} and 10^{-11} seconds. In radiative emission, excited electrons relax through photon emission. It is a slow process on the order of 10^{-9} to 10^{-7} seconds.[370] In PL spectroscopy, the spectra of those emitted photons is recorded. It is important to note that excited electrons tend to first relax non-radiatively to S_1 and then radiatively from S_1 to S_0. Therefore, photoluminescence spectroscopy only measures the transitions between S_1 to S_0. Radiative and non-radiative emissions are competing processes. Non-radiative processes can occur before photoluminescence if they involve relaxation within excited states, but once an electron is in the lowest excited state S_1, it will either return to the ground state radiatively (photoluminescence) or non-radiatively. PL in semiconductors is the macroscopic manifestation of radiative recombination between photogenerated carriers, occurring in tiny regions (few tenths of nanometers wide, typically) below the semiconductor surface.[371] Moreover, the PL intensity quantifies the recombination efficiency of photogenerated charges, which represents one of the most important limiting factors for photocatalytic efficiency.

It is to be noted from **Figure 4.9b**, that PL occurs in the TNTs as well as samples with clusters. An intense luminescence in the visible range is observed for the pristine TNT. The intense PL for pristine TNTs is indicative of rapid charge carrier recombination. Remarkable, the NCs-modified samples exhibited a much lower PL intensity, which suggests the clusters improve photogenerated charge carrier separation, increase lifetime, and thus reduce recombination of holes

and electrons.[372,133,373] When AuCu NCs are deposited on TNTs, excited electron migration from the semiconductor to the metal occurs until the two Fermi levels are aligned and a Schottky barrier formed at the AuCu/TNTs interface serves as an efficient electron trap, preventing electron-hole recombination.[205] The visible luminescence band is quenched when AuCu NCs are deposited, which indicates that the excited electrons trapped in oxygen vacancies of anatase are transferred to metal NPs. The $Au_{0.25}Cu_{0.75}$ modified TNTs photoanode showed minimal emission intensity after Au-TNTs, followed by other combinations $Au_{0.5}Cu_{0.5} < Au_{0.75}Cu_{0.25<}$ Cu-TNT < Pristine TNTs.

4.3.3. Photoelectrochemical performances

The PEC activity of the prepared pristine and Au_xCu_{1-x} NCs (x = 1, 0.75 ,0.5, 0.25 and 0) modified TNTs electrodes was tested using a standard three electrode PEC cell in 0.5 M Na_2SO_4 electrolyte (at pH 7.21) under AM 1.5G illumination. When the semiconductor's Fermi level aligns with the redox potential of the electrolyte solution in the PEC cell, band bending takes place and an electric field is generated. This field facilitates the movement of photogenerated charges (such as holes from n-type semiconductors) towards the interface between the semiconductor and the electrolyte. At this interface, water can undergo oxidation to produce oxygen when in contact with an n-type semiconductor (acting as a photoanode).

The linear sweep voltammograms of pristine and Au_xCu_{1-x} NCs-modified TNTs shown in the **Figure 4.10a** indicates that upon irradiation, a linear trend in photocurrent density was observed with increase in applied potential in the case of NCs-modified TNTs except gold and pristine TNTs. The photocurrent density of the gold electrode exhibits a linear increase until 0.6 V, after which it stabilizes. Pristine TNTs electrode shows a linear trend up to 0.3 V, followed by a plateau in photocurrent density until 1.2 V, where a sudden spike occurs at this potential. Under the suitable illumination, the TNTs and Au_xCu_{1-x} NCs-modified TNTs electrodes produce photogenerated holes and electron pairs and these photogenerated holes oxidize the water molecules at the anode and the electron reduces the proton into molecular hydrogen at the cathode. The photocurrent density of optimized $Au_{0.25}Cu_{0.75}$ modified TNTs photoanode at 1.23 V vs RHE is 244.2 $\mu A/cm^2$, which is 3.5 folds higher than the pristine TNTs (68.03 $\mu A/cm^2$). This value is significantly greater than the values reported (150

$\mu A/cm^2$ and 64 $\mu A/cm^2$ in the scarce literature available for AuCu NCs on TNTs for PEC applications.[339,340]

Figure 4.10b shows the instant photo response of all prepared electrodes when performing LSV under chopped illumination (alternatingly switching on and off the light source every 5 seconds). **Figure 4.10c** shows the photocurrent density of all the electrodes along with the pristine TNTs based on LSV curves. Chronoamperometric (J-t) measurements at 1.23 V vs RHE, shown in **Figure 4.10d**, show a steady photocurrent for all electrodes. The enhancement in the photocurrent by the NC decoration, particularly upon modification with Au_xCu_{1-x} NCs, is confirmed. The photostability of the best performing $Au_{0.25}Cu_{0.75}$ modified TNTs photoanode was evaluated under the AM 1.5G illumination at the constant applied potential of 1.2 V vs RHE for 1 hour and is presented in the **Figure 4.10e**. It retained its initial activity throughout the test. This shows the good stability of Au_xCu_{1-x} clusters under the applied conditions. After a period of 90 days, the same electrode ($Au_{0.25}Cu_{0.75}$ modified TNTs - 4ML) retained 90% from their initial activity. This further confirms stability of the electrodes over time.
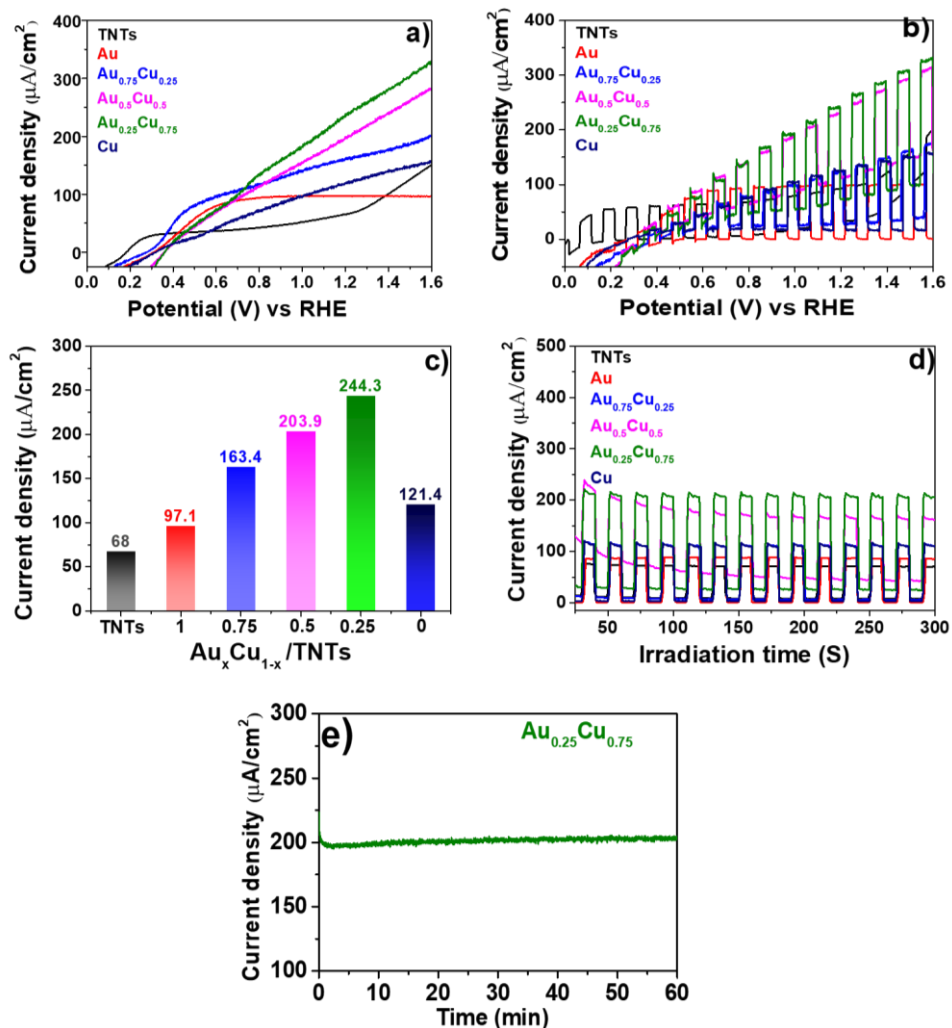
Figure 4.10. a) Linear sweep voltammetry of pristine and Au_xCu_{1-x} NCs-modified TNTs with 4ML loading, tested under AM 1.5G illumination (100 mW cm^{-2}). b) LSV under chopped illumination to check instant photo-response. c) Photocurrent density at 1.23 V vs RHE of the all photoanodes. d) Chronoamperometry at 1.23V vs RHE of pristine and Au_xCu_{1-x} NCs-modified TNTs electrodes. e) Time dependence of the current density of 4 ML $Au_{0.25}Cu_{0.75}$ measured in 0.5M Na_2SO_4 without any scavengers.
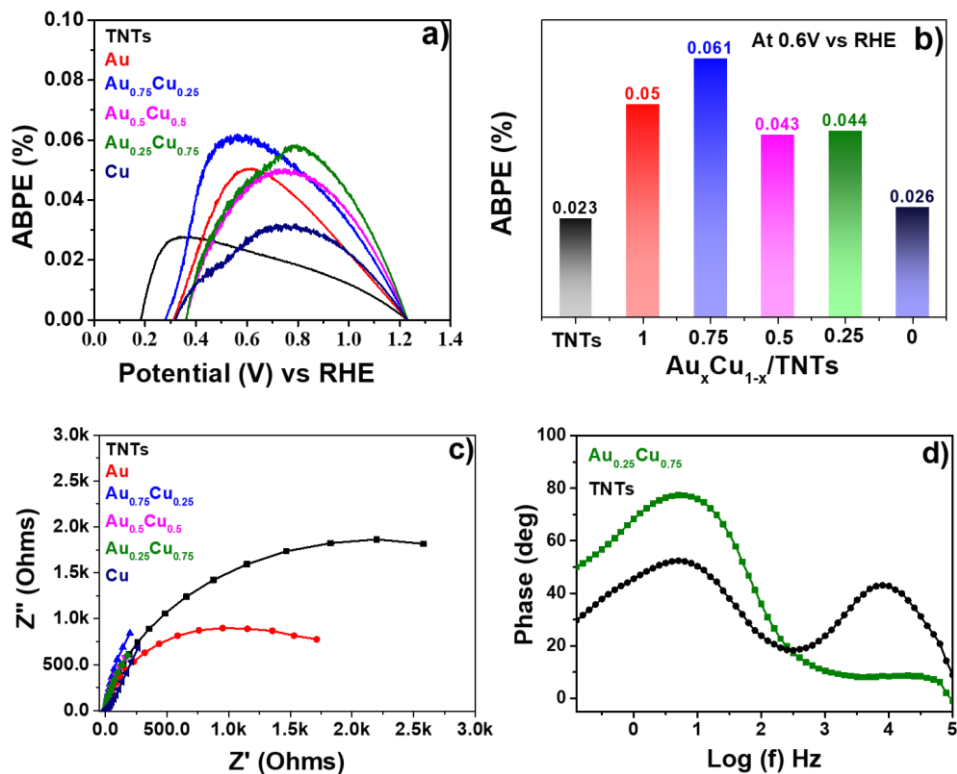
Figure 4.11. a) ABPE (%) plot of all electrodes; b) ABPE (%) values at 0.6 V *vs* RHE under illumination. c) EIS spectra of pristine and $AuCu_{1-x}$ (x= 1, 0.75, 0.5, 0.25 and 0) 4ML NCs modified TNTs electrodes measured under AM 1.5G illumination. d) Bode plot of pristine TNTs and 4 ML $Au_{0.25}Cu_{0.75}$ / TNT samples measured in 0.5M Na_2SO_4 at pH 7.2.

ABPE was calculated using the **equation (4.2)** utilizing values obtained from LSV under illumination and the results are depicted in **Figures 4.11 a& b**. The pristine TNTs electrode exhibits the lowest ABPE (%) of 0.023 at 0.6 V vs RHE, while $Au_{0.75}Cu_{0.25}$ /TNTs demonstrates a maximum ABPE (%) of 0.061 at 0.6 V vs RHE. The ABPE (%) value for $Au_{0.25}Cu_{0.75}$ NCs-modified TNTs is 0.044 at 0.6 V vs RHE, exhibiting a similar trend to the LSV at 0.6 V under illumination condition (**Figure 4.10a**).

The interfacial charge transfer efficiency of the photoelectrodes at the electrode and electrolyte interface was evaluated using electrochemical impedance spectroscopy (EIS) measured in 0.5 M Na_2SO_4 electrolyte at pH 7.2. The Nyquist plot in **Figure 4.11c** shows the results of $AuCu_{1-x}$ (x = 1, 0.75, 0.5, 0.25 and 0) 4ML NCs-modified TNTs and pristine TNTs electrodes measured under AM 1.5G illumination. $Au_{0.25}Cu_{0.75}$ modified TNTs exhibits the smallest circle arc followed successively by $Au_{0.5}Cu_{0.5}$, $Au_{0.75}Cu_{0.25}$, Cu, Au NCs modified TNTs, while the pristine TNTs sample exhibits the largest arc indicative of less interfacial charge transfer. The smaller arc radii in AuCu/TNTs electrodes signify the efficient interfacial charge transfer efficiency and minimal charge transfer resistance at the electrode-electrolyte interface as compared with pristine TNTs. Further using EIS data, the hole relaxation lifetime can be calculated through bode phase analysis presented in **Figure 4.11d.** The accelerated lifetime and minimal hole diffusion length are key factors for a rapid charge transfer process at the interface, resulting in improved water oxidation performance. By using the equation 4.3, the lifetime (τ) of 4 ML $Au_{0.25}Cu_{0.75}$ NCs-modified TNTs is determined and is found to be 2.03 ms, which is shorter than the lifetime of bare TNTs (2.98 ms). Also, the hole diffusion length of 4 ML $Au_{0.25}Cu_{0.75}$ modified TNTs is 101 μm, which is shorter than the bare TNTs (149 μm) calculated using equation 4.4. The values are summarized in **Table 4.3**. The dark current densities cannot be ignored since all the electrodes, except pure gold exhibit certain amount of dark current, probably due to the electrocatalytic performance of copper oxide in all the copper containing electrodes [374,375,376] as shown in the **Figure 4.12.**
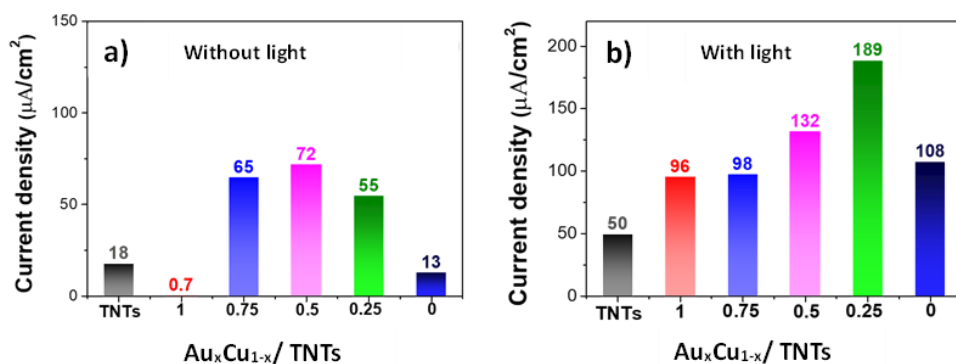
Figure 4.12. Photocurrent densities of all the electrodes both under a) dark and b) purely light conditions deduced by subtracting dark current from the total current observed in LSV.

Table 4.3. Calculated values of relaxation frequency, hole relaxation time and hole diffusion length from bode and EIS plots.

Samples	Relaxation frequency (f_{max}) (Hz)	Hole relaxation time (ms)	Hole diffusion length (µm)
$Au_{0.25}Cu_{0.75}$ / TNTs	78.24	2.03	101
Bare TNTs	53.31	2.98	149

4.4. Discussion

The pure Au/TNTs electrode, with its strong plasmonic properties **(Figure 4.9a)** and lowest recombination of charge carriers exhibited by the lower intensity of its PL emission spectrum **(Figure 4.9b)**, features a 40% increase of PEC activity compared to pristine TNTs **(Figure 4.10c).** This electrode gave negligible dark current, indicating that almost 100% (97%) of the activity depends on the modification with the plasmonic clusters. But the electrode suffers from a high charge transfer resistance at the electrode-electrolyte interface as observed by EIS measurements **(Figure 4.11c).** On the other hand, the pure Cu/TNTs electrode features a remarkable increase in photoactivity of nearly 80% compared to pristine TNTs, despite a significant Cu oxidation in the ambient reducing the metallic part to 27% of the cluster atoms. Small dark current of 13 µA/cm^2 occurs from the 2 eV band gap of the 33% Cu_2O oxide layer, while 89% activity (108 µA/cm^2) is coming purely from light **(Figure 4.12).** However, the copper cluster sample suffers from a poor stability and a higher recombination rate than the other electrodes (PL measurements, **Figure 4.9b)**.

Upon alloying, all the Au_xCu_{1-x} electrodes exhibit higher photocurrent densities than their monometallic counterparts as well as pristine TNTs, with values of 163.43 µA/cm^2, 203.86 µA/cm^2, and 244.28 µA/cm^2 for x = 0.75, 0.5, and 0.25, respectively **(Figure 4.10c)**. This clearly illustrates a synergy between both metals in bimetallic AuCu NCs, [377,378,379] which enhances the photoactivity. A composition-dependent PEC activity peaking at $Au_{0.25}Cu_{0.75}$ clearly **(Figure 4.10c)** suggests that the composition does play a crucial role in tuning the PEC activity. Quenching of luminescence, which is indicative of a decrease in charge recombination, with increasing copper content in the alloy electrodes as observed by PL measurements **(Figure 4.9b)** further supports the composition dependency. The clusters have composition dependent structures, as derived

on the basis of the XAFS measurements **(Figure 4.8)**. In particular, it is suggested that the Au_xCu_{1-x} NCs restructure themselves over time on the surface of TNTs with copper oxide at the outer shell protecting the metallic nature of formed alloy at the core from further corrosion. Finally, the smaller arc radii of Au_xCu_{1-x}/TNTs electrodes as compared with pristine TNTs in EIS measurements **(Figure 4.11c)** signify the efficient interfacial charge transfer efficiency and minimal charge transfer resistance at the electrode-electrolyte interface of NCs-modified TNTs contributing to higher PEC activity than pristine TNTs.

The $Au_{0.75}Cu_{0.25}$/TNTs demonstrates the highest ABPE (0.061%) of all the bimetallic electrodes at 0.6 V vs RHE but shows a 68 % increase in photoactivity compared to pure gold. It is to be noted that ABPE measured in this study is lower than the ABPE efficiency 0.033% of Au/Ag BNPs synthesized via solid-state thermal dewetting on ZnO semiconductor at 0.3 V vs RHE[380] and 2.131 % at the bias of 0.89 V vs RHE for Au-Pd decorated TiO_2 nanorods.[381] A reliable comparison is, however, not possible because of limited literature on AuCu on TNTs and the ABPE is measured at different applied biases and under different synthesis conditions in different studies. On the other hand $Au_{0.75}Cu_{0.25}$/TNTs shows a higher recombination of charge carriers compared its pure Au counterpart as observed by higher photoluminescence intensity **(Figure 4.9b),** but lower charge transfer resistances **(Figure 4.11c)**. This $Au_{0.75}Cu_{0.25}$/TNTs sample has clusters with a large gold-rich alloy core (around 70%) surrounded by a thin layer of CuO. It features a higher plasmon intensity due to the larger size of the metallic core in comparison with the other alloy electrodes. As $Au_{0.75}Cu_{0.25}$ differs mostly from pure Au by the thin CuO layer (10%) surrounding the clusters **(Figure 4.8b),** the presence of CuO may explain the higher activity. $Au_{0.75}Cu_{0.25}$ exhibits a dark current of 65 $\mu A/cm^2$, while 60% (of total current obtained through LSV) activity coming purely from light (98 $\mu A/cm^2$) **(Figure 4.12).**

$Au_{0.5}Cu_{0.5}$/TNTs demonstrates a 25% increase in activity compared to $Au_{0.75}Cu_{0.25}$ at 1.23 V vs RHE. $Au_{0.5}Cu_{0.5}$ consists of a gold rich random alloy at the core (50%) **(Figure 4.8b)** and only differs from the Au rich composition by the presence of a larger amount of 31% CuO_x on the surface of the clusters. This structural arrangement is expected to further reduce the plasmon intensity as the metallic core size decreases. On the other hand, it shows a lower recombination of charge carriers as observed by lower intensity of photoluminescence **(Figure 4.9b)** and lower charge transfer resistances from EIS

measurements **(Figure 4.11c).** The presence of a higher amount (31%) of CuO may be at the origin of the activity increase.

$Au_{0.25}Cu_{0.75}$ exhibits the highest PEC activity of all tested electrodes with a 20 % increase compared to $Au_{0.5}Cu_{0.5}$ and more than twice the activities of pure metals **(Figure 4.10c).** The main structural difference with $Au_{0.5}Cu_{0.5}$ lies in the presence of an intermetallic $Au_{0.5}Cu_{0.5}$ alloyed structure in the core of the cluster instead of a gold-rich random alloy in the two other compositions.

The highest activity of $Au_{0.25}Cu_{0.75}$ is influenced by a combination of many possible factors. Firstly, in this alloy, the presence of a significantly higher amount of Cu than in the other bimetallic materials ordered the original structure with two different Au-Au and Au-Cu distances as shown in the EXAFS analysis, corresponding to higher charge transfer highlighted in the XANES. Secondly, different electronic properties of intermetallic compounds also contribute to the higher activity of $Au_{0.25}Cu_{0.75}$. It is found that intermetallic compounds show larger hot carrier generation, originating mainly from direct interband and phonon-assisted indirect electronic transitions. The resulting hot carriers are energetically higher than that in their monometallic counterparts. The resulting hot carriers have longer relaxation times and mean free path and thus become efficient LSPR materials absorbing light strongly as shown in literature.[382,383] Compared to pure copper the addition of a minority of Au changes dramatically the properties of the clusters by creating a large metallic core accounting for 50% of the cluster atoms featuring a significant larger plasmonic intensity than pure copper where the metallic core represent only (27%).[384] Thirdly, formation of a metal-metal oxide interface in an Au-Cu bimetal system under oxidative conditions, shows significantly enhanced catalytic performance due to the formation of CuO_x/Au interfacial[385] sites, which may further explain the high activity of $Au_{0.25}Cu_{0.75}$. Fourthly, the superior performance can also be driven by reduced recombination of charge carriers as indicated by the lowest PL intensity of all tested electrodes besides Au **(Figure 4.9b),** implying the generated charge carriers are efficiently separated by $Au_{0.25}Cu_{0.75}$ NCs acting as electron sinks and are therefore easily available for redox reactions. Fifth, the highest interfacial charge transfer efficiency is evidenced by the EIS results **(Figure 4.11c)**; This is supported by lower charge transfer resistance, shorter hole relaxation time, and hole diffusion length, as compared to pristine TNTs (**Table 4.3)** leading to more efficacious charge migration and separation facilitating water oxidation to boost the resultant PEC performance. Sixth, the sample contains an optimal metal loading which allows

the TNTs photocatalyst to harvest sunlight effectively and generate more charge carriers while samples with higher loading, 6 ML and 8 ML, exhibited lower photocurrent density as shown in **Figure 4.13**. The higher loading of AuCu species, though increase the number of trapping sites with the formation of Schottky barrier at the interface, may reduce the area of the TNTs surface exposed to light and can act as recombination centers of photogenerated electron-hole pairs.[386]
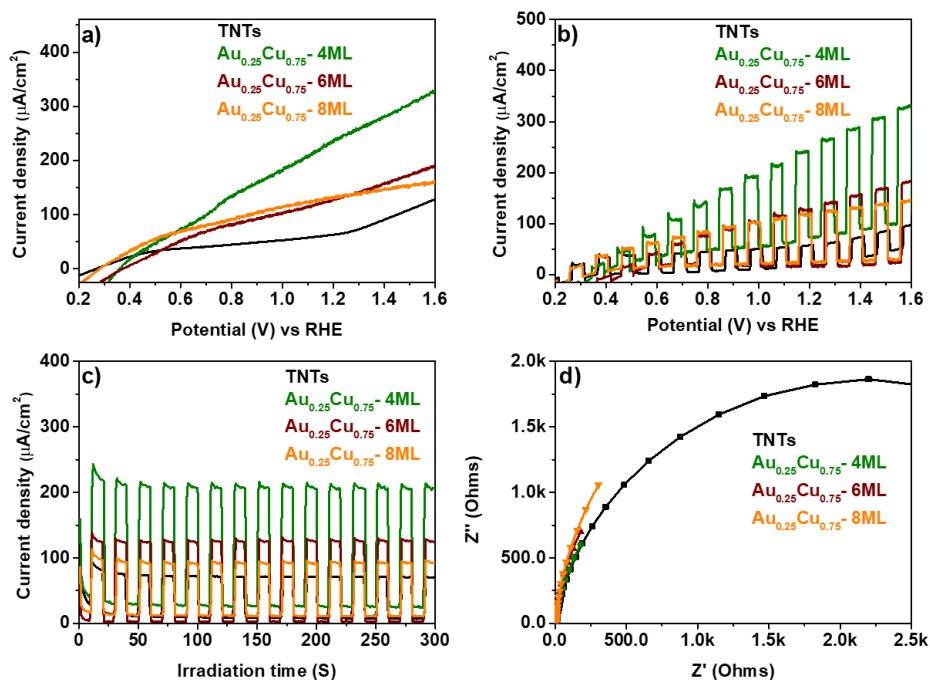
Figure 4.13. a) LSV of $Au_{0.25}Cu_{0.75}$ clusters modified titania nanotubes with loadings of 4 ML, 6 ML and 8 ML and pristine TNTs electrodes tested under solar illumination (100 mW cm^{-2}). b) LSV under chopped illumination (alternating on and off every 5 s). c) Chronoamperometry of $Au_{0.25}Cu_{0.75}$ clusters modified TNTs electrodes at 1.2 V vs RHE in Na_2SO_4 electrolyte at pH 7.2 with solar illumination. d) Electrochemical impedance spectroscopy (EIS) of $Au_{0.25}Cu_{0.75}$ clusters modified TNTs electrodes under solar illumination.

4.5. Conclusion

In summary, well-dispersed, ligand free, size and composition tuneable Au_xCu_{1-x} (x = 1, 0.75, 0.5, 0.25 and 0) NCs were synthesized and deposited, by the CBD method, on TNTs. It was observed that surface modification of TNTs with Au_xCu_{1-x} NCs leads to enhanced PEC activity under solar irradiation peaking for the $Au_{0.25}Cu_{0.75}$ NC composition, which showed a four-fold enhancement in photocurrent compared to pristine TNTs. This enhancement is attributed to a combination of factors such as the unique tubular morphology of TiO_2, atomic restructuring of the electrode over the time forming a thin protective copper oxide layer on the surface, and the intermetallic alloy at the core contributing to charge redistribution between Au and Cu which improves the stability. Reduced recombination of charge carriers as indicated by the lowest PL intensity, and the highest interfacial charge transfer efficiency as evidenced by the impedance spectroscopy, contribute to the superior performance of this sample. Finally, the potential of the CBD technique that produces ligand-free NCs of tuneable size and composition with a high degree of purity and high uniformity, serves as an ideal platform technology to investigate cluster properties and at the same time design efficient cluster-based photocatalysts for PEC water oxidation.

Chapter 5

General conclusions and Outlook

5.1. General conclusions

The main objective of this PhD thesis can be summarized as:

"To design and characterize new and high-performance TiO_2 photocatalysts modified by AuM (M = Ag, Cu) bimetallic nanoclusters that can be used for self-cleaning surfaces and water oxidation.

The aforementioned objective was achieved through fabrication of well-defined, composition- and size-controlled AuAg and AuCu alloy BNCs and depositing them on titania nanoparticles and nanotubes. The required amount of NCs, predominantly with a loading of 4 ML, was subsequently deposited on TiO_2-based substrates for photocatalytic (self-cleaning) and PEC (photocurrent generation) applications. Prior to applications, samples were subjected to diverse characterization methods and techniques to know their size, composition, oxidation state, and structure and their influence in boosting photocatalytic and PEC activity.

In **chapter 1,** the research was situated within the broad context of the environmental and energy challenges confronting our world today, emphasizing the significance of conducting this research, i.e., for the creation of a more sustainable world. The chapter continued with an overview of TiO_2-based photocatalysis, plasmonic photocatalysis, and PEC reactions, supported by examples from literature. AuAg and AuCu NCs synthesized through the CBD technique were introduced as potential effective and high-performing cocatalysts with n-type semiconductor TiO_2. The limitations of traditional TiO_2 photocatalysis were commented on as well as those of wet chemical methods for the synthesis of NCs. Finally, this chapter concludes highlighting the main objective of thesis.

Chapter 2 introduced the experimental methods and characterization techniques employed in this thesis, supported by examples from the research.

119

The CBD technique for nanocluster synthesis and deposition as well as the characterization techniques served as foundations for the research, facilitating the understanding of properties, and their role as cocatalysts in photocatalytic and PEC applications.

Chapters 3 and 4 contain the main research results of the thesis. Chapter 3 demonstrated that AuAg NCs-modified TiO_2 are efficient cocatalysts for self-cleaning surfaces, while in chapter 4 the efficiency of AuCu NCs on TNT as photoanodes for PEC activity is discussed.

In chapter 3 the photocatalytic self-cleaning activity of 4 ML Au_xAg_{1-x} (x = 1, 0.9, 0.7, 0.5, 0.3, and 0) BNCs modified TiO_2 powder films were tested under UV and visible light as self-cleaning surfaces. The degradation of stearic acid, a model compound for organic fouling, was probed with infrared absorption spectroscopy. A cluster composition dependent photodegradation activity was found, with the $Au_{0.3}Ag_{0.7}$ composition showing the most effective stearic acid degradation. Structural characterization of Au and $Au_{0.7}Ag_{0.3}$ BNCs deposited on carbon TEM grids revealed that the clusters were uniformly distributed over the surface and were crystalline. The atomic structure of the Au_xAg_{1-x} BNCs deposited on TiO_2 and carbon supports with a 4 ML loading was further characterized by XAFS and while XPS provided the information about the elemental composition, chemical state, and electronic structure of the surface of a material. A charge redistribution between Ag and Au atoms was observed. The effect of this charge redistribution is likely stabilizing the Ag against oxidation, which may directly affect the catalytic properties of the clusters. Furthermore, electromagnetic simulations were performed to understand the mechanism behind photocatalytic activity and to investigate the dependence of the LSPR position and the degree of near-field enhancement on the cluster composition. The highest photoactivity of 4 ML loaded $Au_{0.3}Ag_{0.7}$ nanocluster modified TiO_2 under solar light resulted from the combination of the four possible contributing factors namely, the LSPR effect of the BNCs in the visible light wavelength range, a quantitative overlap of LSPR wavelength of $Au_{0.3}Ag_{0.7}$ composition with the sun's irradiance spectrum and a strong near-field enhancement in this wavelength range that has significant intensity as well as sufficient individual photon energy, the low and optimal total metal loading (4 ML) which still leaves enough TiO_2 surface available for UV light absorption and finally charge distribution between Au and Ag. This study demonstrated CBD as

120

an efficient approach for fabricating well-defined, tunable AuAg plasmon-based photocatalysts for self-cleaning applications, outperforming their counterparts obtained through colloidal methods.

In **chapter 4,** TNTs with its unique morphology, modified with a series of 4 ML Au_xCu_{1-x} (x = 1, 0.75, 0.50, 0.25, and 0) BNCs synthesized through CBD technique proved to be promising photocatalyst for photo-oxidation of water. The morphology of as prepared electrodes, investigated through SEM and TEM, confirmed the size, while the composition of BNCs was confirmed by EDX mapping. Structural changes with composition and electronic environment were derived from EXAFS and XANES, revealed charge redistribution between Au and Cu and the formation of a stable intermetallic alloy at the core of best performing $Au_{0.25}Cu_{0.75}$ photocatalyst. Oxidation of as-prepared electrodes over the time resulted in structural modification with Cu_xO at the outer shell functioning as a protective layer. UV-Vis confirmed that the cluster modification extended the absorption range of the TNTs to the visible region, while PL measurements demonstrate that they reduce the high charge carrier recombination rate of pure TNTs. The as-prepared electrodes were tested photoelectrochemically for the generation of anodic photocurrent using AM 1.5G solar simulator. It was found that Au_xCu_{1-x} (x = 1, 0.75, 0.5, 0.25 and 0) NC modification remarkably enhances the anodic photocurrent relative to that of pristine TNTs.

In summary, the potential of using the CBD technique as a tool for gaining fundamental knowledge and designing photo(electro)catalysts made of BNCs on TiO_2 supports is highlighted in this PhD. The CBD technique offers precise control over particle size and composition, enabling a detailed understanding of their properties and the structure-activity relationship. The decoration of TiO_2 surfaces with BNCs has resulted in significant improvements in light absorption, charge separation, and photocatalytic activity. Specifically, AuAg BNCs on TiO_2 have proven highly effective as photocatalysts for self-cleaning surfaces. The synergistic effects between the BNCs and TiO_2 enhance the degradation of organic pollutants like stearic acid under visible light irradiation. Additionally, AuCu BNCs on TNTs have demonstrated superior performance as photoanodes, requiring minimal material to facilitate efficient and stable hydrogen generation from water. These materials are thus effective in both self-cleaning applications and water splitting, showcasing their potential

to significantly contribute to sustainable energy solutions and environmental remediation technologies.

5.2. Suggestions for further research

The universe is full of surprises. It never stops catching our attention with its extraordinary and complex systems from the microscopic to the macroscopic world. The more we explore this universe, the more we realize how little we know. This is the driving force for me to know more by extending my research.

The first proposal for further study is to use the obtained knowledge about the AuAg and AuCu BNCs, to explore their potential for CO_2 photoreduction. Ag and Au as co-catalysts are known to exhibit a good selectivity for CO_2 reduction to CO,[387] and Cu is known to produce a range of C1 and C2+ hydrocarbons and alcohols.[388,389,390] Photocatalytic CO_2 reduction is an active research area in view of the alarming rise of CO_2 emission levels in the atmosphere, already exceeding 400 ppm, destabilizing the climate by increasing global warming.[391] Therefore, there is an urgent need to mitigate excess of CO_2 emission in the atmosphere by converting it into high energy fuels that may replace fossil fuels. AuCu and AuAg nanostructures synthesized through CBD technique together with n-type semiconductor TiO_2, in combination with abundant solar energy, can significantly improve the CO_2 photoreduction performance. This research could be further be extended towards other plasmonic nanostructures like Pt, Pd and Ni in combination with Au, Ag and Cu since AgPd, AuAg, CuPt, AuCu, and AuPt nanoalloys generally exhibit better activity and selectivity for CO_2 photoreduction than their monometallic counterparts.[392,393,336] For instance, a marked 80% methane selectivity is observed for AgPt co-catalysts on TiO_2 as compared to 20% over pure TiO_2.[394] A remarkable field enhancement has been observed at the metal interface in AuAg and AuPt bimetallic NPs[395,396] and in AuNi NPs,[397] hot electrons from Au enhance the CO_2 catalytic conversion occurring at Ni sites. Designing highly performant plasmonic photocatalysts for CO_2 reduction can be done by carefully tuning the BNPs' size, shape, and composition. Both the LSPR wavelength and the band width depend on the size of the plasmonic NP.[70,398,399] Shape influences the intensity of the LSPR (near field enhancement which is due to LSPR, is extremely intense at tips, edges and sharp corners of anisotropic plasmonic NPS

(e.g. nanorods, -triangles or -cubes).[400,70,401] Also the metal-support interaction plays a significant role in the photocatalytic activity.[402] The role of these parameters can be carefully and systematically tuned to obtain promising outcome.

Secondly, since CBD technique is found to be promising in producing well-dispersed, ligand free, size and composition controlled, tunable mono and bimetallic coinage metal NCs that are excellent photocatalysts compared to the equivalent ones prepared chemically, it can provide a new direction for designing novel photocatalysts in the future. I would like to move from mono and bimetallic AuAg and AuCu NC synthesis to trimetallic or multi-metallic NCs in combination with less expensive metals like Ni, Fe with suitable semiconductors to study their ability for manifold applications such as exhaust pollutants removal, self-cleaning surface efficiency enhancement as well as for splitting water to oxygen and hydrogen.

Finally, this thesis used only TiO_2- based substrates (P25 and nanotubes) for AuAg and AuCu nanocluster deposition for photocatalytic and PEC applications. A new semiconductor-based materials other than TiO_2, with a wide range of light absorption, appropriate redox potentials, and high stability for efficient photocatalysis can be utilized. Literature study mentions that bismuth-based layered perovskite oxyhalides, specially bismuth vanadate $(BiVO_4)$[403] owing to unique crystal structure, intensive visible light absorption, suitable band structure, and superior stability, provides a highly promising alternative for traditional metal oxide photocatalysts for various applications ranging from water splitting to pollutant removal.[404] With a bandgap of 2.4 - 2.5 eV and enhanced thermodynamic solar to hydrogen conversion efficiency (i.e., ~ 9.1%)[405] $BiVO_4$ is among the most promising ternary metal oxide photoanode.[406] Therefore, developing highly efficient and stable photocatalysts with Bi-based substrates, modified with metal NCs such as AuAg, AuCu, AgCu and AuNi clusters is an option to experiment with.

Hence, by employing the CBD technique for cluster synthesis in combination with appropriate substrates, it becomes feasible to develop novel and efficient photocatalysts suitable for both catalyst studies and industrial applications.

References

1 THE 17 GOALS | Sustainable Development, https://sdgs.un.org/goals, (accessed March 10, 2024).

2 U. Nations, Causes and Effects of Climate Change, https://www.un.org/en/climatechange/science/causes-effects-climate-change, (accessed March 28, 2024).

3 I. Yüksel, *Renew. Sustain. Energy Rev.*, 2010, **14**, 462–469.

4 E. Barbier, *Renew. Sustain. Energy Rev.*, 2002, **6**, 3–65.

5 A. Pareek, R. Dom, J. Gupta, J. Chandran, V. Adepu and P. H. Borse, *Mater. Sci. Energy Technol.*, 2020, **3**, 319–327.

6 A. Fujishima and K. Honda, *Nature*, 1972, **238**, 37–38.

7 B. O'Regan and M. Grätzel, *Nature*, 1991, **353**, 737–740.

8 P. Lianos, *Appl. Catal. B Environ.*, 2017, **210**, 235–254.

9 S. Boutillier, S. Fourmentin and B. Laperche, *Environ. Chem. Lett.*, 2022, **20**, 1017–1033.

10 K. Hashimoto, H. Irie and A. Fujishima, *Jpn. J. Appl. Phys.*, 2005, **44**, 8269.

11 K. Nakata and A. Fujishima, *J. Photochem. Photobiol. C Photochem. Rev.*, 2012, **13**, 169–189.

12 B. Ohtani, *Phys. Chem. Chem. Phys.*, 2014, **16**, 1788–1797.

13 S. G. Kumar and K. S. R. K. Rao, *Appl. Surf. Sci.*, 2017, **391**, 124–148.

14 D. M. Tobaldi, L. Lajaunie, M. López Haro, R. A. S. Ferreira, M. Leoni, M. P. Seabra, J. J. Calvino, L. D. Carlos and J. A. Labrincha, *ACS Appl. Energy Mater.*, 2019, **2**, 3237–3252.

15 M. R. Hoffmann, S. T. Martin, W. Choi and D. W. Bahnemann, *Chem. Rev.*, 1995, **95**, 69–96.

16 Z. Zhu, Z. Lu, D. Wang, X. Tang, Y. Yan, W. Shi, Y. Wang, N. Gao, X. Yao and H. Dong, *Appl. Catal. B Environ.*, 2016, **182**, 115–122.

17 J. Luo, S. Zhang, M. Sun, L. Yang, S. Luo and J. C. Crittenden, *ACS Nano*, 2019, **13**, 9811–9840.

18 J. C. S. Wu, T.-H. Wu, T. Chu, H. Huang and D. Tsai, *Top. Catal.*, 2008, **47**, 131–136.

19 O. Carp, C. L. Huisman and A. Reller, *Prog. Solid State Chem.*, 2004, **32**, 33–177.

20 D. T. Cromer and K. Herrington, *J. Am. Chem. Soc.*, 1955, **77**, 4708–4709.

21 R. Marchand, L. Brohan and M. Tournoux, *Mater. Res. Bull.*, 1980, **15**, 1129–1133.

22 L. Liu, H. Zhao, J. M. Andino and Y. Li, *ACS Catal.*, 2012, **2**, 1817–1828.

23 T. Luttrell, S. Halpegamage, J. Tao, A. Kramer, E. Sutter and M. Batzill, *Sci. Rep.*, 2014, **4**, 4043.

24 X. Wang, Z. Li, J. Shi and Y. Yu, *Chem. Rev.*, 2014, **114**, 9346–9384.

25 N. Serpone, *J. Photochem. Photobiol. Chem.*, 1997, **104**, 1–12.

26 A. Fujishima, X. Zhang and D. A. Tryk, *Surf. Sci. Rep.*, 2008, **63**, 515–582.

27 What is standard hydrogen electrode?, https://www.toppr.com/ask/question/what-is-standard-hydrogen-electrode/, (accessed June 13, 2024).

28 A. Fujishima, T. N. Rao and D. A. Tryk, *J. Photochem. Photobiol. C Photochem. Rev.*, 2000, **1**, 1–21.

29 V. Etacheri, C. Di Valentin, J. Schneider, D. Bahnemann and S. C. Pillai, *J. Photochem. Photobiol. C Photochem. Rev.*, 2015, **25**, 1–29.

30 M. Pelaez, N. T. Nolan, S. C. Pillai, M. K. Seery, P. Falaras, A. G. Kontos, P. S. M. Dunlop, J. W. J. Hamilton, J. A. Byrne, K. O'Shea, M. H. Entezari and D. D. Dionysiou, *Appl. Catal. B Environ.*, 2012, **125**, 331–349.

31 H.-S. Son, S.-J. Lee, I.-H. Cho and K.-D. Zoh, *Chemosphere*, 2004, **57**, 309–317.

32 P. Wang, B. Huang, Y. Dai and M.-H. Whangbo, *Phys. Chem. Chem. Phys.*, 2012, **14**, 9813–9825.

33 C. Ampelli, C. Genovese, G. Centi, R. Passalacqua and S. Perathoner, *Top. Catal.*, 2016, **59**, 757–771.

34 S. Perathoner, G. Centi and D. Su, *ChemSusChem*, 2016, **9**, 345–357.

35 P. K. Jain, X. Huang, I. H. El-Sayed and M. A. El-Sayed, *Acc. Chem. Res.*, 2008, **41**, 1578–1586.

36 null Payal and P. Pandey, *Recent Pat. Nanotechnol.*, 2022, **16**, 45–66.

37 I. D. Ibrahim, E. R. Sadiku, T. Jamiru, Y. Hamam, Y. Alayli and A. A. Eze, *J. King Saud Univ. - Sci.*, 2020, **32**, 758–764.

38 W.-T. Liu, *J. Biosci. Bioeng.*, 2006, **102**, 1–7.

39 A. Aghababai Beni and H. Jabbari, *Results Eng.*, 2022, **15**, 100467.

40 V. Amendola, R. Pilot, M. Frasconi, O. M. Maragò and M. A. Iatì, *J. Phys. Condens. Matter Inst. Phys. J.*, 2017, **29**, 203002.

41 D. Cheng, R. Liu and K. Hu, *Front. Chem.*, , DOI:10.3389/fchem.2022.958626.

42 J. R. Morones, J. L. Elechiguerra, A. Camacho, K. Holt, J. B. Kouri, J. T. Ramírez and M. J. Yacaman, *Nanotechnology*, 2005, **16**, 2346–2353.

43 Y. Yu, Z. Zhou, G. Huang, H. Cheng, L. Han, S. Zhao, Y. Chen and F. Meng, *Water Res.*, 2022, **222**, 118901.

44 Z. Hai, N. E. Kolli, D. B. Uribe, P. Beaunier, M. José-Yacaman, J. Vigneron, A. Etcheberry, S. Sorgues, C. Colbeau-Justin, J. Chen and H. Remita, *J. Mater. Chem. Mater. Energy Sustain.*, 2013, **1**, 10829–10835.

45 H. Tian, X. L. Zhang, J. Scott, C. Ng and R. Amal, *J Mater Chem A*, 2014, **2**, 6432–6438.

46 G. Binnig and H. Rohrer, *Rev. Mod. Phys.*, 1987, **59**, 615–625.

47 M. Knoll and E. Ruska, *Z. Für Phys.*, 1932, **78**, 318–339.

48 B. Sperry, N. Kukhta, Y. Huang and C. Luscombe, *Chem. Mater.*, , DOI:10.1021/acs.chemmater.2c03006.

49 A. Heuer-Jungemann, N. Feliu, I. Bakaimi, M. Hamaly, A. Alkilany, I. Chakraborty, A. Masood, M. F. Casula, A. Kostopoulou, E. Oh, K. Susumu, M. H. Stewart, I. L. Medintz, E. Stratakis, W. J. Parak and A. G. Kanaras, *Chem. Rev.*, 2019, **119**, 4819–4880.

50 E. M. Modan and A. G. Plăiaşu, *Ann. "Dunarea Jos" Univ. Galati Fascicle IX Metall. Mater. Sci.*, 2020, **43**, 53–60.

51 X. Gan, D. Lei, R. Ye, H. Zhao and K.-Y. Wong, *Nano Res.*, , DOI:10.1007/s12274-020-2955-x.

52 S. Linic, P. Christopher and D. B. Ingram, *Nat. Mater.*, 2011, **10**, 911–921.

53 J. J. Chen, J. C. S. Wu, P. C. Wu and D. P. Tsai, *J. Phys. Chem. C*, 2011, **115**, 210–216.

54 N. Zhang, S. Liu and Y.-J. Xu, *Nanoscale*, 2012, **4**, 2227–2238.

55 X. Zhang, Y. L. Chen, R.-S. Liu and D. P. Tsai, *Rep. Prog. Phys.*, 2013, **76**, 046401.

56 J. R. Lombardi and R. L. Birke, *J. Phys. Chem. C*, 2008, **112**, 5605–5617.

57 P. V. Kamat, *J. Phys. Chem. B*, 2002, **106**, 7729–7744.

58 V. Subramanian, E. Wolf and P. V. Kamat, *J. Phys. Chem. B*, 2001, **105**, 11439–11446.

59 V. Subramanian, E. E. Wolf and P. V. Kamat, *J. Am. Chem. Soc.*, 2004, **126**, 4943–4950.

60 S. Bai, X. Li, Q. Kong, R. Long, C. Wang, J. Jiang and Y. Xiong, *Adv. Mater.*, 2015, **27**, 3444–3452.

61 P. Christopher, H. Xin and S. Linic, *Nat. Chem.*, 2011, **3**, 467–472.

62 P. Christopher, D. B. Ingram and S. Linic, *J. Phys. Chem. C*.

63 P. Christopher, D. Ingram and S. Linic, *J. Phys. Chem. C - J PHYS CHEM C*, , DOI:10.1021/jp101633u.

64 S. A. Maier, *Plasmonics: fundamentals and applications*, Springer, New York, NY, Repr., 2007.

65 R. Schasfoort and A. Tudos, *Handbook Of Surface Plasmon Resonance*, 2007.

66 V. Rai, A. Srivastava, C. Mukherjee and S. Deb, .

67 D. T. Hue, T. T. Thu Huong, P. T. Thu Ha, T. T. Trang, N. T. Ha Lien and V. Xuan Hoa, *AIP Adv.*, 2021, **11**, 055319.

68 P. K. Jain, K. S. Lee, I. H. El-Sayed and M. A. El-Sayed, *J. Phys. Chem. B*, 2006, **110**, 7238–7248.

69 J. J. Mock, M. Barbic, D. R. Smith, D. A. Schultz and S. Schultz, *J. Chem. Phys.*, 2002, **116**, 6755–6759.

70 K. L. Kelly, E. Coronado, L. L. Zhao and G. C. Schatz, *J. Phys. Chem. B*, 2003, **107**, 668–677.

71 C. Langhammer, Z. Yuan, I. Zorić and B. Kasemo, *Nano Lett.*, 2006, **6**, 833–838.

72 I. Thomann, B. A. Pinaud, Z. Chen, B. M. Clemens, T. F. Jaramillo and M. L. Brongersma, *Nano Lett.*, 2011, **11**, 3440–3446.

73 S. Mubeen, G. Hernandez-Sosa, D. Moses, J. Lee and M. Moskovits, *Nano Lett.*, 2011, **11**, 5548–5552.

74 C. Clavero, *Nat. Photonics*, 2014, **8**, 95–103.

75 X.-C. Ma, Y. Dai, L. Yu and B.-B. Huang, *Light Sci. Appl.*, 2016, **5**, e16017–e16017.

76 A. Manjavacas, J. G. Liu, V. Kulkarni and P. Nordlander, *ACS Nano*, 2014, **8**, 7630–7638.

77 N. Szydlo and R. Poirier, *J. Appl. Phys.*, 1980, **51**, 3310–3312.

78 M. Moskovits, *Science*, 2011, **332**, 676–677.

79 Becquerel, *Comptes Rendus L´Academie Sci.*, 1839, **9**, 145–149.

80 C. Du, X. Yang, M. T. Mayer, H. Hoyt, J. Xie, G. McMahon, G. Bischoping and D. Wang, *Angew. Chem. Int. Ed.*, 2013, **52**, 12692–12695.

81 J.-W. Jang, C. Du, Y. Ye, Y. Lin, X. Yao, J. Thorne, E. Liu, G. McMahon, J. Zhu, A. Javey, J. Guo and D. Wang, *Nat. Commun.*, 2015, **6**, 7447.

82 J. Brillet, J.-H. Yum, M. Cornuz, T. Hisatomi, R. Solarska, J. Augustynski, M. Graetzel and K. Sivula, *Nat. Photonics*, 2012, **6**, 824.

83 B. D. Alexander, P. J. Kulesza, I. Rutkowska, R. Solarska and J. Augustynski, *J. Mater. Chem.*, 2008, **18**, 2298–2303.

84 M. A., M. J., M. Ashokkumar and P. Arunachalam, *Appl. Catal. Gen.*, 2018, **555**, 47–74.

85 Y. Cho, M. Park, J. K. Kim, S. Kim, H. Suk Jung and J. H. Park, *Appl. Surf. Sci.*, 2020, **505**, 144569.

86 F. Barbir, *Energy*, 2009, **34**, 308–312.

87 M. Piz and E. Filipek, *Ceram. Int.*, 2021, **47**, 12327–12333.

88 J. Zhang, A. Bifulco, P. Amato, C. Imparato and K. Qi, *J. Colloid Interface Sci.*, 2023, **638**, 193–219.

89 J. Zhang, Y. Zhao, K. Zhang, A. Zada and K. Qi, *Ultrason. Sonochem.*, 2023, **94**, 106325.

90 S. Shen, J. Chen, M. Wang, X. Sheng, X. Chen, X. Feng and S. S. Mao, *Prog. Mater. Sci.*, 2018, **98**, 299–385.

91 X. Chen and S. S. Mao, *Chem. Rev.*, 2007, **107**, 2891–2959.

92 K. Lee, A. Mazare and P. Schmuki, *Chem. Rev.*, 2014, **114**, 9385–9454.

93 C. Murugan, K. B. Bhojanaa, W.-J. Ong, K. Jothivenkatachalam and A. Pandikumar, *Int. J. Hydrog. Energy*, 2019, **44**, 30885–30898.

94 H. M. Chen, C. K. Chen, C.-J. Chen, L.-C. Cheng, P. C. Wu, B. H. Cheng, Y. Z. Ho, M. L. Tseng, Y.-Y. Hsu, T.-S. Chan, J.-F. Lee, R.-S. Liu and D. P. Tsai, *ACS Nano*, 2012, **6**, 7362–7372.

95 G. K. Mor, K. Shankar, M. Paulose, O. K. Varghese and C. A. Grimes, *Nano Lett.*, 2005, **5**, 191–195.

96 O. K. Varghese and C. A. Grimes, *Sol. Energy Mater. Sol. Cells*, 2008, **92**, 374–384.

97 C. Ampelli, F. Tavella, S. Perathoner and G. Centi, *Chem. Eng. J.*, 2017, **320**, 352–362.

98 Q.-L. Mo, X.-C. Dai and F.-X. Xiao, *Small*, 2023, **19**, 2302372.

99 R. Wang, K. Hashimoto, A. Fujishima, M. Chikuni, E. Kojima, A. Kitamura, M. Shimohigoshi and T. Watanabe, *Nature*, 1997, **388**, 431–432.

100 N. Sakai, A. Fujishima, T. Watanabe and K. Hashimoto, *J. Phys. Chem. B*, 2001, **105**, 3023–3026.

101 A. Fujishima, T. N. Rao and D. A. Tryk, *J. Photochem. Photobiol. C Photochem. Rev.*, 2000, **1**, 1–21.

102 R. Wang, N. Sakai, A. Fujishima, T. Watanabe and K. Hashimoto, *J. Phys. Chem. B*, 1999, **103**, 2188–2194.

103 M. Alvaro, B. Cojocaru, A. A. Ismail, N. Petrea, B. Ferrer, F. A. Harraz, V. I. Parvulescu and H. Garcia, *Appl. Catal. B Environ.*, 2010, **99**, 191–197.

104 Riegle Report - Lethal Nerve Agent GD, https://web.archive.org/web/20130912230529/http://www.gulfweb.org/bigdoc/report/appgd.html, (accessed June 10, 2024).

105 D. M. Fouad and M. B. Mohamed, *J. Nanomater.*, 2012, **2012**, 1–8.

106 Y. Cao, H. Tan, T. Shi, T. Tang and J. Li, *J. Chem. Technol. Biotechnol.*, 2008, **83**, 546–552.

107 K. Sytwu, M. Vadai and J. A. Dionne, *Adv. Phys. X*, 2019, **4**, 1619480.

108 E. A. Redina and O. A. Kirichenko, *Catalysts*, 2024, **14**, 68.

109 A. K. Singh and Q. Xu, *ChemCatChem*, 2013, **5**, 652–676.

110 N. Berahim, W. J. Basirun, B. F. Leo and M. R. Johan, *Catalysts*, 2018, **8**, 412.

111 E. A. Redina, G. I. Kapustin, O. P. Tkachenko, A. A. Greish and L. M. Kustov, *Catal. Sci. Technol.*, 2021, **11**, 5881–5897.

112 S. Hu, F. Che, B. Khorasani, M. Jeon, C. W. Yoon, J.-S. McEwen, L. Scudiero and S. Ha, *Appl. Catal. B Environ.*, 2019, **254**, 685–692.

113 V. C. Chinnabathini, F. Dingenen, R. Borah, I. Abbas, J. van der Tol, Z. Zarkua, F. D'Acapito, T. H. T. Nguyen, P. Lievens, D. Grandjean, S. W. Verbruggen and E. Janssens, *Nanoscale*, 2023, **15**, 6696–6708.

114 N. Toshima, *Pure Appl. Chem.*, 2013, **85**, 437–451.

115 O. S. G. P. Soares, M. F. R. Pereira, J. J. M. Órfão, J. L. Faria and C. G. Silva, *Chem. Eng. J.*, 2014, **251**, 123–130.

116 A. Devard, V. S. Aghemo, C. A. Caballero Dorantes, M. Gutierrez Arzaluz, F. A. Marchesini and M. A. Ulla, *React. Kinet. Mech. Catal.*, 2017, **120**, 39–54.

117 A. Zielińska-Jurek and J. Hupka, *Catal. Today*, 2014, **230**, 181–187.

118 S. W. Verbruggen, M. Keulemans, B. Goris, N. Blommaerts, S. Bals, J. A. Martens and S. Lenaerts, *Appl. Catal. B Environ.*, 2016, **188**, 147–153.

119 F. Dingenen, N. Blommaerts, M. Van Hal, R. Borah, D. Arenas-Esteban, S. Lenaerts, S. Bals and S. W. Verbruggen, *Nanomaterials*, 2021, **11**, 2624.

120 Air Mass | PVEducation, https://www.pveducation.org/pvcdrom/properties-of-sunlight/air-mass, (accessed March 29, 2024).

121 S. Abela, C. Farrugia, R. Xuereb, F. Lia, E. Zammit, A. Rizzo, P. Refalo and M. Grech, *Nanomaterials*, 2021, **11**, 2823.

122 S. Asadi, B. Mortezagholi, A. Hadizadeh, V. Borisov, M. J. Ansari, H. Shaker Majdi, A. Nishonova, H. Adelnia, B. Farasati Far and C. Chaiyasut, *Pharmaceutics*, 2022, **14**, 1359.

123 M. Yamaguchi, H. Abe, T. Ma, D. Tadaki, A. Hirano-Iwata, H. Kanetaka, Y. Watanabe and M. Niwano, *Langmuir*, 2020, **36**, 12668–12677.

124 Ł. Haryński, J. Karczewski, J. Ryl, K. Grochowska and K. Siuzdak, *J. Alloys Compd.*, 2021, **877**, 160316.

125 S. A. Batool, M. Salman Maqbool, M. A. Javed, A. Niaz and M. A. U. Rehman, *Surfaces*, 2022, **5**, 456–480.

126 J. Gong, Y. Lai and C. Lin, *Electrochimica Acta*, 2010, **55**, 4776–4782.

127 Q. Li and J. K. Shang, *Environ. Sci. Technol.*, 2009, **43**, 8923–8929.

128 J. Talat-Mehrabad, M. Khosravi, N. Modirshahla and M. A. Behnajady, *Res. Chem. Intermed.*, 2016, **42**, 595–609.

129 W. M. A. El Rouby and A. A. Farghali, *J. Photochem. Photobiol. Chem.*, 2018, **364**, 740–749.

130 F. Xu, D. Bai, J. Mei, D. Wu, Z. Gao, K. Jiang and B. Liu, *J. Alloys Compd.*, 2016, **688**, 914–920.

131 H. Zhang, G. Wang, D. Chen, X. Lv and J. Li, *Chem. Mater.*, 2008, **20**, 6543–6549.

132 K. K. M., B. K., N. G., S. B. and V. A., *Appl. Catal. B Environ.*, 2016, **199**, 282–291.

133 F.-X. Xiao, S.-F. Hung, J. Miao, H.-Y. Wang, H. Yang and B. Liu, *Small*, 2015, **11**, 554–567.

134 M. M. Momeni, Y. Ghayeb and Z. Ghonchegi, *Ceram. Int.*, 2015, **41**, 8735–8741.

135 M. G. Hosseini and M. M. Momeni, *Appl. Catal. Gen.*, 2012, **427–428**, 35–42.

136 K. A. Soliman, A. F. Zedan, A. Khalifa, H. A. El-Sayed, A. S. Aljaber, S. Y. AlQaradawi and N. K. Allam, *Sci. Rep.*, 2017, **7**, 1913.

137 M. M. Momeni, Y. Ghayeb and F. Ezati, *J. Colloid Interface Sci.*, 2018, **514**, 70–82.

138 T. Sharifi, Y. Ghayeb, T. Mohammadi and M. M. Momeni, *Dalton Trans.*, 2018, **47**, 11593–11604.

139 J. Liu and F. Chen, *Int. J. Electrochem. Sci.*, 2012, **7**, 9560–9572.

140 J. A. De Toro, P. S. Normile and C. Binns, in *Gas-Phase Synthesis of Nanoparticles*, John Wiley & Sons, Ltd, 2017, pp. 39–55.

141 O. F. Hagena and W. Obert, *J. Chem. Phys.*, 1972, **56**, 1793–1802.

142 R. W. Siegel, *Annu. Rev. Mater. Res.*, 1991, **21**, 559–578.

143 S. L. Girshick, C.-P. Chiu, R. Muno, C. Y. Wu, L. Yang, S. K. Singh and P. H. McMurry, *J. Aerosol Sci.*, 1993, **24**, 367–382.

144 S. E. Pratsinis, *Prog. Energy Combust. Sci.*, 1998, **24**, 197–219.

145 K. Sattler, J. Mühlbach and E. Recknagel, *Phys. Rev. Lett.*, 1980, **45**, 821–824.

146 T. G. Dietz, M. A. Duncan, D. E. Powers and R. E. Smalley, *J. Chem. Phys.*, 1981, **74**, 6511–6512.

147 W. A. de Heer, *Rev. Mod. Phys.*, 1993, **65**, 611–676.

148 M. A. Duncan, *Rev. Sci. Instrum.*, 2012, **83**, 041101.

149 S. Maruyama, L. R. Anderson and R. E. Smalley, *Rev. Sci. Instrum.*, 1990, **61**, 3686–3693.

150 P. Milani and W. A. deHeer, *Rev. Sci. Instrum.*, 1990, **61**, 1835–1838.

151 J. Theerthagiri, K. Karuppasamy, S. J. Lee, R. Shwetharani, H.-S. Kim, S. K. K. Pasha, M. Ashokkumar and M. Y. Choi, *Light Sci. Appl.*, 2022, **11**, 250.

152 V. E. Bondybey, I. Fischer and R. Schlachta, *Proc. Indian Acad. Sci.*, 1991, **103**, 313–323.

153 A. N. Dobrynin, D. N. Ievlev, G. Verschoren, J. Swerts, M. J. Van Bael, K. Temst, P. Lievens, E. Piscopiello, G. Van Tendeloo, S. Q. Zhou and A. Vantomme, *Phys. Rev. B*, 2006, **73**, 104421.

154 G. Verschoren, A. N. Dobrynin, K. Temst, R. E. Silverans, C. Van Haesendonck, P. Lievens, B. Pipeleers, S. Q. Zhou, A. Vantomme and W. Bras, *Thin Solid Films*, 2008, **516**, 8232–8239.

155 Z. Li, H.-Y. T. Chen, K. Schouteden, T. Picot, K. Houben, T.-W. Liao, C. Van Haesendonck, G. Pacchioni, P. Lievens and E. Janssens, *Nano Lett.*, 2016, **16**, 3063–3070.

156 P. Ferrari, J. Vanbuel, Y. Li, T.-W. Liao, E. Janssens and P. Lievens, in *Gas-Phase Synthesis of Nanoparticles*, John Wiley & Sons, Ltd, 2017, pp. 59–78.

157 B. Pauwels, G. Van Tendeloo, E. Zhurkin, M. Hou, G. Verschoren, L. Theil Kuhn, W. Bouwen and P. Lievens, *Phys. Rev. B*, 2001, **63**, 165406.

158 P. Milani and S. Iannotta, *Cluster Beam Synthesis of Nanostructured Materials*, Springer Science & Business Media, 2012.

159 T.-W. Liao, A. Yadav, K.-J. Hu, J. van der Tol, S. Cosentino, F. D'Acapito, R. E. Palmer, C. Lenardi, R. Ferrando, D. Grandjean and P. Lievens, *Nanoscale*, 2018, **10**, 6684–6694.

160 B. A. Mamyrin, *Int. J. Mass Spectrom. Ion Process.*, 1994, **131**, 1–19.

161 *How do Electron Microscopes Work? 📔 🔬 📔 Taking Pictures of Atoms*, .

162 R. F. Klie, *Physics*, 2009, **2**, 85.

163 SEM Resolution | Scanning Electron Microscopy - BE, https://www.thermofisher.com/uk/en/home/materials-science/learning-center/applications/sem-resolution.html, (accessed March 13, 2024).

164 Sample Preparation | 4 SEM Sample Preparation Techniques, https://vaccoat.com/blog/sample-preparation-for-sem/, (accessed March 21, 2024).

165 J. F. Moulder, *Handbook of X-ray Photoelectron Spectroscopy: A Reference Book of Standard Spectra for Identification and Interpretation of XPS Data*, Physical Electronics, 1995.

166 H. R. Verma, *Atomic and nuclear analytical methods: XRF, Mössbauer, XPS, NAA and ion-beam spectroscopic techniques*, Springer, Berlin ; New York, 2007.

167 A. Goel, Photoelectric effect | Radiology Reference Article | Radiopaedia.org, https://radiopaedia.org/articles/photoelectric-effect, (accessed March 13, 2024).

168 X-Ray Photoelectron Spectroscopy | XPS X-Ray Sources - BE, https://www.thermofisher.com/uk/en/home/materials-science/learning-center/surface-analysis/x-ray-generation.html, (accessed April 6, 2024).

169 XPS Instrumentation, http://www.casaxps.com/help_manual/XPSInformation/XPSInstr.htm, (accessed March 13, 2024).

170 J. Torrent and V. Barrón, in *Methods of Soil Analysis Part 5—Mineralogical Methods*, John Wiley & Sons, Ltd, 2008, pp. 367–385.

171 P. Morozzi, B. Ballarin, S. Arcozzi, E. Brattich, F. Lucarelli, S. Nava, P. J. Gómez-Cascales, J. A. G. Orza and L. Tositti, *Atmos. Environ.*, 2021, **252**, 118297.

172 *Principle and Operation of Shimadzu ISR 2600 Plus Integrating Sphere Accessory*, .

173 Modern Techniques in Applied Molecular Spectroscopy | Wiley, https://www.wiley.com/en-us/Modern+Techniques+in+Applied+Molecular+Spectroscopy-p-9780471123590, (accessed April 6, 2024).

174 Relative Diffuse Reflectance Measurement, https://www.ssi.shimadzu.com/products/uv-vis/uv-vis-nir-spectroscopy-consumables/relative-diffuse-reflectance-measurement/index.html, (accessed December 9, 2023).

175 M. Newville, *Rev. Mineral. Geochem.*, 2014, **78**, 33–74.

176 J. Penner-Hahn, *Compr. Coord. Chem. II*, 2004, **2**, 159–186.

177 A. A. Hummer and A. Rompel, *Adv. Protein Chem. Struct. Biol.*, 2013, **93**, 257–305.

178 Production and characterization of novel catalysts based on bimetallic deposited clusters - KU Leuven, https://kuleuven.limo.libis.be/discovery/fulldisplay/lirias2333290/32KUL_KUL:Lirias, (accessed November 9, 2023).

179 *Handbook on Synchrotron Radiation by G.V. Marr - Ebook | Everand*, .

180 exafs, https://www2.ung.si/~arcon/xas/exafs/exafs.htm, (accessed December 11, 2023).

181 Extended X-ray absorption fine structure (EXAFS) - Online Dictionary of Crystallography, https://dictionary.iucr.org/Extended_X-ray_absorption_fine_structure_(EXAFS), (accessed December 8, 2023).

182 Y. Paz, Z. Luo, L. Rabenberg and A. Heller, *J. Mater. Res.*, 1995, **10**, 2842–2848.

183 R. Fretwell and P. Douglas, *J. Photochem. Photobiol. Chem.*, 2001, **143**, 229–240.

184 Y. Paz and A. Heller, *J. Mater. Res.*, 1997, **12**, 2759–2766.

185 T. Minabe, D. A. Tryk, P. Sawunyama, Y. Kikuchi, K. Hashimoto and A. Fujishima, *J. Photochem. Photobiol. Chem.*, 2000, **137**, 53–62.

186 A. Mills, A. Lepre, N. Elliott, S. Bhopal, I. P. Parkin and S. A. O'Neill, *J. Photochem. Photobiol. Chem.*, 2003, **160**, 213–224.

187 M. N. Ghazzal, N. Barthen and N. Chaoui, *Appl. Catal. B Environ.*, 2011, **103**, 85–90.

188 14.4, https://chem.libretexts.org/Bookshelves/General_Chemistry/Map%3A_General_Chemistry_(Petrucci_et_al.)/14%3A_Chemical_Kinetics/14.04%3A_Zero-Order_Reactions, (accessed June 13, 2024).

189 A. Mills and J. Wang, *J. Photochem. Photobiol. Chem.*, 2006, **182**, 181–186.

190 Y. Paz, Z. Luo, L. Rabenberg and A. Heller, *J. Mater. Res.*, 1995, **10**, 2842–2848.

191 X. Shi, L. Cai, M. Ma, X. Zheng and J. H. Park, *ChemSusChem*, 2015, **8**, 3192–3203.

192 Z. Chen, H. N. Dinh and E. Miller, *Photoelectrochemical Water Splitting: Standards, Experimental Methods, and Protocols*, Springer New York, New York, NY, 2013.

193 H. H. Mohamed, in *Sustainable Materials and Green Processing for Energy Conversion*, eds. K. Y. Cheong and A. Apblett, Elsevier, 2022, pp. 169–212.

194 T. M. Nahir, R. A. Clark and E. F. Bowden, *Anal. Chem.*, 1994, **66**, 2595–2598.

195 D. A. Skoog, F. J. Holler and S. R. Crouch, *Principles of Instrumental Analysis*, Cengage Learning, 2017.

196 S. Kumar, S. Ahirwar and A. K. Satpati, *RSC Adv.*, **9**, 41368–41382.

197 D. Luo, Q. Chen, Y. Qiu, B. Liu and M. Zhang, *Materials*, 2019, **12**, 1713.

198 A. J. Bard, L. R. Faulkner and H. S. White, *Electrochemical Methods: Fundamentals and Applications*, John Wiley & Sons, 2022.

199 Chronoamperometry Purpose, https://www.gamry.com/Framework%20Help/HTML5%20-%20Tripane%20-%20Audience%20A/Content/PE/Experimental_Techniques/Chronoamperometry/Purpose.htm, (accessed June 14, 2024).

200 K. Trzciński, M. Szkoda, K. Siuzdak, M. Sawczak and A. Lisowska-Oleksiak, *Electrochimica Acta*, 2016, **222**, 421–428.

201 B.-Y. Chang and S.-M. Park, *Annu. Rev. Anal. Chem.*, 2010, **3**, 207–229.

202 Interpreting Electrochemical Impedance Spectroscopy Measurements, https://resources.pcb.cadence.com/blog/2020-interpreting-electrochemical-impedance-spectroscopy-measurements, (accessed June 12, 2024).

203 Basics of EIS: Electrochemical Research-Impedance Gamry Instruments, https://www.gamry.com/application-notes/EIS/basics-of-electrochemical-impedance-spectroscopy/, (accessed June 13, 2024).

204 X. Liu, Q. Zhang, J. Li, N. Valanoor, X. Tang and G. Cao, *Sci. Rep.*, 2018, **8**, 17389.

205 A. L. Linsebigler, G. Lu and J. T. Jr. Yates, *Chem. Rev.*, 1995, **95**, 735–758.

206 Pilkington Activ™ Range, https://www.pilkington.com/en-gb/uk/products/product-categories/self-cleaning/pilkington-activ-range, (accessed January 27, 2024).

207 N. Sakai, A. Fujishima, T. Watanabe and K. Hashimoto, *J. Phys. Chem. B*, 2003, **107**, 1028–1035.

208 R. Wang, N. Sakai, A. Fujishima, T. Watanabe and K. Hashimoto, *J. Phys. Chem. B*, 1999, **103**, 2188–2194.

209 A. Fujishima and X. Zhang, *Comptes Rendus Chim.*, 2006, **9**, 750–760.

210 A. Zielińska-Jurek, E. Kowalska, J. W. Sobczak, W. Lisowski, B. Ohtani and A. Zaleska, *Appl. Catal. B Environ.*, 2011, **101**, 504–514.

211 T. Pakizeh, C. Langhammer, I. Zorić, P. Apell and M. Käll, *Nano Lett.*, 2009, **9**, 882–886.

212 S. Linic, P. Christopher and D. B. Ingram, *Nat. Mater.*, 2011, **10**, 911–921.

213 A. E. Schlather, A. Manjavacas, A. Lauchner, V. S. Marangoni, C. J. DeSantis, P. Nordlander and N. J. Halas, *J. Phys. Chem. Lett.*, 2017, **8**, 2060–2067.

214 Y. Zhang, S. He, W. Guo, Y. Hu, J. Huang, J. R. Mulcahy and W. D. Wei, *Chem. Rev.*, 2018, **118**, 2927–2954.

215 S. Wang, Y. Gao, S. Miao, T. Liu, L. Mu, R. Li, F. Fan and C. Li, *J. Am. Chem. Soc.*, 2017, **139**, 11771–11778.

216 S. Mukherjee, F. Libisch, N. Large, O. Neumann, L. V. Brown, J. Cheng, J. B. Lassiter, E. A. Carter, P. Nordlander and N. J. Halas, *Nano Lett.*, 2013, **13**, 240–247.

217 M. Ahlawat, D. Mittal and V. Govind Rao, *Commun. Mater.*, 2021, **2**, 1–15.

218 C. Ng, J. J. Cadusch, S. Dligatch, A. Roberts, T. J. Davis, P. Mulvaney and D. E. Gómez, *ACS Nano*, 2016, **10**, 4704–4711.

219 K. Wu, J. Chen, J. R. McBride and T. Lian, *Science*, 2015, **349**, 632–635.

220 R. Asapu, N. Claes, R.-G. Ciocarlan, M. Minjauw, C. Detavernier, P. Cool, S. Bals and S. W. Verbruggen, *ACS Appl. Nano Mater.*, 2019, **2**, 4067–4074.

221 Y. Horiguchi, T. Kanda, K. Torigoe, H. Sakai and M. Abe, *Langmuir*, 2014, **30**, 922–928.

222 X. Zhang, S. Yuan, Y. Yuan and X. Li, *Optoelectron. Lett.*, 2015, **11**, 1–4.

223 R. Ninakanti, F. Dingenen, R. Borah, H. Peeters and S. W. Verbruggen, *Top. Curr. Chem.*, 2022, **380**, 40.

224 S. Link, Z. L. Wang and M. A. El-Sayed, *J. Phys. Chem. B*, 1999, **103**, 3529–3533.

225 L. M. Liz-Marzán, *Langmuir*, 2006, **22**, 32–41.

226 S. W. Verbruggen, M. Keulemans, J. A. Martens and S. Lenaerts, *J. Phys. Chem. C*, 2013, **117**, 19142–19145.

227 F. Dingenen, N. Blommaerts, M. Van Hal, R. Borah, D. Arenas-Esteban, S. Lenaerts, S. Bals and S. W. Verbruggen, *Nanomaterials*, 2021, **11**, 2624.

228 N. Zhou, L. Polavarapu, N. Gao, Y. Pan, P. Yuan, Q. Wang and Q.-H. Xu, *Nanoscale*, 2013, **5**, 4236–4241.

229 Y. Zhu, S. Yang, J. Cai, M. Meng and X. Li, *Mater. Lett.*, 2015, **154**, 163–166.

230 D. B. Ingram, P. Christopher, J. L. Bauer and S. Linic, *ACS Catal.*, 2011, **1**, 1441–1447.

231 H. Peeters, M. Keulemans, G. Nuyts, F. Vanmeert, C. Li, M. Minjauw, C. Detavernier, S. Bals, S. Lenaerts and S. W. Verbruggen, *Appl. Catal. B Environ.*, 2020, **267**, 118654.

232 A. Yadav, Y. Li, T.-W. Liao, K.-J. Hu, J. E. Scheerder, O. V. Safonova, T. Höltzl, E. Janssens, D. Grandjean and P. Lievens, *Small*, 2021, **17**, 2004541.

233 T. G. Dietz, M. A. Duncan, D. E. Powers and R. E. Smalley, *J. Chem. Phys.*, 1981, **74**, 6511–6512.

234 W. Bouwen, P. Thoen, F. Vanhoutte, S. Bouckaert, F. Despa, H. Weidele, R. E. Silverans and P. Lievens, *Rev. Sci. Instrum.*, 2000, **71**, 54–58.

235 T.-W. Liao, S. W. Verbruggen, N. Claes, A. Yadav, D. Grandjean, S. Bals and P. Lievens, *Nanomaterials*, 2018, **8**, 30.

236 F. D'Acapito, G. Lepore, A. Puri, A. Laloni, F. Manna, E. Dettona, A. Luisa and A. Martin, *J. Synchrotron Radiat.*, , DOI:10.1107/S160057751801843X.

237 T. Hihara and K. Sumiyama, *J. Vac. Sci. Technol. B Microelectron. Nanometer Struct. Process. Meas. Phenom.*, 1999, **17**, 1923–1929.

238 R. Liu, Q. Li and L. M. Smith, *J. Am. Soc. Mass Spectrom.*, 2014, **25**, 1374–1383.

239 R. Esparza, G. Rosas, E. Valenzuela, Iii, S. A. Gamboa, U. Pal, Iv and R. Perez-Campos, *Matér. Rio Jan.*, 2008, **13**, 579–586.

240 N. van Vegten, P. Haider, M. Maciejewski, F. Krumeich and A. Baiker, *J. Colloid Interface Sci.*, 2009, **339**, 310–316.

241 V. Petkov, Y. Peng, G. Williams, B. Huang, D. Tomalia and Y. Ren, *Phys. Rev. B*, 2005, **72**, 195402.

242 T.-W. Liao, A. Yadav, K.-J. Hu, J. van der Tol, S. Cosentino, F. D'Acapito, R. E. Palmer, C. Lenardi, R. Ferrando, D. Grandjean and P. Lievens, *Nanoscale*, 2018, **10**, 6684–6694.

243 I. J. Godfrey, A. J. Dent, I. P. Parkin, S. Maenosono and G. Sankar, *J. Phys. Chem. C*, 2017, **121**, 1957–1963.

244 R. E. Benfield, *J. Chem. Soc. Faraday Trans.*, 1992, **88**, 1107–1110.

245 D. Briggs, V. J. I. Zichy, D. M. Brewis, J. Comyn, R. H. Dahm, M. A. Green and M. B. Konieczko, *Surf. Interface Anal.*, 1980, **2**, 107–114.

246 A. Alqudami, S. Annapoorni, Govind and S. M. Shivaprasad, *J. Nanoparticle Res.*, 2008, **10**, 1027–1036.

247 P. Sangpour, O. Akhavan, A. Z. Moshfegh and M. Roozbehi, *Appl. Surf. Sci.*, 2007, **254**, 286–290.

248 P. Sangpour, O. Akhavan and A. Z. Moshfegh, *J. Alloys Compd.*, 2009, **486**, 22–28.

249 A. E. Taverner, A. Gulino, R. G. Egdell and T. J. Tate, *Appl. Surf. Sci.*, 1995, **90**, 383–387.

250 X. Yang, Y. Wang, L. Zhang, H. Fu, P. He, D. Han, T. Lawson and X. An, *Catalysts*, 2020, **10**, 139.

251 H. Alloul, in *Introduction to the Physics of Electrons in Solids*, ed. H. Alloul, Springer, Berlin, Heidelberg, 2011, pp. 51–97.

252 S. Nishimura, A. T. N. Dao, D. Mott, K. Ebitani and S. Maenosono, *J. Phys. Chem. C*, 2012, **116**, 4511–4516.

253 A. Bzowski, Y. M. Yiu and T. K. Sham, *Phys. Rev. B*, 1995, **51**, 9515–9520.

254 T. K. Sham, M. L. Perlman and R. E. Watson, *Phys. Rev. B*, 1979, **19**, 539–545.

255 C. C. Tyson, A. Bzowski, P. Kristof, M. Kuhn, R. Sammynaiken and T. K. Sham, *Phys. Rev. B*, 1992, **45**, 8924–8928.

256 B. Hammer and J. K. Norskov, *Nature*, 1995, **376**, 238–240.

257 J. K. Nørskov, F. Abild-Pedersen, F. Studt and T. Bligaard, *Proc. Natl. Acad. Sci. U. S. A.*, 2011, **108**, 937–943.

258 T.-W. Liao, A. Yadav, P. Ferrari, Y. Niu, X.-K. Wei, J. Vernieres, K.-J. Hu, M. Heggen, R. E. Dunin-Borkowski, R. E. Palmer, K. Laasonen, D. Grandjean, E. Janssens and P. Lievens, *Chem. Mater.*, 2019, **31**, 10040–10048.

259 X. Wei, C. Xiao, K. Wang and Y. Tu, *J. Electroanal. Chem.*, 2013, **702**, 37–44.

260 C. M. Aikens, S. Li and G. C. Schatz, *J. Phys. Chem. C*, 2008, **112**, 11272–11279.

261 S. W. Verbruggen, M. Keulemans, M. Filippousi, D. Flahaut, G. Van Tendeloo, S. Lacombe, J. A. Martens and S. Lenaerts, *Appl. Catal. B Environ.*, 2014, **156–157**, 116–121.

262 S. W. Verbruggen, M. Keulemans, B. Goris, N. Blommaerts, S. Bals, J. A. Martens and S. Lenaerts, *Appl. Catal. B Environ.*, 2016, **188**, 147–153.

263 P. Mulvaney, *Langmuir*, 1996, **12**, 788–800.

264 J. Kimling, M. Maier, B. Okenve, V. Kotaidis, H. Ballot and A. Plech, *J. Phys. Chem. B*, 2006, **110**, 15700–15707.

265 W. Haiss, N. T. K. Thanh, J. Aveyard and D. G. Fernig, *Anal. Chem.*, 2007, **79**, 4215–4221.

266 S. Agnihotri, S. Mukherji and S. Mukherji, *RSC Adv.*, 2013, **4**, 3974–3983.

267 U. Aslam, V. G. Rao, S. Chavez and S. Linic, *Nat. Catal.*, 2018, **1**, 656–665.

268 X. Zhang, Y. L. Chen, R.-S. Liu and D. P. Tsai, *Rep. Prog. Phys.*, 2013, **76**, 046401.

269 B. Y. Zheng, H. Zhao, A. Manjavacas, M. McClain, P. Nordlander and N. J. Halas, *Nat. Commun.*, 2015, **6**, 7797.

270 H. Shi, X. Zhu, S. Zhang, G. Wen, M. Zheng and H. Duan, *Nanoscale Adv.*, 2021, **3**, 4349–4369.

271 J. A. Scholl, A. L. Koh and J. A. Dionne, *Nature*, 2012, **483**, 421–427.

272 A. Campos, N. Troc, E. Cottancin, M. Pellarin, H.-C. Weissker, J. Lermé, M. Kociak and M. Hillenkamp, *Nat. Phys.*, 2019, **15**, 275–280.

273 G. L. Nealon, B. Donnio, R. Greget, J.-P. Kappler, E. Terazzi and J.-L. Gallani, *Nanoscale*, 2012, **4**, 5244–5258.

274 R. Borah and S. W. Verbruggen, *J. Phys. Chem. C*, 2020, **124**, 12081–12094.

275 A. Marzo, P. Ferrada, F. Beiza, P. Besson, J. Alonso-Montesinos, J. Ballestrín, R. Román, C. Portillo, R. Escobar and E. Fuentealba, *Renew. Energy*, 2018, **127**, 871–882.

276 M. Valenti, A. Venugopal, D. Tordera, M. P. Jonsson, G. Biskos, A. Schmidt-Ott and W. A. Smith, *ACS Photonics*, 2017, **4**, 1146–1152.

277 N. Alissawi, V. Zaporojtchenko, T. Strunskus, I. Kocabas, V. S. K. Chakravadhanula, L. Kienle, D. Garbe-Schönberg and F. Faupel, *Gold Bull.*, 2013, **46**, 3–11.

278 N. R. Kim, K. Shin, I. Jung, M. Shim and H. M. Lee, *J. Phys. Chem. C*, 2014, **118**, 26324–26331.

279 S. Raza, W. Yan, N. Stenger, M. Wubs and N. A. Mortensen, *Opt. Express*, 2013, **21**, 27344–27355.

280 R. Watanabe-Tamaki, A. Ishikawa and T. Tanaka, *Appl. Phys. Lett.*, 2013, **102**, 043110.

281 X. Fan, W. Zheng and D. J. Singh, *Light Sci. Appl.*, 2014, **3**, e179–e179.

282 N. Blommaerts, R. Asapu, N. Claes, S. Bals, S. Lenaerts and S. W. Verbruggen, *Chem. Eng. J.*, 2017, **316**, 850–856.

283 R. Asapu, R.-G. Ciocarlan, N. Claes, N. Blommaerts, M. Minjauw, T. Ahmad, J. Dendooven, P. Cool, S. Bals, S. Denys, C. Detavernier, S. Lenaerts and S. W. Verbruggen, *ACS Appl. Mater. Interfaces*, 2017, **9**, 41577–41585.

284 A. Mills, N. Elliott, G. Hill, D. Fallis, J. R. Durrant and R. L. Willis, *Photochem. Photobiol. Sci.*, 2003, **2**, 591–596.

285 A. Mills, G. Hill, S. Bhopal, I. P. Parkin and S. A. O'Neill, *J. Photochem. Photobiol. Chem.*, 2003, **160**, 185–194.

286 A. Mills, S.-K. Lee, A. Lepre, I. P. Parkin and S. A. O'Neill, *Photochem. Photobiol. Sci.*, 2002, **1**, 865–868.

287 G. Kenanakis, Z. Giannakoudakis, D. Vernardou, C. Savvakis and N. Katsarakis, *Catal. Today*, 2010, **151**, 34–38.

288 R. Quesada-Cabrera, C. Sotelo-Vazquez, J. A. Darr and I. P. Parkin, *Appl. Catal. B Environ.*, 2014, **160–161**, 582–588.

289 H. Keskinen, J. M. Mäkelä, M. Aromaa, J. Keskinen, S. Areva, C. V. Teixeira, J. B. Rosenholm, V. Pore, M. Ritala, M. Leskelä, M. Raulio, M. S. Salkinoja-Salonen, E. Levänen and T. Mäntylä, *Catal. Lett.*, 2006, **111**, 127–132.

290 A. Sandoval, L. Delannoy, C. Méthivier, C. Louis and R. Zanella, *Appl. Catal. Gen.*, 2015, **504**, 287–294.

291 A.-Q. Wang, C.-M. Chang and C.-Y. Mou, *J. Phys. Chem. B*, 2005, **109**, 18860–18867.

292 Y. Yang, T. Zhang, L. Le, X. Ruan, P. Fang, C. Pan, R. Xiong, J. Shi and J. Wei, *Sci. Rep.*, 2014, **4**, 7045.

293 F. J. Knorr, D. Zhang and J. L. McHale, *Langmuir*, 2007, **23**, 8686–8690.

294 K. Ueda, Y. Nakato, N. Suzuki and H. Tsubomura, *J. Electrochem. Soc.*, 1989, **136**, 2280.

295 H. Kobayashi, F. Mizuno, Y. Nakato and H. Tsubomura, *J. Phys. Chem.*, 1991, **95**, 819–824.

296 R. K. Keswani, H. Ghodke, D. Sarkar, K. C. Khilar and R. S. Srinivasa, *Colloids Surf. Physicochem. Eng. Asp.*, 2010, **369**, 75–81.

297 B. Liu, D. Deng, J. Y. Lee and E. S. Aydil, *J. Mater. Res.*, 2010, **25**, 1588–1594.

298 Z. Zander, R. Yagloski, J. DeCoste, D. Zhang and B. G. DeLacy, *Mater. Lett.*, 2016, **163**, 39–42.

299 J. M. Macak, H. Hildebrand, U. Marten-Jahns and P. Schmuki, *J. Electroanal. Chem.*, 2008, **621**, 254–266.

300 G. D. Sulka, J. Kapusta-Kołodziej, A. Brzózka and M. Jaskuła, *Electrochimica Acta*, 2010, **55**, 4359–4367.

301 J. M. Macak, H. Tsuchiya, A. Ghicov, K. Yasuda, R. Hahn, S. Bauer and P. Schmuki, *Curr. Opin. Solid State Mater. Sci.*, 2007, **11**, 3–18.

302 G. D. Sulka, J. Kapusta-Kołodziej, A. Brzózka and M. Jaskuła, *Electrochimica Acta*, 2013, **104**, 526–535.

303 J. M. Macak and P. Schmuki, *Electrochimica Acta*, 2006, **52**, 1258.

304 S. Bauer, S. Kleber and P. Schmuki, *Electrochem. Commun.*, 2006, **8**, 1321–1325.

305 V. Zwilling, M. Aucouturier and E. Darque-Ceretti, *Electrochimica Acta*, 1999, **45**, 921–929.

306 D. Gong, C. A. Grimes, O. K. Varghese, W. Hu, R. S. Singh, Z. Chen and E. C. Dickey, *J. Mater. Res.*, 2001, **16**, 3331–3334.

307 S. Rani, S. C. Roy, M. Paulose, O. K. Varghese, G. K. Mor, S. Kim, S. Yoriya, T. J. LaTempa and C. A. Grimes, *Phys. Chem. Chem. Phys.*, 2010, **12**, 2780–2800.

308 H. Brahmi, G. Katwal, M. Khodadadi, S. Chen, M. Paulose, O. K. Varghese and A. Mavrokefalos, *Nanoscale*, 2015, **7**, 19004–19011.

309 X. Nie, S. Yin, W. Duan, Z. Zhao, L. Li and Z. Zhang, *Nano*, 2021, **16**, 2130002.

310 S. Kment, F. Riboni, S. Pausova, L. Wang, L. Wang, H. Han, Z. Hubicka, J. Krysa, P. Schmuki and R. Zboril, *Chem. Soc. Rev.*, 2017, **46**, 3716–3769.

311 M. Ge, Q. Li, C. Cao, J. Huang, S. Li, S. Zhang, Z. Chen, K. Zhang, S. S. Al-Deyab and Y. Lai, *Adv. Sci.*, , DOI:10.1002/advs.201770005.

312 J. F. De Brito, F. Tavella, C. Genovese, C. Ampelli, M. V. B. Zanoni, G. Centi and S. Perathoner, *Appl. Catal. B Environ.*, 2018, **224**, 136–145.

313 M. Paulose, K. Shankar, S. Yoriya, H. E. Prakasam, O. K. Varghese, G. K. Mor, T. J. LaTempa, A. Fitzgerald and C. A. Grimes, *J. Phys. Chem. B*, 2006, **110**, 16179–16184.

314 J. M. Macak, M. Zlamal, J. Krysa and P. Schmuki, *Small Weinh. Bergstr. Ger.*, 2007, **3**, 300–304.

315 Y. Jiang, B. Zheng, J. Du, G. Liu, Y. Guo and D. Xiao, *Talanta*, 2013, **112**, 129–135.

316 L. Martínez, L. Soler, I. Angurell and J. Llorca, *Appl. Catal. B Environ.*, 2019, **248**, 504–514.

317 K. Shankar, J. I. Basham, N. K. Allam, O. K. Varghese, G. K. Mor, X. Feng, M. Paulose, J. A. Seabold, K.-S. Choi and C. A. Grimes, *J. Phys. Chem. C*, 2009, **113**, 6327–6359.

318 P. Szymanski and M. A. El-Sayed, *Theor. Chem. Acc.*, 2012, **131**, 1202.

319 A. Fujishima and K. Honda, *Nature*, 1972, **238**, 37–38.

320 M. Grätzel, *Nature*, 2001, **414**, 338–344.

321 S. U. M. Khan, M. Al-Shahry and W. B. Ingler, *Science*, 2002, **297**, 2243–2245.

322 Q. Peng, B. Kalanyan, P. G. Hoertz, A. Miller, D. H. Kim, K. Hanson, L. Alibabaei, J. Liu, T. J. Meyer, G. N. Parsons and J. T. Glass, *Nano Lett.*, 2013, **13**, 1481–1488.

323 M. R. Khan, T. W. Chuan, A. Yousuf, M. N. K. Chowdhury and C. K. Cheng, *Catal. Sci. Technol.*, 2015, **5**, 2522–2531.

324 E. Grabowska, A. Zaleska, S. Sorgues, M. Kunst, A. Etcheberry, C. Colbeau-Justin and H. Remita, *J. Phys. Chem. C*, 2013, **117**, 1955–1962.

325 M. G. Méndez-Medrano, E. Kowalska, A. Lehoux, A. Herissan, B. Ohtani, D. Bahena, V. Briois, C. Colbeau-Justin, J. L. Rodríguez-López and H. Remita, *J. Phys. Chem. C*, 2016, **120**, 5143–5154.

326 L. Sun, J. Li, C. Wang, S. Li, Y. Lai, H. Chen and C. Lin, *J. Hazard. Mater.*, 2009, **171**, 1045–1050.

327 P. A. Gross, S. N. Pronkin, T. Cottineau, N. Keller, V. Keller and E. R. Savinova, *Catal. Today*, 2012, **189**, 93–100.

328 J. Ma, M. Yang, Y. Sun, C. Li, Q. Li, F. Gao, F. Yu and J. Chen, *Phys. E Low-Dimens. Syst. Nanostructures*, 2014, **58**, 24–29.

329 I. Paramasivam, J. M. Macak and P. Schmuki, *Electrochem. Commun.*, 2008, **10**, 71–75.

330 S. Zhang, F. Peng, H. Wang, H. Yu, S. Zhang, J. Yang and H. Zhao, *Catal. Commun.*, 2011, **12**, 689–693.

331 K. Xie, L. Sun, C. Wang, Y. Lai, M. Wang, H. Chen and C. Lin, *Electrochimica Acta*, 2010, **55**, 7211–7218.

332 Y. Wang, Z. Li, Y. Tian, W. Zhao, X. Liu and J. Yang, *Mater. Lett.*, 2014, **122**, 248–251.

333 K. Syrek, J. Grudzień, A. Sennik-Kubiec, A. Brudzisz and G. D. Sulka, *J. Nanomater.*, 2019, **2019**, e9208734.

334 R. Ferrando, J. Jellinek and R. L. Johnston, *Chem. Rev.*, 2008, **108**, 845–910.

335 B. Zhu, L.-Y. Zhang, J.-L. Liu, X.-M. Zhang, X.-S. Li and A.-M. Zhu, *J. Hazard. Mater.*, 2021, **402**, 123508.

336 Ş. Neaţu, J. A. Maciá-Agulló, P. Concepción and H. Garcia, *J. Am. Chem. Soc.*, 2014, **136**, 15969–15976.

337 T. H. Tan, J. A. Scott, Y. H. Ng, R. A. Taylor, K.-F. Aguey-Zinsou and R. Amal, *J. Catal.*, 2017, **352**, 638–648.

338 Y. Sugano, Y. Shiraishi, D. Tsukamoto, S. Ichikawa, S. Tanaka and T. Hirai, *Angew. Chem.*, 2013, **125**, 5403–5407.

339 Z.-Y. Li, Y.-H. Chen, J.-R. Zhu, Q. Chen, S.-J. Lu and F.-X. Xiao, *Inorg. Chem.*, 2023, **62**, 16965–16973.

340 W. Lipińska, K. Grochowska, J. Ryl, J. Karczewski and K. Siuzdak, *ACS Appl. Mater. Interfaces*, 2021, **13**, 52967–52977.

341 D. Gong, C. A. Grimes, O. K. Varghese, W. Hu, R. S. Singh, Z. Chen and E. C. Dickey, *J. Mater. Res.*, 2001, **16**, 3331–3334.

342 Z. Hua, Z. Dai, X. Bai, Z. Ye, P. Wang, H. Gu and X. Huang, *Chem. Eng. J.*, 2016, **283**, 514–523.

343 K. Grochowska, N. Nedyalkov, J. Karczewski, Ł. Haryński, G. Śliwiński and K. Siuzdak, *Sci. Rep.*, 2020, **10**, 20506.

344 Agagcl Reference Electrode Working Principle And Applications, https://kindle-tech.com/articles/agagcl-reference-electrode-working-principle-and-applications, (accessed June 14, 2024).

345 Electrochemcal Impedance Spectroscopy (EIS) Basics, https://pineresearch.com/shop/kb/theory/eis-theory/eis-basics/, (accessed June 13, 2024).

346 G. Xing, N. Mathews, S. Sun, S. S. Lim, Y. M. Lam, M. Grätzel, S. Mhaisalkar and T. C. Sum, *Science*, 2013, **342**, 344–347.

347 S. D. Stranks, G. E. Eperon, G. Grancini, C. Menelaou, M. J. P. Alcocer, T. Leijtens, L. M. Herz, A. Petrozza and H. J. Snaith, *Science*, 2013, **342**, 341–344.

348 M. Nischk, P. Mazierski, Z. Wei, K. Siuzdak, N. A. Kouame, E. Kowalska, H. Remita and A. Zaleska-Medynska, *Appl. Surf. Sci.*, 2016, **387**, 89–102.

349 Y. Pang, G. Xu, Q. Feng, J. Lv, Y. Qin, Y. Zhang, Z. Zheng and Y. Wu, *Phys. Lett. A*, 2018, **382**, 2759–2762.

350 R. Liu, Q. Li and L. M. Smith, *J. Am. Soc. Mass Spectrom.*, 2014, **25**, 1374–1383.

351 D. Hong, A. Sharma, D. Jiang, E. Stellino, T. Ishiyama, P. Postorino, E. Placidi, Y. Kon and K. Koga, *ACS Omega*, 2022, **7**, 31260–31270.

352 T. K. Sham, Y. M. Yiu, M. Kuhn and K. H. Tan, *Phys. Rev. B*, 1990, **41**, 11881–11886.

353 R. E. Watson, J. Hudis and M. L. Perlman, *Phys. Rev. B*, 1971, **4**, 4139–4144.

354 W. Eberhardt, S. C. Wu, R. Garrett, D. Sondericker and F. Jona, *Phys. Rev. B*, 1985, **31**, 8285–8287.

355 M. Kuhn and T. K. Sham, *Phys. Rev. B*, 1994, **49**, 1647–1661.

356 P. Weinberger, A. M. Boring, R. C. Albers and W. M. Temmerman, *Phys. Rev. B*, 1988, **38**, 5357–5362.

357 I. A. Abrikosov, Yu. H. Vekilov and A. V. Ruban, *Phys. Lett. A*, 1991, **154**, 407–412.

358 M. Brown, R. E. Peierls and E. A. Stern, *Phys. Rev. B*, 1977, **15**, 738–744.

359 J. E. Müller, O. Jepsen and J. W. Wilkins, *Solid State Commun.*, 1982, **42**, 365–368.

360 G. D. M. R. Dabera, M. Walker, A. M. Sanchez, H. J. Pereira, R. Beanland and R. A. Hatton, *Nat. Commun.*, 2017, **8**, 1894.

361 K. S. Tan and K. Y. Cheong, *J. Nanoparticle Res.*, 2013, **15**, 1537.

362 S. Zhao, Z. Cheng, S. Wang, H. Hao and Y. Fang, *Appl. Phys. A*, 2021, **127**, 930.

363 D. Albinsson, S. Nilsson, T. J. Antosiewicz, V. P. Zhdanov and C. Langhammer, *J. Phys. Chem. C*, 2019, **123**, 6284–6293.

364 Z. Guo, O. V. Prezhdo, T. Hou, X. Chen, S.-T. Lee and Y. Li, *J. Phys. Chem. Lett.*, 2014, **5**, 1642–1647.

365 S. Kurian, H. Seo and H. Jeon, *J. Phys. Chem. C*, 2013, **117**, 16811–16819.

366 Z. Zhang and P. Wang, *Energy Environ. Sci.*, 2012, **5**, 6506–6512.

367 Z. Zhang, L. Zhang, M. N. Hedhili, H. Zhang and P. Wang, *Nano Lett.*, 2013, **13**, 14–20.

368 M. Szkoda, K. Siuzdak, A. Lisowska-Oleksiak, J. Karczewski and J. Ryl, *Electrochem. Commun.*, 2015, **60**, 212–215.

369 Photoluminescence Spectroscopy, https://www.ossila.com/pages/photoluminescence, (accessed June 11, 2024).

370 Jablonski diagram, https://chem.libretexts.org/Bookshelves/Physical_and_Theoretical_Chemistry_Textbook_Maps/Supplemental_Modules_(Physical_and_Theoretical_Chemistry)/Spectroscopy/Electronic_Spectroscopy/Jablonski_diagram, (accessed June 11, 2024).

371 T. H. Gfroerer, in *Encyclopedia of Analytical Chemistry*, John Wiley & Sons, Ltd, 2006.

372 B.-H. Lee, S. Park, M. Kim, A. K. Sinha, S. C. Lee, E. Jung, W. J. Chang, K.-S. Lee, J. H. Kim, S.-P. Cho, H. Kim, K. T. Nam and T. Hyeon, *Nat. Mater.*, 2019, **18**, 620–626.

373 T. Kiyonaga, M. Fujii, T. Akita, H. Kobayashi and H. Tada, *Phys. Chem. Chem. Phys.*, 2008, **10**, 6553–6561.

374 X. Liu, S. Cui, Z. Sun, Y. Ren, X. Zhang and P. Du, *J. Phys. Chem. C*, 2016, **120**, 831–840.

375 S. M. Pawar, B. S. Pawar, B. Hou, J. Kim, A. T. A. Ahmed, H. S. Chavan, Y. Jo, S. Cho, A. I. Inamdar, J. L. Gunjakar, H. Kim, S. Cha and H. Im, *J. Mater. Chem. A*, 2017, **5**, 12747–12751.

376 K. Kannimuthu, K. Sangeetha, S. S. Sankar, A. Karmakar, R. Madhu and S. Kundu, *Inorg. Chem. Front.*, 2021, **8**, 234–272.

377 D. Kim, J. Resasco, Y. Yu, A. M. Asiri and P. Yang, *Nat. Commun.*, 2014, **5**, 4948.

378 A. Shah, M. Akhtar, S. Aftab, A. H. Shah and H.-B. Kraatz, *Electrochimica Acta*, 2017, **241**, 281–290.

379 U. Latif-ur-Rahman, A. Shah, R. Qureshi, S. B. Khan, A. M. Asiri, A.-H. A. Shah, M. Ishaq, M. S. Khan, S. K. Lunsford and M. A. Zia, *Adv. Mater. Sci. Eng.*, 2015, **2015**, e638629.

380 F. S. Lim, S. T. Tan, Y. Zhu, J.-W. Chen, B. Wu, H. Yu, J.-M. Kim, R. T. Ginting, K. S. Lau, C. H. Chia, H. Wu, M. Gu and W. S. Chang, *J. Phys. Chem. C*, 2020, **124**, 14105–14117.

381 R. Siavash Moakhar, M. Jalali, A. Kushwaha, G. Kia Liang Goh, N. Riahi-Noori, A. Dolati and M. Ghorbani, *J. Appl. Electrochem.*, 2018, **48**, 995–1007.

382 C. Jian, J. Zhang, W. He and X. Ma, *Nano Energy*, 2021, **82**, 105763.

383 C. Jian, J. Zhang and X. Ma, *RSC Adv.*, 2020, **10**, 13277–13285.

384 Y.-H. Su and W.-L. Wang, *Nanoscale Res. Lett.*, 2013, **8**, 408.

385 T.-S. Kim, H. Choi, D. Kim, H. C. Song, Y. Oh, B. Jeong, J. Lee, K.-J. Kim, J. W. Shin, H. R. Byon, R. Ryoo, H. Y. Kim and J. Y. Park, *Appl. Catal. B Environ.*, 2023, **331**, 122704.

386 Y. Li, W.-N. Wang, Z. Zhan, M.-H. Woo, C.-Y. Wu and P. Biswas, *Appl. Catal. B-Environ. - APPL CATAL B-Env.*, 2010, **100**, 386–392.

387 Y. Hori, K. Kikuchi and S. Suzuki, *Chem. Lett.*, 1985, **14**, 1695–1698.

388 J. Albero, Y. Peng and H. García, *ACS Catal.*, 2020, **10**, 5734–5749.

389 D. Yang, Q. Zhu, C. Chen, H. Liu, Z. Liu, Z. Zhao, X. Zhang, S. Liu and B. Han, *Nat. Commun.*, 2019, **10**, 677.

390 Y. Hori, K. Kikuchi, A. Murata and S. Suzuki, *Chem. Lett.*, 1986, **15**, 897–898.

391 R. B. Jackson, C. L. Quéré, R. M. Andrew, J. G. Canadell, J. I. Korsbakken, Z. Liu, G. P. Peters and B. Zheng, *Environ. Res. Lett.*, 2018, **13**, 120401.

392 J. Jiao, Y. Wei, Y. Zhao, Z. Zhao, A. Duan, J. Liu, Y. Pang, J. Li, G. Jiang and Y. Wang, *Appl. Catal. B Environ.*, 2017, **209**, 228–239.

393 M. Tahir, B. Tahir and N. A. S. Amin, *Appl. Catal. B Environ.*, 2017, **204**, 548–560.

394 B. D. Mankidy, B. Joseph and V. K. Gupta, *Nanotechnology*, 2013, **24**, 405402.

395 J.-H. Lee, M.-H. You, G.-H. Kim and J.-M. Nam, *Nano Lett.*, 2014, **14**, 6217–6225.

396 L. Liu, T. D. Dao, R. Kodiyath, Q. Kang, H. Abe, T. Nagao and J. Ye, *Adv. Funct. Mater.*, 2014, **24**, 7754–7762.

397 J. N. G. Stanley, I. García-García, T. Perfrement, E. C. Lovell, T. W. Schmidt, J. Scott and R. Amal, *Chem. Eng. Sci.*, 2019, **194**, 94–104.

398 O. A. Yeshchenko, I. M. Dmitruk, A. A. Alexeenko, A. V. Kotko, J. Verdal and A. O. Pinchuk, *Plasmonics*, 2012, **7**, 685–694.

399 K. Qian, B. C. Sweeny, A. C. Johnston-Peck, W. Niu, J. O. Graham, J. S. DuChene, J. Qiu, Y.-C. Wang, M. H. Engelhard, D. Su, E. A. Stach and W. D. Wei, *J. Am. Chem. Soc.*, 2014, **136**, 9842–9845.

400 S. Linic, P. Christopher, H. Xin and A. Marimuthu, *Acc. Chem. Res.*, 2013, **46**, 1890–1899.

401 R. J. Chimentão, I. Kirm, F. Medina, X. Rodríguez, Y. Cesteros, P. Salagre and J. E. Sueiras, *Chem. Commun.*, 2004, 846–847.

402 S. Zhu and D. Wang, *Adv. Energy Mater.*, 2017, **7**, 1700841.

403 P. Dias and A. Mendes, in *Encyclopedia of Sustainability Science and Technology*, ed. R. A. Meyers, Springer, New York, NY, 2017, pp. 1–52.

404 Z. Zhu, F. Chen, N. Tian, Y. Zhang and H. Huang, *Curr. Opin. Green Sustain. Chem.*, 2022, **37**, 100669.

405 Y. Li, Q. Wang, X. Hu, Y. Meng, H. She, L. Wang, J. Huang and G. Zhu, *Chem. Eng. J.*, 2022, **433**, 133592.

406 D. Lee, W. Wang, C. Zhou, X. Tong, M. Liu, G. Galli and K.-S. Choi, *Nat. Energy*, 2021, **6**, 287–294.

Curriculum Vitae

PERSONAL INFORMATION

Name:	Chinnabathini **Vana** Chinnappa
Date of birth:	February 27th, 1980
Place of birth:	Govindapuram, Telangana, India
Address:	Jesuit residence, 54-16-14/5, Andhra Loyola college, Vijayawada-520008, AP, India
Nationality:	Indian
e-mail (private):	cvchinnasj@gmail.com
Mobile number:	+32 493253341, +917893635863

EDUCATION

2001-2004	Bachelor in Physics (ALC, Vijayawada, AP, India)
2004-2006	Diploma in Philosophy (Jnana Deepa Vidyapeeth, India)
2007-2009	Master in Physics (Loyola college, Chennai, India)
2010-2014	Bachelor in Theology (Vidya Jyoti school of theology, Delhi, India)
2019-2020	Predoctoral studies in Science (KU Leuven)
2020-2024	PhD in Science: Physics (joint degree of KU Leuven and University of Antwerp)

Publications

- **<u>Chinnabathini, V.C</u>**., Dingenen, F., Borah, R., Abbas, I., van der Tol, J., Zarkua, Z., D'Acapito, F., Nguyen, T.H T., Lievens, P., Grandjean, D., Verbruggen, S.W., Janssens, E. (2023). *Gas phase deposition of well-defined bimetallic gold-silver clusters for photocatalytic applications.* **NANOSCALE, 15(14), 6696-6708. doi: <u>10.1039/d2nr07287d</u>.**

- Nguyen, T.H. T., Zarkua, Z., **<u>Chinnabathini, V.C</u>**., Hu, W., Sree, S.P., Grandjean, D., Pant, D., Janssens, E. (2023). *$Co_{3-x}Fe_xO_4$ inverse opals with tunable catalytic activity for high-performance overall water splitting*. **NANOSCALE, 15, 10306-10318. doi: <u>10.1039/d2nr07300e</u>.**

   IN PREPARATION:

- **<u>Chinnabathini, V.C.,</u>** Karthick, R.A., Abbas, I., Nguyen, T.H. T., Zarkua, Z., Hoang, T.H., Grandjean, D., Verbruggen, S.W., and Janssens, E. *Composition-dependent and oxygen-induced atomically restructured well-defined gas phase AuCu clusters on titania nanotubes for photoelectrochemical applications.*

- Nguyen, T.H. T., Singh, Chandani., Shen, Jing., **<u>Chinnabathini, V.C.,</u>** Papamichail, D., Sanchez, O.G., Hu, W., Grandjean, D., Pant, D., and Janssens, E. *Pd nanocluster-modified Mesoporous Copper Oxide Inverse Opals as Electrocatalysts for CO_2 Reduction to C_2 Products.*

- Nguyen, T.H. T., **<u>Chinnabathini, V.C</u>**., Grandjean, D., and Janssens, E. *Gas Phase-Gold Nanoparticles modified Cobalt Iron Oxide Hollow Spheres as High-Performance Oxygen Reduction Electrocatalyst.*